Thesis for the Degree of Doctor of Philosophy

Cellulose Nanofiber Matrix−Assisted 3D Printing

셀룰로오스 나노섬유 매트릭스 지지
3차원 프린팅

February 2020

Seoul National University
Department of Biosystems & Biomaterials
Science and Engineering

Shin, Sungchul

Abstract

Cellulose nanofibers (CNFs) are attracting material for a three-dimensional (3D) printing matrix due to excellent rheological characteristics. In 3D printing with CNFs, a nozzle moves through the viscoelastic CNF matrix and makes patterns with ink materials. Rheological properties of CNFs are related to various factors including fiber dimension and concentration of CNFs in the aqueous dispersion, and influence on the printing fidelity. The different morphology of CNFs was prepared by varying the degree of carboxymethylation with CNFs. The printing fidelity was evaluated by observing the shape of ink features that were printed directly inside the CNF matrix. The relationship between the rheological properties of the CNF matrix and the printing fidelity was investigated on the printing speed, strain fields, and yielded regions. The cell-containing bio-ink and hydrophobic silicon-based inks were printed in the CNF matrix in a complex structure with high printing fidelity. Amazingly, the structure printed freely in the CNF hydrogels was able to retain its highly resolved 3D features in an ultrathin two-dimensional (2D) paper using a simple drying process. The dimensional change in the CNF hydrogels from 3D to 2D resulted from simple dehydration of the CNFs and provided transparent, stackable paper-based 3D channel devices. The CNF devices exhibited selective diffusion of molecules from the channel wall, indicating the applicability for the sensor and the cell culture platforms.

Table of Contents

List of Figures

vii

I. Introduction

The current major problems in 3D printing are focused on inks and printing systems. However, in addition to ink, the matrix is one of the most critical components in 3D printing of soft matter. Nevertheless, matrix research is rarely reported due to the lack of selectable materials. The matrix plays an important role in maintaining printed structures in a free-standing form in the bulk space [1, 2]. To this end, the simple removal of ink from the matrix enabled the construction of microchannels to become the starting point of the research on matrix-assisted 3D printing of microfluidic devices. In addition, the deformation of a bulky matrix into a film enforced the vertical integration of 3D structures by natural dehydration and it made the research more challenging.

Matrix-assisted 3D printing (MAP) using a matrix and ink was most effective for printing free-standing structures and a smart choice for the rapid prototyping of microfluidic systems due to the ease of processing and freedom of design. The free-standing 3D structures could be fabricated by extruding inks in the liquid matrix including PDMS prepolymers [3, 4], self-healing hydrogels [5] and granular gel media [6]. A green material, cellulose nanofiber (CNF) hydrogel, was adopted as a potential novel matrix in the research, and the critical factors were investigated for the 3D printing of free-standing structures using this material.

Cellulose is a limitless resource on earth, and CNF has been widely researched from a new angle in recent decades. Due to a high water content of 98% and superior mechanical properties [7, 8], CNFs have been applied as substrates of transparent films [9-12], porous packaging [13], tissue engineering scaffolds [14-16], hydrogels and aerogels [17-19], and battery electrodes [20-22]. In recent years, CNFs has been used as an additive to ink for the enhancement of low viscosity in the ink and the directional

deformation of structures, and as an embedding material for direct 3D printing [23-26]. However, no research has been reported on the use of CNFs as a matrix in 3D printing or a platform for microfluidic devices. Therefore, the quantitative criteria needed to be suggested for excellent printing fidelity.

Here, the rheological properties of the CNF matrix were adjusted by controlling the carboxylic content and concentration. The carboxylic content was changed to control the fiber dimension during the nanofibrilation process. The rheological properties of CNF were varied with the concentration of CNF between 0.25 and 1.5%. The printing fidelity was evaluated by observing the features of printed inks inside the CNF matrix at the controlled conditions. The controlled rheological parameter was strongly related to the accurate printing of 3D structures. It was possible to print microfluidic channels using a CNF hydrogel matrix in a simple and rapid process. The vertical integration of the microchannels printed in 3D was achieved through simple drying. This is a unique new concept in the fabrication of microfluidic systems that have not yet been reported. The bulky CNF hydrogel matrix deformed into a thin film during drying. Since a thin and dense barrier of CNF was formed between the printed features, the resolved integration of microchannels was naturally achieved.

CNF hydrogels are composed of high aspect-ratio natural nanofibers; CNF films with microchannels are flexible and even foldable after dehydration, and additional selective finishing processes were available. In addition, it was possible to monitor the chemical reactions in the microchannels due to the high transparency of CNF-based devices fabricated by matrix-assisted 3D printing. Another unique feature of our microfluidic devices is that they are distinct from paper wicking sensing platforms, which suffer from undesirable retention, high adsorption of analytes to the bulk and the opacity of paper [27-30].

This is the first report to fabricate microfluidic channels in the CNF matrix using 3D printing and to integrate the 3D structures by deforming the matrix to 2D. It will be applicable to the compact design of microfluidic devices and the effective stacking of multitasking devices by simply connecting the layers. With a simple process and easy control of composition, CNF hydrogel could be used as a generic matrix for 3D printing with a combination of a variety of ink materials in the future.

II. Literature survey

2.1. Various 3D printing technologies.

Charles W. Hull first conceived the earliest 3D printing technology in 1986 under the name of "stereolithography" [31]. Stereolithography is a method in which thin layers are sequentially printed by applying ultraviolet rays to a resin that can be cured to produce a three-dimensional structure [32-34]. This advancement in three-dimensional printing has enabled a new dimension of printing over the last few decades. The production of 3D structures enabled us to fabricate prototypes, especially in the industry, and specialized in the production of personalized and customized products [34-36]. In addition to manufacturing these products, 3D printing has been used in a variety of fields such as medicine, science, and education. By using 3D printing, doctors can create patient-customized organ structures, and labs use them to create customized scientific tools.

3D printing technology has evolved in many different ways, but they share the same principles. It is to make three-dimensional structures from one-dimensional lines and two-dimensional faces by stacking them. Those multiple steps make 3D printing slower to fabricate 3D structures compared to a conventional molding method. However, 3D printing has strength in manufacturing various topologies that are limited using a mold. To get a final product with a 3D printer, several steps have to be passed. First of all, a structure should be designed with a computer and then it should be sent to a slicer that breaks it up into one or two-dimensional structures depending on the 3D printing technology. The disassembled structures are input to the 3D printer, and printing will start. Various three-dimensional structures can be produced directly from various materials with 3D printing technology. Common light- and ink-based 3D printing methods are described in Figure 1.

Stereolithography, abbreviated as SLA, was the first 3D printing technique. SLA is a laser-based printing technology. In SLA, the liquid resin is selectively photopolymerized by a rastering laser. When one layer is printed, a new layer of liquid resin is introduced, and the laser is continuously imaged and cross-linked. This process is repeated until the desired 3D structure is completed. State-of-the-art methods, including Digital Projection Lithography (DLP) [37-40], Continuous Liquid Interface Production (CLIP) [41, 42], and Two-Photon Polymerization (2PP) [43-45], are all based on these basic concepts. DLP and CLIP technology, however, differ from conventional SLA technology in that they do not start in one-dimensional lines but in two-dimensional faces using micromirror array device.

In Selective Laser Sintering (SLS), the polymer particles in the powder bed are locally heated and fused by a rastering laser [46-49]. The layer is printed, and fresh powder spreads over the printed layer and locally sintered. Spherical powders with a diameter of 10 μm to 100 μm are generally used for uniform dispersion of the powder. Unsintered particles in the powder bed support the structure during the manufacturing of the three-dimensional structure [50]. Besides, the unsintered powder is recycled after the 3D printing is completed and removed from the powder bed.

Fused Deposition Modeling (FDM), the most commonly used method, is a cost-effective and straightforward approach that utilizes the melting and solidification of materials [51-54]. The polymer is melted and laminated by the heat applied at the nozzle end. The basis of FDM technology is the manufacture of filaments by extrusion process. In general, thermoplastic polymers are widely used, such as polylactic acid (PLA) [55-57], polycaprolactone (PCL) [58, 59], ethylene-vinyl acetate (EVA) [60, 61], and acrylonitrile butadiene styrene (ABS) [52, 62, 63]. To 3D print a stable three-dimensional structure with high resolution, it is necessary to understand the properties of the material thoroughly.

The Direct Ink Writing (DIW) method, designed to print soft materials such as hydrogels and silicones, is very similar to FDM, which produces 3D structures by ejecting ink from nozzles [64-69]. However, DIW deals with soft materials without using thermoplastic polymers. Therefore, the characteristics of the materials are different from those of the FDM method. Appropriate rheological and shear thinning properties are required to eject and stack ink [70-74]. In most cases, the hydrogel is loaded into the syringe and discharged from the nozzle by hydraulic, pneumatic, or screw pressure applied to the syringe. As the shear stress applied at the nozzle, the inks exhibiting shear thinning characteristics will flow well due to their low viscosity at a high shear rate. When the shear stress disappears as ink is ejected, the viscosity will increase to maintain its shape. Therefore, the rheological properties of ink materials are critical for excellent printability [75]. Many researchers have focused on controlling the rheological properties and have outlined the critical elements for stable printing. To be applied to DIW, the ink must be gelled quickly and easily, and it must be well fluidized at the nozzle and ejected with a small resistance. After dispensing, the ink must have a high zero shear viscosity to have sufficient strength to maintain the printed structure. Besides, the structure must be easily cured by ions, heat, or ultraviolet light.

Hydrogel is a material that traps a large amount of water, so it shows very similar physical properties to human organs [76-79]. Many researchers have been working on the use of hydrogels in the biomedical field, which further expands the utility of DIW. 3D bio-printing is a technique for producing three-dimensional structures by mixing living cells with a hydrogel ink to produce living structures having biological and mechanical properties suitable for clinical restoration of tissue and organ functions [80-82].
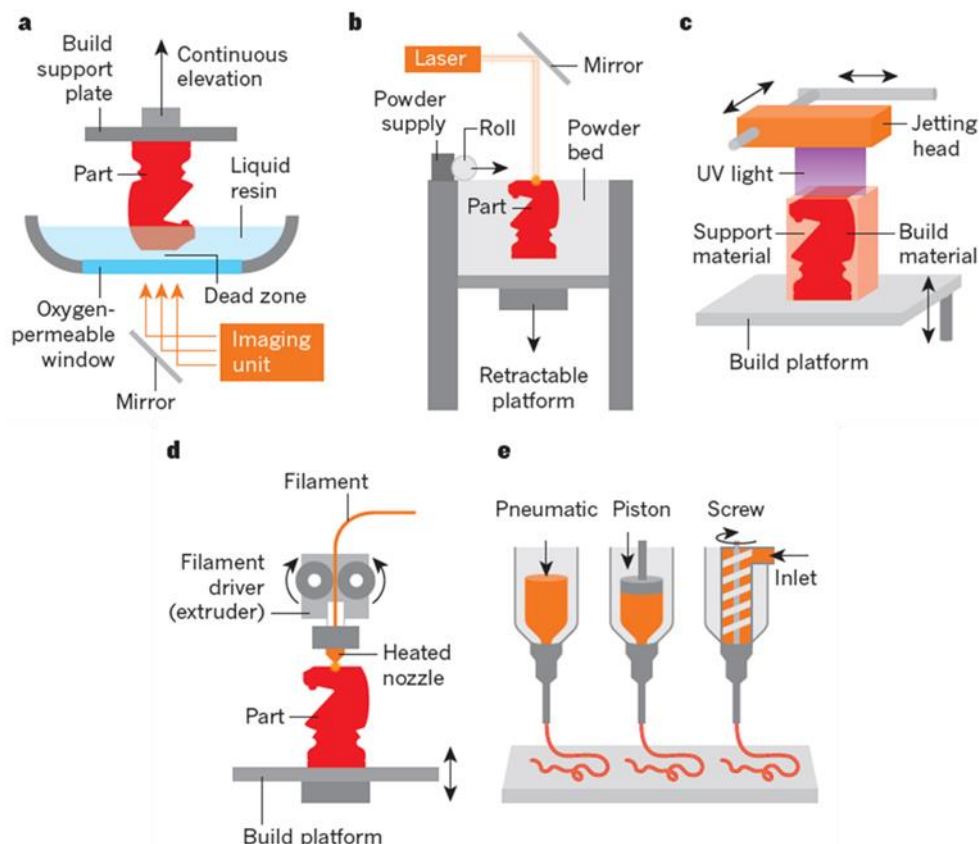
Figure 1. Common light- and ink-based 3D printing methods. (a) The light-based 3D printing method known as continuous liquid interface production. (b) Light-based selective laser sintering of powders. (c) Light- and ink-based photocurable inkjet printing of photopolymerizable resins. (d) Ink-based fused deposition modeling of thermoplastic filaments. (e) Direct ink writing using viscoelastic inks [83].

2.2. Matrix-assisted 3D printing (MAP).

Soft materials such as hydrogels or silicones are very vulnerable to deformation after 3D printing with the DIW method, which limits designs and topologies. For example, when printing the bridged structure, it can easily collapse if there is no proper support. Recently, a method for overcoming the limitations of the DIW method has emerged. A technique called embedded 3D (EMB3D) printing or matrix-assisted 3D printing (MAP), which involves direct patterning of inks within soft supporting matrices along predefined omnidirectional printing path (Figure 2) [70, 84]. Since the soft material is printed inside the supporting matrix, the ink cannot easily be deformed. To date, these technologies have been used in a wide variety of applications, such as manufacturing 3D microvascular networks inside hydrogels or manufacturing soft robots, soft sensors, microfluidic systems, and scaffolds [1, 82, 85-87].
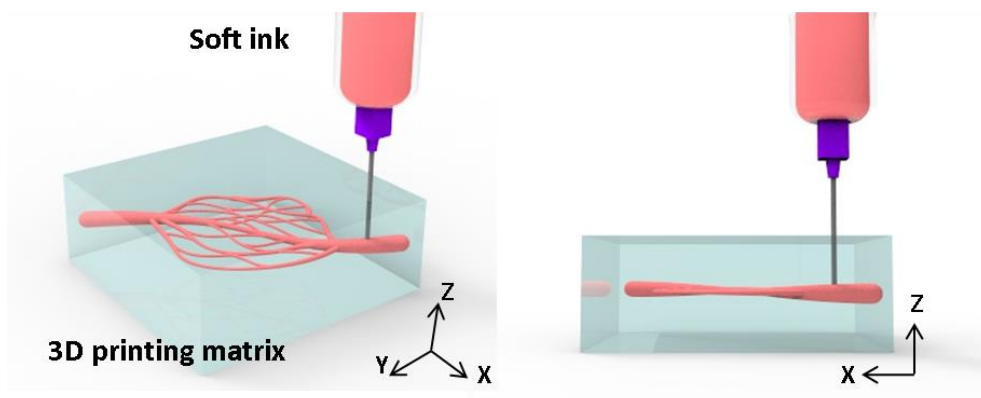
Figure 2. Schematic illustration of matrix-assisted 3D printing (MAP).

2.2.1. Rheological requirements for MAP.

In the early days, three components were essential for the printing concept of MAP. It consisted of matrices with two different rheological properties and single ink [1, 87]. When the ink was printed inside the matrix showing high storage modulus, crevasse was generated along the path of the nozzles. Another matrix having low viscosity was poured on the existing matrix to fill the crevasse. Thus, a multi-component material system had been developed that consists of ink, a matrix with high storage modulus, and a flowable filler matrix. These components were adjusted to exhibit the appropriate rheological properties needed to maintain high printing stability throughout the 3D printing and curing process. Besides, it had the characteristic of being chemically compatible between matrices showing two different rheological properties. Several criteria must be fulfilled when designing a support matrix and filler matrix for MAP. First, the matrix should facilitate the patterning of the desired ink filament without breakage. Second, as the nozzles pass through the matrix, any defects that occur during printing must be quickly healed by the highly fluid matrix.

As technology advances, instead of using multi-matrices, matrix materials began to emerge that allowed self-healing by adequately adjusting the rheological properties with a single matrix [70]. This development had made it possible to print the three-dimensional structures within the matrix through MAP. To secure higher printing stability in the single matrix-based MAP, many researchers have reported appropriate conditions by controlling the rheological properties of the matrix and the ink materials. Ink and matrix materials must meet several requirements to enable MAP. The ink must show shear-thinning property where the viscosity decreases as the shear rate is applied to ensure stable passage through the nozzle [70]. Qualitatively, the ink must have yield stress, and the matrix material must exhibit shear-thinning and yield stress properties as well as the ink. If the shear modulus (G') of ink

is too large for the shear modulus of the matrix, the nozzle can pull the ink in the matrix material. In contrast, if the G' ink is too low compared to the G' matrix, the ink filaments may fragment within the matrix. The matrix must have a yield stress low enough that the nozzle can move freely throughout the matrix. Moreover, the crevasse formed as the nozzles pass should be filled up quickly. However, if the yield stress of the matrix is too low compared to the viscous stress associated with nozzle displacement, the nozzle will create a stress field that deforms the printed structure. If the yield stress of the matrix is too large, a gap is formed behind the nozzle, requiring the introduction of filler fluid to the top surface of the matrix. Thus, to be utilized as matrix material, the matrix must exhibit time-dependent rheological behavior due to dynamic reconstruction at the microscale, and the crevasse of nozzle movement has to be recovered quickly. Besides, the ink and matrix materials must be chemically compatible and exhibit the desired composition and functionality required for the application.

2.2.2. Various matrix systems for MAP.

Unlike the DIW method, MAP always requires a pair of materials, ink, and matrix. Various ink and matrix materials have been reported for various applications and purposes. The various matrix systems are presented in Figure 3.

The first matrix material is the Pluronic F127, a triblock copolymer with a hydrophobic poly (propylene oxide) (PPO) segment and two hydrophilic poly (ethylene oxide) (PEO) segments arranged in a PEO-PPO-PEO configuration [1, 82]. Aqueous Pluronic F127 solutions undergo a phase transition that is both concentration and temperature-dependent. Under ambient conditions, the PEO-PPO-PEO species form micelles that consist of a PPO core surrounded by a PEO corona above a critical micelle concentration (CMC) yielding a physical gel, as reflected by the substantial increase in shear elastic

modulus, G' as the concentration exceeds the CMC. Besides, these Pluronic F127 solutions also possess a critical micelle temperature (CMT) [88-90]. Above the CMT, the PPO block dehydrates leading to pronounced hydrophobic interactions that drive micelle formation. However, below the CMT, the hydrophobic PPO units are hydrated, allowing individual PEO-PPO-PEO species to become soluble in water, thereby inducing a sol-gel transition for systems whose concentration resides above the CMC. This particular rheological property has led many researchers to use Pluronic F127 as a 3D printing matrix.

To mimic the 3D microvascular networks, a fugitive ink, fluid filler matrix, and gel matrix, whose properties were tailored for printing and subsequent transformation into the desired structures were developed. 3D biomimetic microvascular networks composed of a hierarchical 3D branching topology with microchannel diameters ranging from 200–600 μm could be constructed using this system [1]. Embedded vasculatures could also be prepared by patterning bio-inks containing cells inside the Pluronic F127 matrix [82].

Recently, matrices made by adjusting rheological properties such that self-healing property for healing the crevasses formed by moving nozzles have been reported [70]. This technique includes the printing of shear-thinning hydrogel "inks" directly into self-healing "support" hydrogels. The MAP was possible because of their noncovalent and reversible bonds that could be disrupted by the application of a physical stimulus such as shear stress, and that reformed rapidly upon removal of the stimulus. Such properties permitted their use as injectable hydrogels, and consequently, as inks in extrusion-based 3DP. These same properties enabled the use of a guest–host hydrogel as a support matrix, which deformed to accommodate extruded material and self-heals to maintain material localization.

A study has been reported to produce a matrix using gelatin, which is a biocompatible protein material [91]. The additive manufacturing of complex

three-dimensional (3D) biological structures using soft protein and polysaccharide hydrogels were challenging to create using traditional fabrication approaches. These structures were built by embedding the printed hydrogel inks in a hydrogel matrices that serves as a temporary, thermoreversible, and biocompatible support.

Besides, a cross-linked acrylic acid-based matrix has been reported [84]. This material, called Carbopol, has the form of a granular gel and is considered to be the best matrix material to date. Gels made from soft microscale particles smoothly transition between the fluid and solid states, making them an ideal matrix in which to create macroscopic structures with microscopic precision. While tracing out spatial paths with an injection tip, the granular gel fluidizes at the point of injection and then rapidly solidifies, trapping injected material in place. This physical approach to creating three-dimensional (3D) structures negates the effects of surface tension, gravity, and particle diffusion, allowing a limitless breadth of materials to be written. With this method, silicones, hydrogels, colloids, and living cells were used to create complex large aspect ratio 3D objects, thin closed shells, and hierarchically branched tubular networks.

Numerous researchers have sought to fabricate the final product into devices, not just 3D printing. The most suitable material for this purpose was silicone. Silicone is a soft material with elasticity through the hardening process and has been applied in various applications such as microfluidics, sensors, actuators, and soft electronics [92-94]. A study has been reported in which ink consisting of carbon black particles was printed on silicone oil to produce a three-dimensional strain sensor [87]. Conductive carbon grease displayed the rheological properties required for 3D printing.

Silicon matrix has also been reported for its application in soft robotics as well as strain sensors [86]. The Pluronic F127 hydrogel, which can be easily removed to form a channel in the silicon matrix, was printed. And the catalyst

was prepared in a hydrogel form that would act as a power source. Two hydrogel-based inks were printed within the molded matrix materials. These printed features were interfaced with each other as well as with the soft controller through the use of 'fugitive plugs' introduced at the inlets of the controller before filling the mold with the matrix materials. The catalytic ink contains platinum particles suspended in a mixture of Pluronic F127-diacrylate and poly (ethylene glycol) diacrylate that is photo cross-linked after printing.

A granular organic microgel system was used as an oil-based 3D printing support matrix [95]. The organogel particles were formed through the self-assembly of diblock and triblock copolymers dispersed at low concentration in mineral oil, in contrast to traditional polymerization routes to synthesizing microgels. 3D printing was performed by translating an injection needle through the organogel medium while depositing features made from numerous silicone-based materials. Silicone features as small as 80 mm could be printed and remain indefinitely stable without cross-linking. The breakup of unstable features could be delayed markedly by increasing the viscosity of silicone inks, allowing even higher-precision (30 mm) structures to be manufactured.
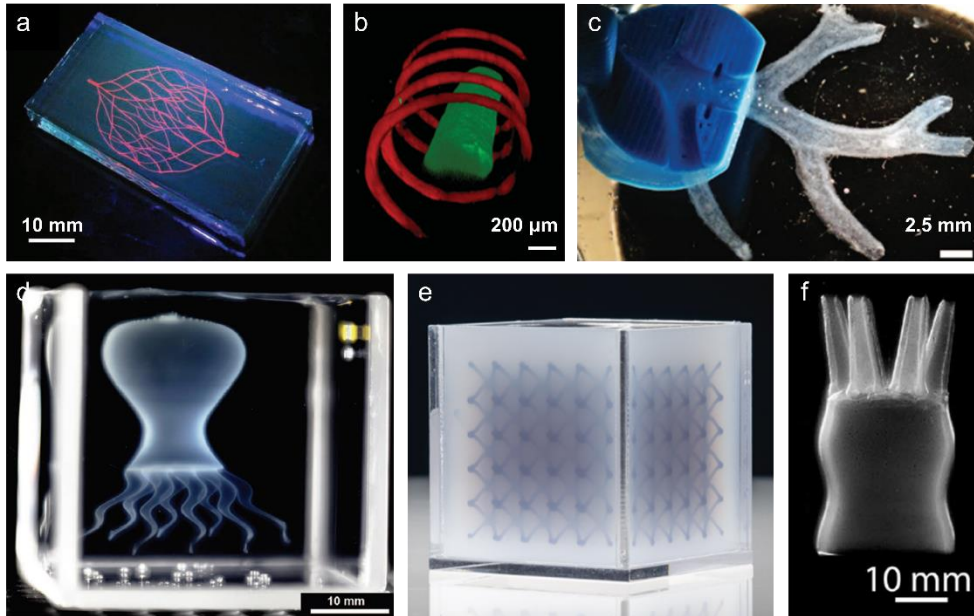
Figure 3. Various matrix systems for MAP. (a) Fluorescent image of a 3D microvascular network fabricated via omnidirectional printing of a fugitive ink within a photopolymerized Pluronic F127-diacrylate matrix [1]. (b) Confocal images of a filament of a fluorescein-labeled ink and then a continuous spiral of a second, rhodamine-labeled ink printed into a self-healing hydrogel matrix [70]. (c) A dark-field image of the arterial tree mounted in a perfusion fixture to position a syringe in the root of the tree [91]. (d) A thin-shell model octopus is made from multiple connected hydrogel parts in a cross-linked acrylic acid matrix [84]. (e) Optical image of matrix-assisted 3D printed architectures, including a body-centered cubic lattice [96]. (f) Macroscopic image of a perfusable network of hollow vessels being 3D-printed into the micro-organogel matrix material [95].

15

2.3. Cellulose.

Cellulose is one of the most abundant natural macromolecular organic compounds on the planet and is produced by billions of tons every year as long as solar energy is present [97]. Therefore, many researchers actively developed the technology to utilize the cellulose component of the plant as a resource of energy, chemicals, or food for the future. Recently, the importance of cellulose to resource and environmental issues is increasing. Cellulose-based wood has long been used in energy sources, apparel, housing, ships, and many other fields. In conclusion, the study of cellulose resources is the most important field to meet the human desire for new materials and new energy.

Cellulose is a carbohydrate polymer composed of 44.4% carbon, 6.2% hydrogen, and 49.4% oxygen [98]. It is a linear polymer composed of the monosaccharide glucose, β-D glucose. Cellulose is a condensation polymer in which β-D glucose is connected as the hydroxyl group attached to C1 of one glucose molecule and the hydroxyl group attached to another C4. The link between molecular units is called 1, 4-β-D-glucosidic bond or β-glucosidic oxygen bridge. Multiple condensation reactions result in linear polymer chains that are very long and do not have side branches. The degree of polymerization, representing the length of the polymer chain, can reach up to 10,000 anhydroglucose units. The molecular formula of the anhydroglucose unit, which is a repeating unit, is $C_6H_{10}O_5$; thus, the molecular formula of cellulose can be specified as $(C_6H_{10}O_5)_n$ [99]. Cellulose is obtained from various sources such as cotton and wood, but the chemical structure is the same. There is only a difference in content and degree of polymerization, molecular weight. Cotton, for example, contains more than 95% of cellulose and about 50% to 60% of wood [98, 100].

Cellulose is a linear polymer, but its structure is very complicated due to the strong intermolecular bonds between cellulose molecular chains.

Cellulose generates strong hydrogen bonds between the chains due to the many hydroxyl groups. This hydrogen bond is enhanced by successive alternating steric arrangements of anhydroglucose units. Thus, cellulose is highly crystalline, regardless of its source. The region with very high crystallinity is the region where hydrogen bonds are maximized, and the cellulose molecules parallel to each other are tightly arranged. Cellulose does not dissolve in some chemicals because the crystalline regions are difficult for chemicals to penetrate. Ramie, cotton, and flax contain 60-87% crystalline cellulose, while wood is 50-65%.

2.3.1. Cellulose nanofiber (CNF).

Cellulose particles that are more than one dimensional on the nanoscale (1-100 nm) are called nanocelluloses. Different terms in various cellulose nanotechnology and various technical committees and organizations (ISO TC 6 and TC 229; TAPPI and CSA Z5100-14) have been reported, such as nanofibrillated cellulose (NFC), microfibrillated cellulose (MFC) or cellulose nanofibers. Although the work of standardizing this has not yet been completed, most experts use the term "cellulose nanofibrils" for nanocellulose.

Bacterial cellulose (BC) and electrospun cellulose nanofibers (ECNF) are also considered nanocelluloses. Cellulose nanocrystal (CNC) and cellulose nanofibrils (CNF), however, are much more common because they are produced by breaking down cellulose fibers into nanoparticles (a top-down process). On the other hand, BC and ECNF are produced by the accumulation of nanofibers (a bottom-up process) from small molecules, which makes the mass production of BC and ECNF still in doubt. Regardless of the type of nano cellulose, it shows hydrophilicity, relatively large specific surface area, and enormous potential for surface chemical modification.

2.3.2. Extraction methods of CNF.

Cellulose is present with hemicellulose and lignin in trees or plants. The latter is generally removed before manufacturing CNF by various cooking and bleaching methods similar to those used in the paper industry. The CNF production method generally involves several operations: purification, enzymatic hydrolysis, repurification, and final homogenization. Therefore, the CNFs with different characteristics could be produced depending on the production process. The CNFs produced by these various methods show different morphological characteristics. In particular, nanofiber dimensions and the amount of residual fine fiber fragments, surface chemistry, crystallinity, and DP are different.

Dry cellulose pulp can be broken down into small pieces using mechanical methods. However, it usually leads to fiber breakage instead of fibril exfoliation. As a result, CNFs with a low degree of polymerization, low crystallinity, and low aspect ratio are produced. So the mechanical properties of subsequent nanomaterials are relatively weak. The energy must be exceeded over the hydrogen bond between the fibers to exfoliate rather than cut the nanofibers. For this reason, CNF is generally produced in aqueous media, which loosens hydrogen bonds between fibers. In general, cellulose is dispersed at low concentrations (<5%) due to its high water absorption, creating a high viscosity suspension. Refining, homogenization, and grinding are the most common techniques used to produce CNF. These techniques are most efficient for exfoliation of fiber cell walls and CNF separations and are suitable for upscaling. Therefore, it is currently used for the industrial pilot production of CNF.

Producing CNF using only mechanical decomposition requires high energy and cost [101, 102]. Since the beginning of the CNF research, intensive research has been carried out to improve the degree of nanofibrillation and reduce energy demand. Recent methods of CNF production include various

biological and chemical pretreatments. This type of pretreatment has a significant impact on the CNF output. The top-down process for cellulose nanofiber extraction is described in Figure 4.

Some enzymes are known to promote hydrolysis of cellulose and to enhance nanofibrillation. Cellulase was used to improve cellulose fibrillation in the papermaking process [103]. Since then, extensive research has been carried out, from mild enzymatic hydrolysis to facilitate the purification process, to strong hydrolysis to convert cellulose to glucose for further production of bioethanol. Recently, the production of CNF with mild enzyme hydrolysis has been reported [104, 105]. In these studies, the single component endoglucanase, Novozym 476 was used as the enzyme.

The introduction of negatively charged (carboxyl or carboxymethyl) groups on the fibers is known to improve the exfoliation efficiency of nanofibrils. This is caused by the electrostatic repulsion between negatively charged cellulose nanofibrils [106, 107]. Based on the same principle, sulfurous acid pulp is known to be easier to peel than conventional kraft pulp. 2,2,6,6-tetramethylpiperidine-N-oxyl (TEMPO) was reported for improving nanofibrillation since 1993 [108]. TEMPO is radical for the selective oxidation of monosaccharide primary alcohol groups, and this process has become one of the most popular topics in the field of selective oxidation of cellulose.

Carboxymethylation is another way for cellulose pretreatment. Carboxymethyl cellulose was first manufactured in 1918 and already commercially produced in Germany in the early 1920s [109]. The production of CNF from carboxymethylated cellulose as a new type of material was described. Carboxymethylated cellulose fibers were prepared by chemical pretreatment to remove unfibrillated fibers by high-pressure homogenization, sonication, and centrifugation. Nanofibrillated cellulose had a cylindrical cross-section of 5-15 nm in diameter and up to 1 μm in length.
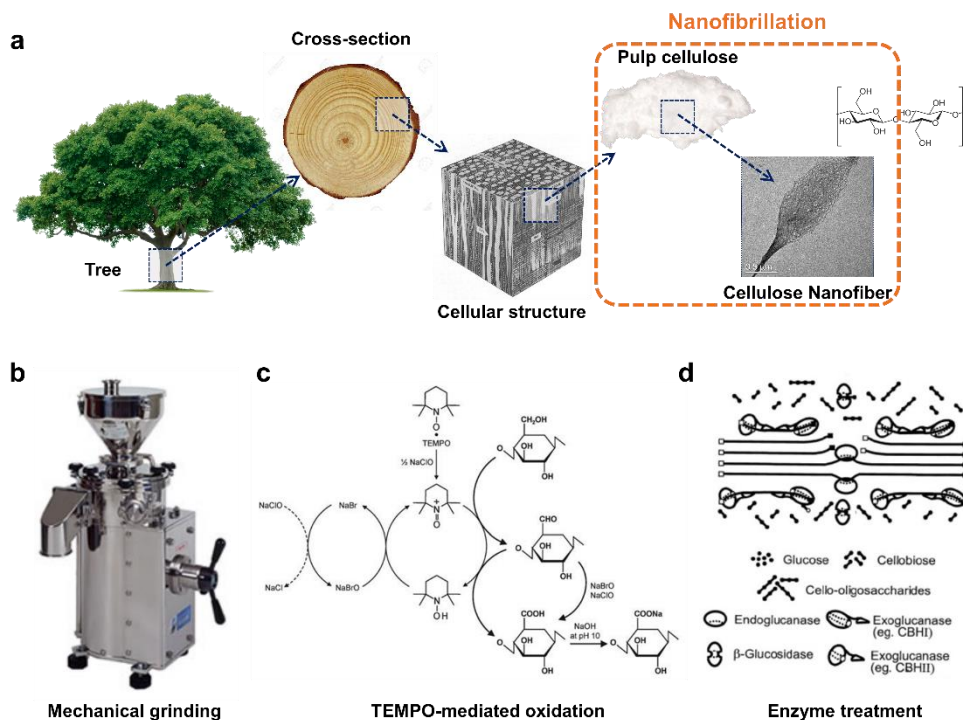
Figure 4. Top-down process for cellulose nanofiber extraction. (a) Hierarchical structure of wood: from tree to cellulose, (b) Image of mechanical grinder, (c) Regioselective oxidation of C6 primary hydroxyls of cellulose to C6 carboxylate groups by TEMPO/NaBr/NaClO oxidation in water at pH 10–11 [12]. (d) The enzymatic hydrolysis model of cellulose.

2.3.3. Rheological properties of CNF.

The rheological properties are critical for the design and operation of some processes such as pumping, mixing, storage, and extrusion. Therefore, understanding how to control the rheological behavior of CNF suspensions is essential to utilize the functionality of the material. Besides, the mechanisms controlling the rheological properties of CNF suspensions could be applied to other nanofiber types of suspensions.

CNF suspension has gel-like behavior at concentrations of 1.0% and has very complex rheological properties [105, 110]. CNF suspensions exhibit both pseudoplastic and thixotropic properties [111, 112]. Flowing the CNF suspension requires deformation of the individual flocs and deformation of the three-dimensional fiber network. Regardless of the production conditions, all types of CNF suspensions decrease in viscosity with increasing shear rate showing shear-thinning properties. CNF has a thixotropic property, that is, a viscosity decreases when a stable shear rate is applied, and when the shear rate decreases to zero, the viscosity rises again to the same level. Therefore, time dependence is significant, so it is essential to measure steady-state flows. Viscosity and shear stress increase as a function of CNF concentration. As mentioned above, these suspensions have shear-thinning behavior, which is observed at a wide range of shear rates. In many studies, the Newtonian plateau was reported between low and high shear rate regions, and hysteresis loops were observed when increasing and decreasing shear rates. It is noteworthy that the Newtonian plateau and hysteresis were both observed with or without chemical pretreatment. These were associated with the formation and destruction of shear-induced structures in CNF suspensions.

CNF suspensions form a network structure with a low solids content. Oscillatory shear measurements are typically performed to study the linear viscoelastic properties of these structures. Oscillatory strain sweeps are performed to determine the strain domain where the linear strain viscoelastic

regions, the storage (G') and loss (G") modulus, are independent of the strain. The oscillatory frequency measurements are performed on strains in the linear viscoelastic region. An example of linear viscoelasticity measurements for TEMPO-oxidized CNF suspensions at various concentrations (0.5-1.5 wt%) is reported [113]. After exceeding the critical strain (about 1%), the elastic CNF network is destroyed, which is reflected by the nonlinear behavior of the dynamic modulus. The CNF suspension forms a gel even at low concentrations. This is confirmed by G'> G", where G' and G" are parallel to each other and mainly frequency independent. These gel-like properties have been reported for CNF suspensions at low concentrations of 0.125% corresponding to the gel point, after which the nanofibrils begin to form interconnected networks. As the concentration of CNF increases, a stronger fibrous network is formed, which increases the dynamic modulus widely reported in other studies [111, 114-116].

2.4. CNF as a 3D printing material.

Cellulosic materials without chemical modifications are generally considered unsuitable for extrusion or sintering based 3D printing because cellulose decomposes on heating before it melts and fluidizes. On the other hand, CNF hydrogel exhibiting shear-thinning behavior can be considered as an ink material for 3D printing. The rheological properties of CNF already mentioned are considered to be very suitable for use as 3D printing inks [57, 117-121]. A new era is coming with 3D printing using cellulose materials to replace synthetic plastic materials (Figure 5).

2.4.1. CNF as a rheology modifier.

Inks properties are of critical importance in 3D printing [122]. In particular, 3D printing inks require a well-controlled viscoelastic response (high viscosity and shear-thinning behavior) [122-127]. The shear-thinning properties of polymer solutions were often used to achieve this result. CNF has been used as the viscosity modifier in a wide range of industrial products for many years. The cellulose chains can form hydrogen bonds between each other, restricting the water motion and further increasing the viscosity. However, when an external force is added, the mixing energy will break the hydrogen bonds between cellulose chains, and subsequently, the chains will be aligned in the direction of flow, leading to decreased viscosity through shear-thinning or pseudoplastic behavior [128]. The rheological properties of CNF, therefore, provide the desired low viscosity at high shear rates, while providing high viscosity as the high shear rates are stopped. The thixotropic property of CNF makes them reasonable 3D printing inks.

CNF in hydrogel stands out as a biomaterial in bio-ink due to its low cytotoxicity and structural similarity with ECM. CNF was first proposed to manufacture scaffolds for application by tissue engineering using inkjet printing techniques [126]. Carboxymethylated nanocellulose also

successfully printed on a TEMPO-mediated oxidized nanocellulose film [129]. In order to improve the printing stability of the ink, the CNF hydrogel can be formulated with auxiliary materials, which can be mixed with CNF to control the rheological properties of the ink. Besides, as the CNF addition amount increased, it was possible to secure structural stability when forming the three-dimensional structure of the ink. As ink modifiers, water-soluble lignosulfonate (LS) could also be added to the 2% CNF obtained through enzymatic hydrolysis to control the rheological properties. Ionically cross-linked alginates can be formulated by combining the concentration of 2.5% CNF and alginate obtained through mechanical treatment and enzymatic hydrolysis when shape fidelity was improved [121, 126, 130].

As a result of tremendous interest in natural cellulose-based bio-inks, it is commercialized under the trademark CELLINK by CELLINK AB (Sweden). CELLINK can be prepared from 2% plant-derived CNF and 0.5% alginate. Using CELLINK, the structure of the ear with pores and cartilage cells with high shape fidelity can be produced. Various studies have been made to manufacture bio-inks by compounding photocurable polymers with CNF. Representatively methacrylated gelatin (GelMA) was used with CNF hydrogels as a photocrosslinkable material naturally derived from collagen with properties to improve biological interactions [119].

2.4.2. CNF as a reinforcement.

CNF has been studied as a novel nanofiller to reinforce materials [131-133]. Many researchers carried out a biomimetic 3D printing study using wood-derived CNF as a stiff filler [134]. The composite architectures were printed with a hydrogel composite ink containing stiff CNF that had been embedded in a soft acrylamide matrix mimicking the composition of plant cell walls. The CNF underwent shear-induced alignment as the ink flowed through the deposition nozzle during printing, producing printed filaments with

anisotropic stiffness, and hence, swelling behavior in the longitudinal direction (defined by the printing path). CNF alignment was directly observed in the printed samples compared to isotropic cast sheets of the same material. CNF was adopted to improve the mechanical performance of polylactic acid (PLA) in 3D printing [135, 136]. The incorporation of PLA-g-CNFs improved the storage modulus of the composite filaments both below and above the glass transition temperature, which could be due to the increased crystallinity of the PLA matrix.

3D printing of polypropylene (PP) is difficult, due to not only the high temperatures required for PP to be printed but also due to shrinkage and warping during the printing process. To overcome the shrinkage and warping problem, CNF was incorporated into PP because CNF has a low thermal expansion coefficient of 0.1 ppm/k [137]. The composites were prepared through mixing CNF and PP pellets in a twin-screw co-rotating extruder. Rheological tests showed that the elastic modulus, complex viscosity, viscosity, and transient flow shear stress of PP were all increased with the addition of 10 wt% CNF, while the creep strain of PP was reduced. Flexural strength and modulus of PP were also improved by adding CNF.

Figure 5. Cellulose as a 3D printing material. (a) 3D printed specimens of wood flour/PLA composites for tensile properties measurement [138]. (b) 3D printed cellulose acetate-based miniature eyeglass frames [139]. (c) 3D printed cellulose nanocrystal grids [117]. (d) Simple flowers composed of 90°/0° bilayers oriented with respect to the long axis of each petal, with time-lapse sequences of the flowers during the swelling process [134]. (e) A small chair is printed with CNF and freeze-dried [140]. (f) 3D printed octopus structure from 2.8 % T-CNF gel [120]. (g) Top view of 3D-printed "letters" after cross-linking and freeze-drying of CNF [141]. (h) 3D printed human ear with CNF/alginate bio-ink [126]. (i) 3D printed human nose structure with CNF/GelMA bio-ink [119].

2.5. CNF based devices.

CNF stabilized by hydrogen bonds that form highly crystalline domains. Thus, cellulose nanofibers have a CTE of 0.1 ppm/K, lower than quartz and glass, and estimated strength of 2-3 GPa, 5 times stronger than mild steel. Nanofibers also show excellent heat transfer properties comparable to glass. Optically transparent TEMPO-oxidized CNF nanopaper can be used as an alternative to traditional substrates (glass, plastic, and plain paper) in a variety of applications such as smart sensors, flexible energy storage, wearable electronics, and optoelectronic devices (Figure 6) [9, 142-150].

2.5.1. Transparent and thin device through dehydration.

Aqueous dispersed CNF can be obtained in a system that is disintegrated in water during CNF manufacturing. CNF aqueous dispersion can be actively utilized due to its unique rheological property, as mentioned above. However, if CNF film is manufactured through dehydration and drying, CNF thin films with unique properties can be obtained. An essential property of CNF is that light scattering can be suppressed [9, 142]. If the nanofibers are densely packed, and the gaps between the fibers are small enough to avoid light scattering, the cellulose material can maintain a high level of transparency.

The optical haze and transmittance of the transparent paper can be adjusted by the porosity and size of the fiber [151-153]. It is important to design transparencies with adjustable optical properties in an inexpensive process. Recently, cellulose was used to investigate very transparent paper. Plain wood fibers act as a scaffold for paper, while CNF fills voids to reduce light scattering. Since CNF has an optical index of refraction 1.5 that is similar to regular fibers in contrast to air, the paper can be adjusted from opaque to transparent, depending on the amount of space filled with CNF. Hybrid paper has the same transmittance of 91.5% as PET when the CNF concentration of the paper reaches 60%. The haze of hybrid paper is much higher than that of

27

PET. In optoelectronic devices such as thin transmissive solar cells, high transmittance and high haze presence would be desirable. The efficiency of thin-film solar cells will increase with improved light trapping. Other applications of hybrid paper are used as outdoor electronic displays such as GPS (Global Positioning System), iPad, or mobile phones. The higher the haze, the less glare from strong light sources.

2.5.2. Electronic devices.

Many electronic materials require high transparency and flexible properties. CNF is a material that is rapidly expanding its application to meet these demands. CNF is not conductive in itself but is highly applicable as a substrate for printing [154-156].

Thin-film transistor (TFT) has recently been demonstrated in transparent paper with a smooth surface [143, 157]. Transparent nanopapers are used as substrates that do not require surface coating due to nanoscale surface roughness, making them compatible with typical TFT device structures. Transparent and conductive CNT films were printed as transparent gates.

Flexible OLEDs use plastic substrates that have thin, smooth, and optically transparent and have excellent blocking properties against oxygen and water. Transparencies have nanoscale smoothness, and optical properties can be adjusted from optically transparent to optically blurred, which is advantageous for flexible OLED devices in a variety of applications [158, 159]. OLEDs with high haze have a wide angle of light distribution for illumination, and OLEDs with low haze paper have high clarity for indoor displays.

Several groups have proved CNF as a substrate for hosting antennas due to its foldability, printability, lightweight, and low cost [145, 160, 161]. The return loss of the nanopaper antenna is much lower than that of plain paper due to the smooth surface. Just as plastics have replaced glass of flexible

electronics, transparent paper can replace plastics in printed green electronics. Universities, government research institutes, and industries are interested in transparencies of CNF for the next generation of green electronics.

2.5.3. Biological and chemical sensing devices.

Sensor is theoretically defined as a transducer that converts one form of energy into other amenable forms for further processing. Many types of sensors including gas sensors, chemical sensors, capacitive sensors, UV sensors, and strain sensors have been well established in both academic and industrial research for energy science and technology. From the viewpoint of sensor materials, there was a prerequisite requirement on simple, sensitive and stable features suited for trace detection in a wide spectrum of applications ranging from lab-on-a-chip and in vivo biosensor to environmental monitoring and warfare agent detection, as opposed to the often employed sensitive, bulky and complicated instrumental methods. It is commonly known that in order to use sensors with higher efficiency, it must be compact, have a high speed for receiving and distribution for signal, be immune to environmental variation as well as able to resolve position down to the atomic scale. For the cellulose-based composite communities, cellulose has been applied in many activities of sensor materials. It is important to note that cellulose can be effectively prepared as hydrogel and composite form [162-165]. The structure of cellulose can be further designed to be sensitive in nano-scale structured materials, leading to several versatile applications of the sensor.

Among the cellulosic materials, CNF has recently researched as a SERS substrate due to its transparent optical properties and the structural properties of nanofibers intertwined in a three-dimensional network [166, 167]. High-performance SERS substrates based on cellulose nanofibers (CNF) and gold nanoparticles (AuNPs) were reported [168, 169]. The unique structure and

excellent flexibility of the CNF-AuNP nanocomposite are SERS substrates for rapid trace detection. Flexible and transparent SERS-activator with 2,2,6,6-tetramethylpiperidine-1-oxy (TEMPO)-oxidized CNF and AuNPs of gold nanospheres (AuNS) or gold nanorods (AuNR) also presented [170].

2.5.4. Cell culture devices.

The use of CNF has attracted greater attention in the field of biomedical engineering as a scaffold for tissue engineering or cell culture. Various researchers performed incubation of mesenchymal stem cells (MSCs) on cellulose-based substrates [171, 172]. Most of this work has been done recently and focuses on bacterial nano cellulose substrates rather than CNFs produced in wood. [173, 174] Mouse MSCs were used for fat production differentiation using bacterial nanocellulose and alginic acid scaffolds. BNCs have been used alone as a scaffold. Horse MSC differentiated from seeded BNC scaffolds and differentiated in vitro differentiation of cell viability, proliferation, adhesion, and supportive cartilage and bone formation differentiation [174]. The CNC was dispersed in poly (lactic acid) and then electrospun to create scaffolds and tested with human MSCs for basic cell compatibility. CNF hydrogels were made with gelatin and tested them with human MSCs. Recently, research has been conducted to utilize CNF as a substrate for culturing MSCs [175]. In manufacturing CNF film, the heat treatment gave a change in the properties of the CNF film, and the behavior of MSCs was observed according to the change.
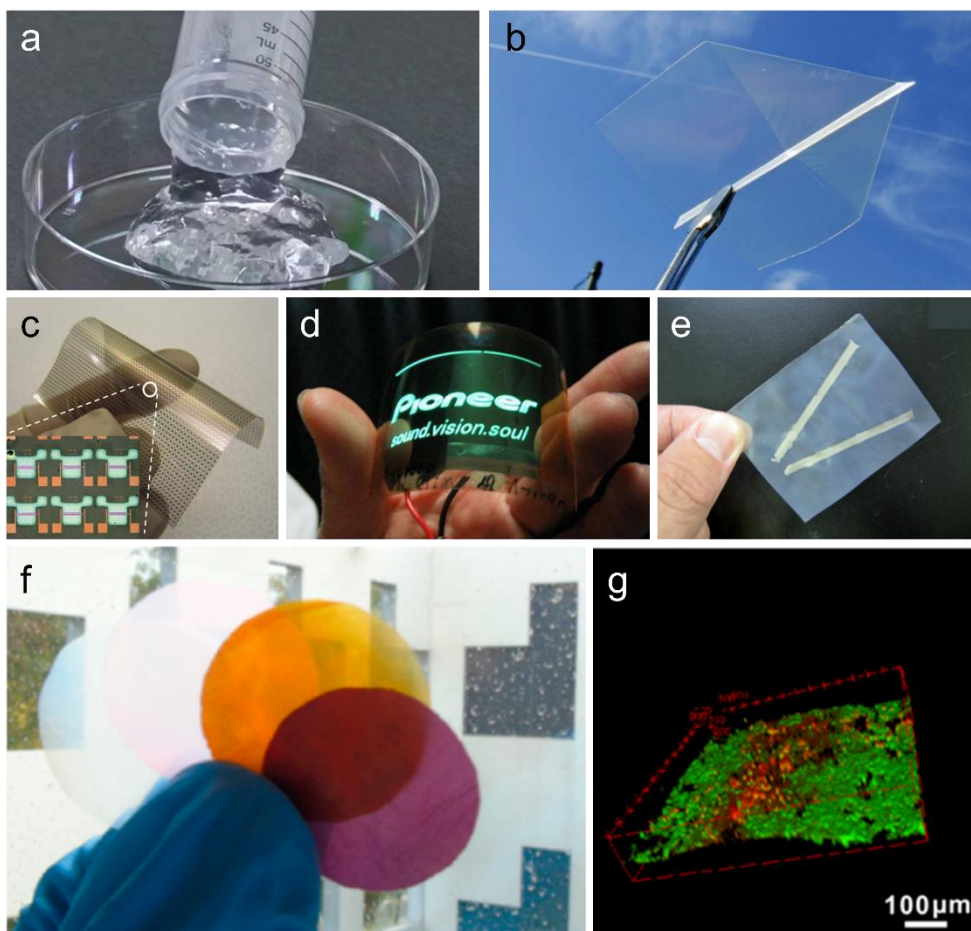
Figure 6. CNF based devices. (a) Optical image of CNF hydrogel. (b) Transparent CNF film [9]. (c) Photograph and optical microscopy image of 20 μm-thick transparent CNF-based OTFT array [157]. (d) Luminescence of an organic light-emitting diode deposited onto a flexible, low-CTE, and optically transparent CNF nanocomposite [158]. (e) V-shaped silver nanowire lines on CNF film [145]. (f) CNF based optical sensing platform [176]. (g) 3D views of live/dead staining of MCF-7 cells in the matrix and HUVECs in CNF film [177].

III. Materials and Methods

3.1. Preparation and characterization of the CNF matrix.

A CNF hydrogel was produced from kraft pulp (Moorim P&P, Ulsan, Korea). Before carboxymethylation and nanofibrillation, the pulp fibers were beaten using a laboratory valley beater for 30 min. Beaten pulp fibers were carboxymethylated, and the procedure proceeded as follows. The wet pulp (dry weight, 70 g) was solvent-exchanged to ethanol. The solvent-exchanged pulp was immersed in a solution of isopropanol (3200 ml)/ methanol (800 ml) with sodium hydroxide (11.2 g), and the mixture was heated at 65 °C under continuous stirring for 60 min. The reaction was initiated by the addition of monochloroacetic acid (14 g, Sigma-Aldrich, St. Louis, MO, USA) and stirred. The reaction time was controlled from 30 min to 90 min. The carboxymethylated cellulose fiber was solvent-exchanged using distilled water at pH 7.0 and passed through a grinder (Super Masscolloider, Masuko Sangyo Co., Ltd., Japan) to produce the CNF hydrogel. The concentration of the pulp suspension during grinding was 1.5 %. The operation speed and the gap distance between the grinder stones were 1500 rpm and −100 μm, respectively. The number of passes through the grinder was adjusted until no more CNF viscosity increased.

The carboxyl group content of the carboxymethylated pulp was determined using a conductometric titration method. This method describes the analysis of the total acidic content of pulp fiber, and the term of the total acid group was replaced by carboxyl group content. Briefly, 1 g of carboxymethylated pulp in sodium form was converted to the proton form until all acid groups received H$^+$ as counter-ions and then titrated with 0.01 mol/l NaOH. The total amount of the carboxyl group was calculated according to Equation (1):

$$\text{Carboxyl group content} = (C_{\text{NaOH}} \times V_{\text{NaOH}}) / w \quad \text{Eq. (1)}$$

Where C_{NaOH}, V_{NaOH}, and w are the concentration of the NaOH solution, the volume of the NaOH solution consumed at a flat area, and the oven-dry weight of the sample, respectively.

The chemical structure of the CNF was characterized by Fourier transform infrared spectroscopy (FT-IR spectroscopy, Nicolet iS5, Thermo Scientific, USA) in the range of 4000–500 cm^{-1}, and 32 scans with a resolution of 4 cm^{-1}.

The surface topography of CNF and fiber dimension were imaged using atomic force microscopy (AFM, XE100, Park Systems, Suwon, Korea) in a non-contact mode (PPP-NCHR 10M, Nanosensors, Neuchâtel, Switzerland) at the scan rate of 0.6 Hz for surface areas of 1.2×1.2 μm^2.

The zeta-potential values of CNF suspensions were measured by Zetasizer Nano ZS90 (Malvern Instrument, U.K.). The concentrations of CNF according to the degree of substitution were 0.1 %.

The transparency of CNF hydrogels was measured by UV-vis spectroscopy (Synergy HT, BioTek, Winooski, USA). The wavelength range was set to 400-800 nm, which is the visible light region, and the 0.5 % concentration of CNF samples were measured.

3.2. Preparation of various types of ink.

3.2.1. Cross-linked polyacrylic acid-based model ink.

Cross-linked polyacrylic acid (Carbopol 940) was selected as a model ink for evaluating the printing fidelity of the CNF matrix. Cross-linked polyacrylic acid was dissolved in distilled water at 0.5 % to prepare 30 ml. 400 μl of 1 % NaOH solution was added to increase the viscosity. Cross-linked polyacrylic acid ink was centrifuged at 3000 RPM for 3 minutes to degas.

33

3.2.2. CNF based bio-ink.

As another hydrophilic functional ink, CNF hydrogel which mainly used in this study as a matrix material was chosen for living cell printing. Carboxymethylated CNF was prepared at a concentration of 0.75 % to use as a cell containing bio-ink. The CNF preparing details are the same as the method of manufacturing the CNF matrix. To prepare the bio-ink precursor solution, the CNF was steam sterilized (100 kPa at 121 °C for 20 min) in an autoclave. CNF bio-ink was prepared in 3T3 cell culture medium (Dulbecco's minimal essential medium (DMEM) with 4.5 g/l glucose, L-glutamine, sodium pyruvate, and 10 % fetal bovine serum (FBS)). 1×10^6 cells/ml NIH 3T3 cells were added to the CNF bio-inks.

3.2.3. Petroleum-jelly based removable ink.

The removable ink for matrix-assisted 3D printing was prepared by mixing petroleum jelly (Sigma-Aldrich) and liquid paraffin (Sigma-Aldrich) at the ratio of 3:1. The mixed inks were heated to 70 °C, vigorously stirred for 1 min, and degassed in a planetary centrifugal mixer. 0.1 wt % fluorescent microparticles were added to the petroleum-jelly inks to visualize under UV illumination.

3.2.4. Silicone ink-based curable ink.

A commercially available Sylgard 184 was used to prepare the silicone-based ink. Part A and Part B were mixed at a 9:1 ratio, and then the viscosity was increased by incorporating 10 % fumed silica nanoparticle (7 nm). After that, Thi-vex, a silicone thickener, was added to adjust the viscosity to prepare a hydrophobic silicone ink. After centrifugation at 3000 RPM for 10 minutes, the gas was taken out.

3.3. Rheological properties of CNF matrices and inks.

The rheological behavior of the CNF hydrogels and the model inks was characterized using a digital rheometer (MARS III, ThermoScientific, Newington, NH, USA) fitted with a parallel plate geometry (35 mm radius). Before rheological characterization, the CNF hydrogel and the model inks were vigorously stirred and degassed by centrifuging at 3000 rpm for 5 min. Samples were placed on the plate and subjected to stress-sweep experiments, employing a stress range from 0.1 to 1000 Pa at a frequency of 1 Hz at 25 °C. The measurement of the shear viscosity was performed in Rot Ramp mode at shear rates from 0.1 to 1000 s^{-1} with a gap size of 1.0 mm. Rheological measurements of thixotropic time demonstrate the recovery of elasticity. The shear rate is plotted for a constant applied stress, immediately after reducing the stress below the yielding threshold.

3.4. Matrix-assisted 3D printing of single-line.
3.4.1. Matrix-assisted 3D printing of straight line.

The structures were designed using the commercially available Rhinoceros software (Rhinoceros 5.0, Robert McNeel & Associates, Seattle, WA, USA). The designed 3D models were translated into G-code instructions for the deposition stage using 3D-printing slicing software (Cura, Ultimaker, Geldermalsen, Netherlands). All printing paths were generated by writing the appropriate G-code commands. Before printing the path designs, CNF hydrogel was poured into a Petri dish at 25 °C, and the cross-linked acrylic acid-based model ink was poured into the syringe. The nozzle tip was inserted to the bottom center of the CNF matrix in the Petri dish, and the G-code was sent to the printer using the host software. The ink was extruded through a 160 μm inner diameter of nozzle installed in a 5 ml syringe. The extruding volume and the thickness of the lines were controlled with applied pressure and printing speed.

3.4.2. Matrix-assisted 3D printing of angled line.

When printing an angled line, the angle was set to 90°. That is, the ideal angle (θ_i) was 90°. The measured angle (θ_m) was observed with an optical or fluorescence microscope. The difference angle (θ_d) between the ideal angle and the measured angle was analyzed. Angled lines were printed while increasing the concentration of the CNF matrix from 0.25 to 1.5%, and printing was performed on the matrix prepared according to the carboxylic content of CNF.

$$\theta_d = |\ \theta_i - \theta_m\ | \qquad \text{Eq. (2)}$$

3.5. Matrix-assisted 3D printing of multi-lines.
3.5.1. Matrix-assisted 3D printing of multi-lines.

In order to evaluate the printing fidelity in the printing of multi-lines, the printing paths were set in three different ways, and the concentrations of the CNF matrix used were set from 0.25 to 1.5%. The outer diameter of the printing nozzle was 300 μm, and the printing speed was set to 1 mm/s. The printing paths were set up with three different ways to form an intersection. The first path was designed the vertically drawn lines to join each other, and the second one was designed the four lines separately to form an intersection. Lastly, the two straight lines were designed to cross each other.

3.5.2. Particle Image Velocimetry (PIV) test.

Fluorescent particles (0.1 wt %) was added to visualize the flow field with PIV. A petri dish was filled with 5 g of each fluorescent particle-laden CNF matrix before carrying out the PIV measurements. An apparatus was built to extend over the microscope (iRis™; Logos Biosystems, Korea) to image during the print nozzle translation. A 1D motion controller was attached to a post and suspended over the microscope.

The PIV images were analyzed with Matlab (PIV lab). The average background noise is subtracted from all PIV images. The velocity vectors are obtained by applying 2D cross-correlations of the particle distribution with multiple interrogation windows of 64×64 pixels with a 50 % overlap for the coarse grid and 32×32 pixels with 50 % overlap for the refined grid system.

3.6. Living cell embedded bio-ink printing.

The CNF ink containing 1×10^6 cells/ml fibroblast cells were printed into the CNF hydrogel matrix and cultured in the medium consisting of DMEM with 4.5 g/l glucose, L-glutamine, sodium pyruvate, and 10 % FBS. The cells were cultured in a humidified 5 % CO_2 incubator at 37 °C for 7 days. The viability of the cultured cells was investigated with a live and dead viability/cytotoxicity kit (Invitrogen, Waltham, MA, USA). The live and dead assay reagents were added to a Petri dish containing cell-cultured discs and incubated for 1 h at room temperature in the dark. The fluorescence images of the cells were collected using an inverted fluorescence microscope.

3.7. Silicone actuator printing.

The prepared silicone ink was printed inside a CNF hydrogel matrix to prepare a silicone structure. After printing, it was cured in an 80 ºC oven for 1 hour with the matrix system sealed. The printed silicone was then removed from the matrix, washed with distilled water, and a silicone tube was inserted at the end of the structure to fabricate the actuator. The shape of the actuator changed as the pneumatic or hydraulic pressure applied.

3.8. Fabrication of CNF based open-channel microfluidic devices.

3.8.1. Fabrication process of CNF microfluidic devices.

The 3D open channels were fabricated by removing the inks from the CNF matrix printed with the petroleum-jelly ink after drying. For the removal of the petroleum-jelly inks, the 3D structures embedded in the CNF matrix were heated to 70 °C in the oven for 5 min. The melted ink was removed by applying compressed air through the channels, and the inner surface of the channels was washed with n-hexane several times by flowing it through the channels at 70 °C. The conversion of the hydrophilic CNF channel surface to a hydrophobic state was achieved using 10 wt % trimethylchlorosilane in n-hexane with continuous flowing of the solution. After silanization, the inner channel surface was coated with silicone elastomer (SH 9555, Dow Corning, Midland, MI, USA). The silicone elastomer base was mixed with a curing agent at a 20:1 weight ratio, and the solution was diluted to 30 wt % with n-hexane. The dilute solution of silicone elastomer was spread on the inner channel surface and was cured for 10 min at 80 °C. A silicone elastomer solution containing 0.1 % fluorescent polystyrene microspheres (2 μm, yellow-green FluoSpheres, Invitrogen, Eugene, OR, USA) was used to visualize the specific layer of silicone elastomer cured at the inner channel surface. Lines of printed ink were imaged using fluorescence optical microscopy (Olympus BX51, Tokyo, Japan). The surface morphology and the cross-section of the 3D multichannel were imaged using field-emission scanning electron microscopy (FE-SEM, SUPRA 55VP, Carl Zeiss, Oberkochen, Germany) at an operation voltage of 2 kV. Platinum was sputtered onto the cross-sectional area of the microfluidic devices at 20 mA for 160 s as a conductive coating for imaging purposes. The surface topography of the inner channel surface was imaged using atomic force microscopy (AFM, XE100, Park Systems, Suwon, Korea) in a non-contact

mode (PPP-NCHR 10M, Nanosensors, Neuchâtel, Switzerland) at the scan rate of 0.6 Hz for surface areas of 2×2 μm^2.

3.8.2. CNF based pH sensor for flowing solution.

A CNF microfluidic device was printed with petroleum-jelly ink according to the CAD design with coiled detection zones. Before removing the inks, a universal pH indicator was dropped onto a coiled feature. After additional drying, the CNF film with printed structures was detached from the Petri dish, and the petroleum-jelly ink was removed by flowing n-hexane through the channels at 70 °C. The inner surface of the microchannels was not coated with silicone elastomer, and distilled water (DW), 1 M NaOH, and 1 M HCl were injected into the channel sequentially. The colorimetric changes in the detection zone were captured with a digital camera.

3.8.3. CNF based heavy metal sensor.

A CNF microfluidic device with three inlets, mixing zones, and detection zones were 3D-printed with petroleum-jelly ink according to the CAD design. The petroleum-jelly ink was removed from the channels, whose inner surface was coated with silicone elastomer, except for the detection zones. Then, 0.01 M dimethylglyoxime (Sigma-Aldrich) was dissolved in an ethanol/water (60/40) solution for the detection of nickel ions, and 0.01 M 1, 5-diphenylcarbazide (Sigma-Aldrich) was dissolved in acetone/water (60/40) solution for the detection of chromium ions. The dimethylglyoxime and 1, 5-diphenylcarbazide solutions were dropped onto the allocated detection zones and were dried completely at 70 °C for 1 h. Different concentrations of potassium dichromate (Sigma-Aldrich) and nickel nitrate hexahydrate (Sigma-Aldrich) in DW were prepared, and calibration curves were obtained with UV–visible (UV–vis) spectroscopy for analysis of the ion concentrations. The mixture of ion solutions was injected into the inlet to evaluate the

selectivity. The 10 % H_2SO_4 and 1 % NaOH solutions were eluted at the specific chelating condition of the metal ions, with dimethylglyoxime and 1, 5-diphenylcarbazide at the detection zones. The flow rates of the heavy metal ion, H_2SO_4, and NaOH solutions were 50, 2, and 2 μl/min, respectively.

3.9. Fabrication of CNF based open cell culture platform.

Petroleum-jelly-printed CNF hydrogels were dehydrated to form a film structure with microfluidic designs. After dehydration for 24 h, the petroleum jelly patterns were removed by applying compressed air at 70 °C to form a channel structure. The channels formed in the CNF film were treated with a 1 % calcium ion solution to prevent further deformation. The produced CNF-based culture platform was washed twice with PBS and stored at room temperature until use.

3.9.1. Hydrophobic treatment of CNF.

Methyltrimethoxysilane (MTMS, Sigma-Aldrich) treatment was carried out to prepare hydrophobized CNF (Hphob-CNF). MTMS was added to the 1.0% CNF hydrogel and mixed well with an overhead stirrer (DAIHAN Scientific Corporation, HT-50DX, Korea) to achieve MTMS concentrations of 0.2, 0.5, and 1.0 %. The reaction was then allowed to proceed for 1 h in an 80 °C oven. The chemical structure of the CNF was characterized by Fourier transform infrared spectroscopy (FT-IR spectroscopy, Nicolet iS5, Thermo Scientific, USA) in the range of 4000–500 cm^{-1}, and 32 scans with a resolution of 4 cm^{-1}. The degree of hydrophobicity was compared by the swelling properties of dried Hphob-CNF prepared at the different concentrations of MTMS. The Hphob-CNF films (1 cm × 1 cm) were immersed in phosphate-buffered saline (PBS) for 24 h, and their weight was measured after removal of water at the surface with tissue paper.

3.9.2. Mass transfer test at the CNF layers.

A static imaging technique was used to characterize the diffusion of small-molecular weight species through the CNF hydrogels. Fluorescein isothiocyanate-dextran (FITC-Dextran, Sigma-Aldrich) was selected as a model drug to evaluate the diffusion of biomolecules into CNF hydrogels from the channels. Diffusion of FITC-Dex to the Hphob-CNF and Hphil-CNF layers was observed with a fluorescence microscope (iRis™; Logos Biosystems, Korea). Three different molecular weights (4, 70, and 150 kDa) of FITC-Dex were dissolved in DW at 5 mg/ml of solution concentration, and each solution was injected into the channel at a rate of 1 ml/h. The fluorescence images were captured at the interval of 5 min for 1 h and analyzed with ImageJ (NIH, Bethesda, Maryland, USA).

3.9.3. Cell culture on CNF microfluidic devices.

Hphob-CNF and Hphil-CNF films were prepared as described above and cut into 8-mm-diameter discs. Then, 1×10^6 cells/ml of fibroblasts were seeded on the Hphob-CNF and Hphil-CNF discs and cultured in DMEM with 4.5 g/l glucose, L-glutamine, sodium pyruvate, and 10 % FBS. The cells seeded on the CNF discs were cultured in a humidified, 5 % CO_2 incubator at 37 °C for 1, 4, and 7 days. The viability of the cultured cells was investigated with a live and dead viability/cytotoxicity kit (Invitrogen, Waltham, MA, USA). The live and dead assay reagents were added to a Petri dish containing cell culture discs and incubated for 1 h at room temperature in the dark. Images of the fluorescence of the cells were collected using an inverted fluorescence microscope.

For investigation of cell proliferation, the cell-cultured CNF discs were washed with PBS and incubated with Alamar Blue (Invitrogen) solution for 4 h at 37 °C. The Alamar Blue fluorescence was assayed at 540 nm (excitation) and 590 nm (emission) using a microplate reader (Synergy HT, BioTek).

A549 cells were seeded from solution (1×10^6 cells/ml) on the CNF open culture platform and incubated in a medium consisting of DMEM with 4.5 g/l glucose, L-glutamine, sodium pyruvate, and 10 % FBS in a humidified, 5 % CO_2 incubator at 37 °C. The IC_{50} of cisplatin (Sigma-Aldrich) of the cells was measured at a controlled infusion rate and drug concentration. The concentration of drugs at the inlet was fixed at 500 μM and flowed at a rate of 0.5 ml/h. PBS was flowed through the opposite inlet at a rate of 2 ml/h or 4 ml/h to adjust the concentration of cisplatin solution in the outlets to 10, 1, 0.1, and 0.01 μM. The cisplatin solution was flowed for 24 h, and cells were retrieved from the discs cut from the culture platform using a punch whose inner diameter was 0.64 cm. Then, the viability test of A549 cells was performed with a live and dead viability/cytotoxicity kit, and the cell proliferation was estimated with Alamar Blue assay as described above. The IC_{50} of cisplatin was fitted using GraphPad Prism software (GraphPad Software Inc., San Diego, CA) based on the obtained proliferation results.

3.10. Imaging.

The surface morphology of the CNF films was imaged using field-emission scanning electron microscopy (FE-SEM, SUPRA 55VP, Carl Zeiss, Oberkochen, Germany) at an operation voltage of 2 kV. Platinum was sputtered onto the CNF films at 20 mA for 160 s as a conductive coating for imaging purposes.

IV. Results and Discussion

4.1. Properties of carboxymethylated CNF.

Carboxymethylation pretreatment was performed to evaluate the effect of the matrix on printing fidelity by controlling the dimension of CNF. Carboxymethylation is a reaction that replaces hydroxyl groups exposed on CNF fiber surface with carboxymethyl groups, which has the advantage of simple reaction and efficient nanofibrillization. Figure 7a shows the conductivity titration curve of carboxymethylated pulp. As NaOH is added, the ionic conductivity decreases. The phase of rapid decrease in conductivity is due to the neutralization of initial HCl. The flat phase is formed by the carboxyl groups in carboxymethylated CNF [178]. Therefore, carboxyl groups could be quantified by the amount of NaOH consumed in the flat section. As the reaction time increased, the amount of NaOH consumed by the carboxyl group gradually increased. The carboxylic content of pristine pulp was nearly 0.01 mmol/g, but the carboxylic content was increased as the reaction time increased (Figure 7b, c). As the reaction time increased to 30 minutes, the carboxylic content increased to 0.66 mmol/g, 0.95 mmol/g for 60 minutes, and 1.14 mmol/g for 90 minutes. And the degree of substitution (DS) was 0.002 at 0 minutes, 0.107 at 30 minutes, 0.154 at 60 minutes, and 0.185 at 90 minutes.

Carboxymethylated pulp was ground mechanically, and the surface charge was measured. Non-carboxymethylated CNF showed a zeta potential of -30 mV due to the NaOH treatments in the kraft process. A number of hydroxyl groups at the CNF surface are replaced by O^-Na^+ groups [179-181]. The zeta potential gradually decreased to -80 mV as the reaction time increased to 90 minutes (Figure 8). These results showed that the carboxymethylation pretreatment increased the amount of negative charge at the surface of CNF [182].
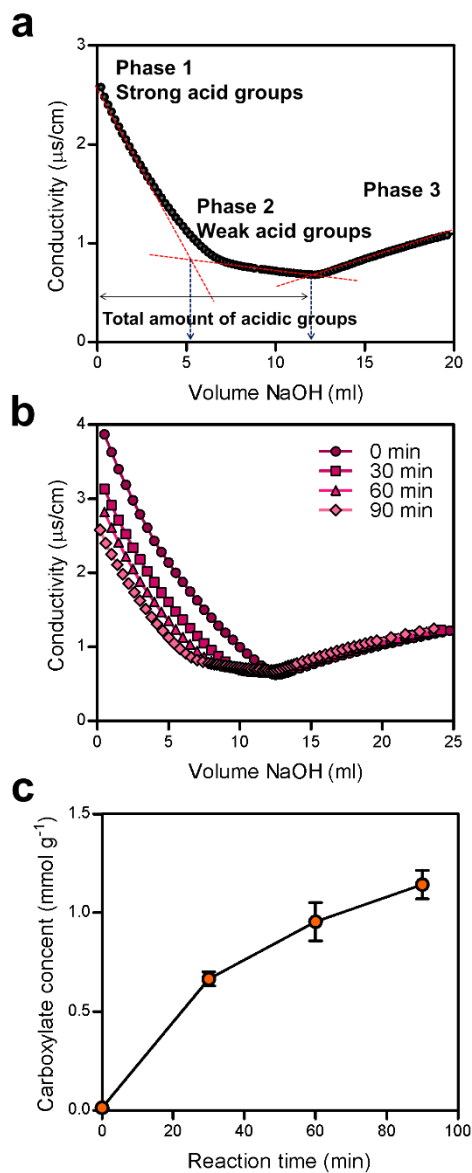
Figure 7. Measurement of the carboxylic content. (a) Schematic diagram of NaOH consumption in the conductivity titration curve. (b) Conductivity titration curve of pristine pulp cellulose, and the pulp celluloses with carboxymethylated for 30, 60 and 90min. (c) Carboxylic contents of pulp celluloses according to the reaction time.
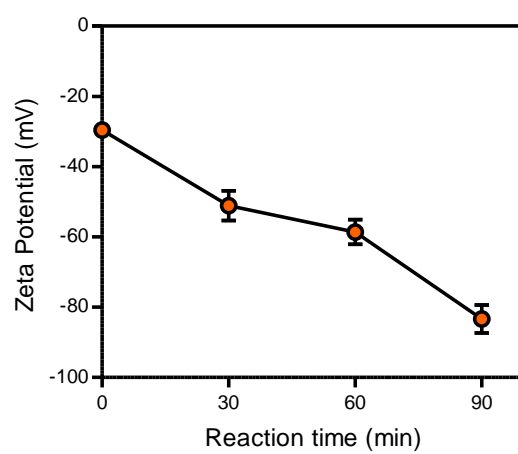
Figure 8. Zeta potential of carboxymethylated CNF according to the reaction time.

The morphology of the nanofibers was observed using FE-SEM with a CNF film at a different carboxylic content (Figure 9). The surface of the non-carboxymethylated CNF film reflected a large number of thick fibers (Figure 9a). The fibers were not nanofibrillated effectively, and a large bundle of fibers was observed. On the other hand, the CNF with carboxylic content of 0.66 mmol/g showed a relatively smooth surface, and the fibers were nanofibrillated more than non-carboxymethylated CNFs (Figure 9b). However, the fiber dimension was not uniform, and the fiber bundles still had a large dimension. As the carboxylic content increased to 1.14 mmol/g, the fiber bundles gradually disappeared, and only the CNF with tiny dimensions remained (Figure 9d). The carboxylic content and the degree of nanofibrillation were closely related. As the amount of carboxyl groups increased, the degree of nanofibrillation was increased due to the inter-fiber repulsion [12, 183].

Carboxymethylation was an energy-efficient pretreatment process for the nanofibrillation [102, 184]. The CNF was highly nanofibrillated, and the fiber width of CNF with the carboxylic content of 1.14 mmol/g was about 18.6 nm, as measured with atomic force microscopy (Figure 10a, b).
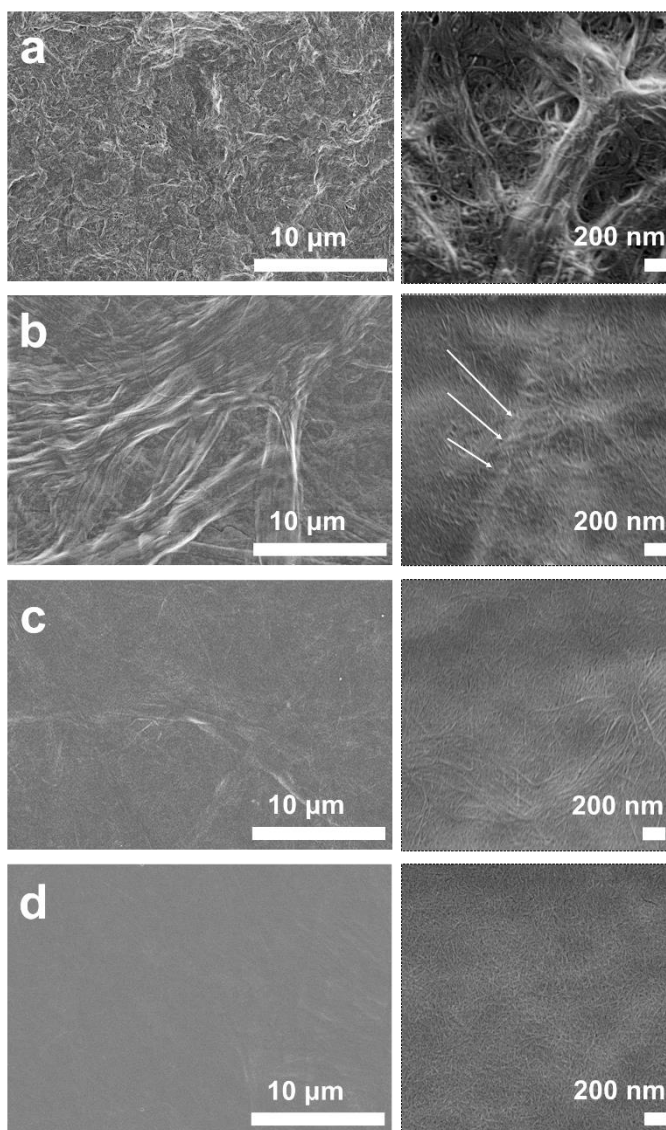
Figure 9. Morphological properties of CNF films. (a) SEM images of non-carboxymethylated CNF, and the CNFs with carboxylic contents of (b) 0.66 mmol/g, (c) 0.95 mmol/g, (d) 1.14 mmol/g. The part indicated by the arrow is a fiber bundle in which nanofibrillization did not sufficiently occur.
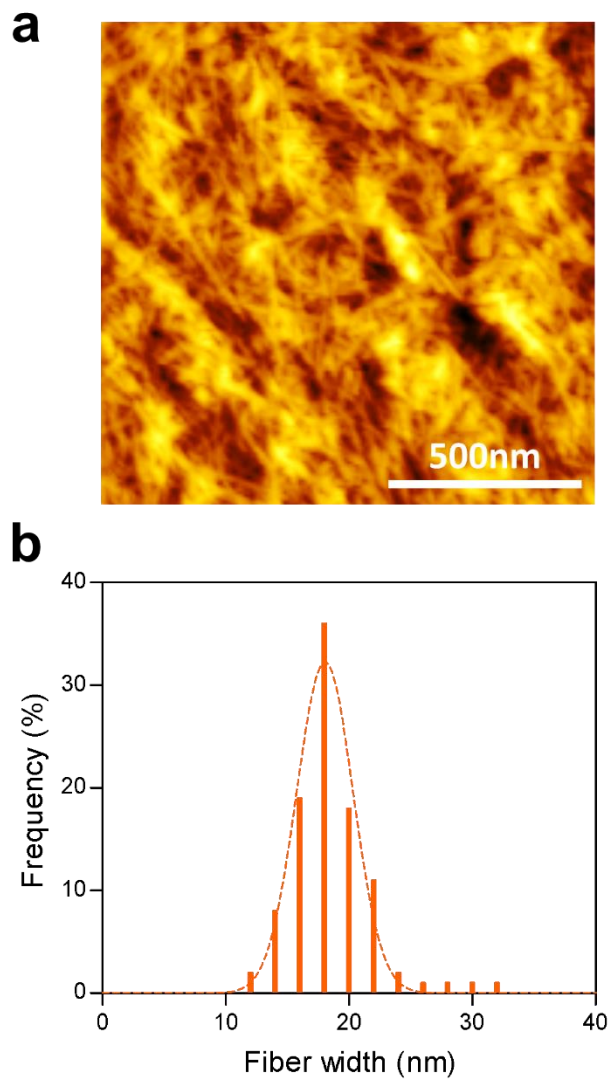
Figure 10. (a) AFM image of CNF film with carboxylic content of 1.14 mmol/g. (b) The fiber width distribution of CNF with carboxylic content of 1.14 mmol/g measured by AFM.

Figure 11 shows the FT-IR spectra of the CNF films according to the carboxylic content. The CNF films showed peaks at 3341 cm^{-1} (-OH stretching), 2940 cm^{-1} (alkyl -CH stretching). The magnified area clearly showed the difference between non-carboxymethylated CNF and carboxymethylated CNF. The non-carboxymethylated CNF had a peak at 1660 cm^{-1}, which was represented by water absorbed in the fiber [185]. As the carboxymethylation progressed, the carboxyl peak assigned at 1603 cm^{-1} gradually increased.

Optical transparency of the 3D printing matrix is required to observe the ink features printed inside. The transparency of CNF hydrogel was varied with the carboxylic content (Figure 12a). As the carboxylic content increased, the transparency of CNF hydrogel increased at the range of visible light. A non-carboxymethylated CNF hydrogel hardly transmitted light at a wavelength of 550 nm, but the CNF hydrogel with the carboxylic content of 1.14 mmol/g showed transparency of about 70%. The transparency of the carboxymethylated CNF hydrogels was confirmed by showing letters at the background enough to be read (Figure 12b)
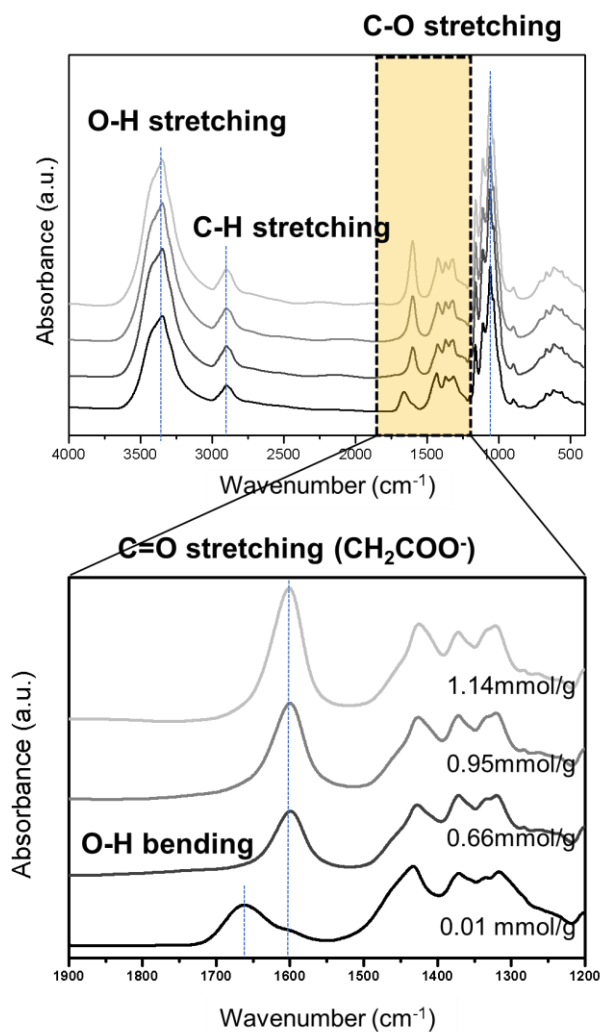
Figure 11. FTIR spectra of CNF films according to carboxylic contents. The peak of carboxyl group is shown in detail from 1200 cm^{-1} to 1900 cm^{-1}.
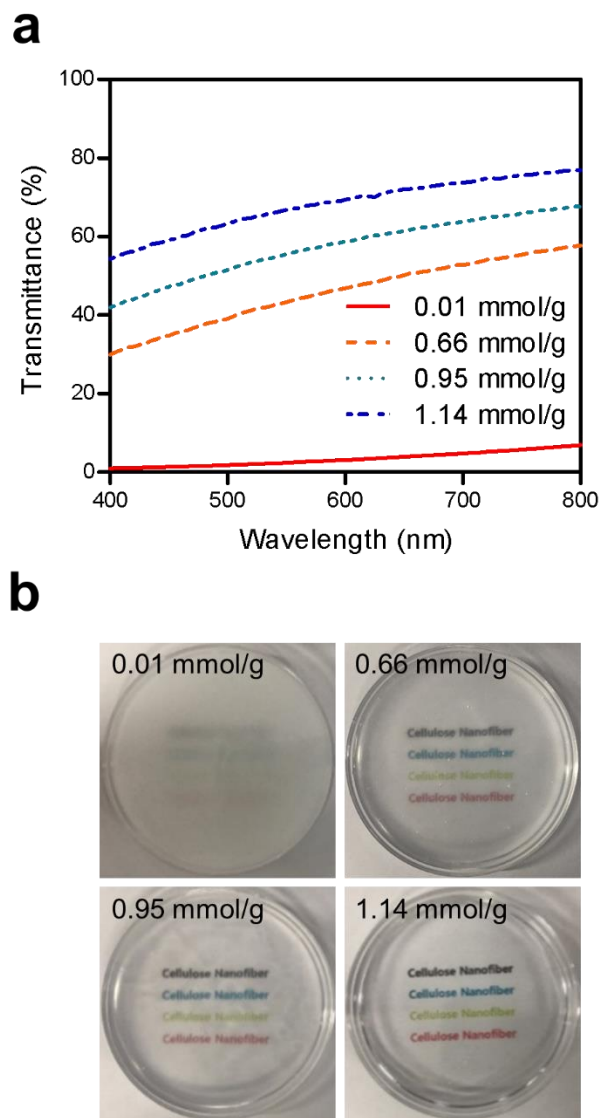
Figure 12. Transparency of CNF hydrogels. (a) Transmittance of CNF hydrogels according to the carboxylic contents at a wavelength from 400 to 800 nm. (b) Photographs of CNF hydrogels according to the carboxylic content at the CNF concentration of 0.75%.

4.2. Rheological properties of CNF matrix.

4.2.1. Shear-thinning property of CNF matrix.

The matrix, a CNF hydrogel, played a role in keeping the printed structures in bulk in a free-standing form. Rheological optimization of the matrix was required to prevent the printed structures from changing their shapes. The surface tension and pressure-driven buckling of the ink material caused serious structural changes to the printed paths [84]. Since the rheological behavior of the CNF hydrogels was a critical factor, four different carboxylic contents and six different concentrations of CNF hydrogels were chosen, and their rheological properties were measured.

To observe the shear-thinning behavior and obtain the Herschel-Bulkley parameters for each matrix material, continuous shear stress was measured with the shear rate increases. Figure 13a shows the fitting result of a CNF matrix with a carboxylic content of 1.14 mmol/g to the Huschel Berkley model, given by $\sigma = \sigma_y + k\varepsilon^n$, where σ is the measured stress, σ_y is the yield stress, and ε is the applied shear rate. The CNF matrix showed typical shear thinning behavior that the n value appears to 0.4. These shear thinning behavior allowed CNF as a matrix material for MAP. Besides, in order to be used as a matrix, an appropriate yielding property is needed because the matrix must be deformed while the nozzle passes. The yield stress corresponds to the shear stress at zero shear rate. The yield stress could be determined by fitting to the Herschel-Bulkley model.

The change of shear stress was measured according to the carboxylic content at fixed CNF concentration (Figure 13b). As the carboxylic content increased, the yield stress and the viscosity increased. This can be interpreted that the entanglement between nanofibers could be effectively increased in the small dimensional nanofibers with high carboxylic content. However, the n value was still less than 1 in all CNF matrices maintaining their shear thinning behavior.

Although having strong electrostatic forces, CNF interacts similarly to macroscopic fibers in suspension [183]. Thus, one can first consider the fiber−fiber interaction from a mechanistic perspective. The inter-fiber interaction is described as an entanglement, which is the most important factor in determining the rheological properties of the CNF suspension. Based on the mechanistic model, the fiber entanglement is controlled by the number of contact points, the bending stiffness of the fibers, and the friction between the fibers. In this respect, the change in the fiber dimension acts as a decisive factor in changing the contact point, so that the viscosity can be improved.

Similarly, the shear stress increased as the CNF matrix concentration increased from 0.25% to 1.5% (Figure 13c). The change of the concentration means the change of the distance between the fibers. It directly affected the entanglement probability between fibers so that the yield stress and viscosity increased sharply as the concentration increases.
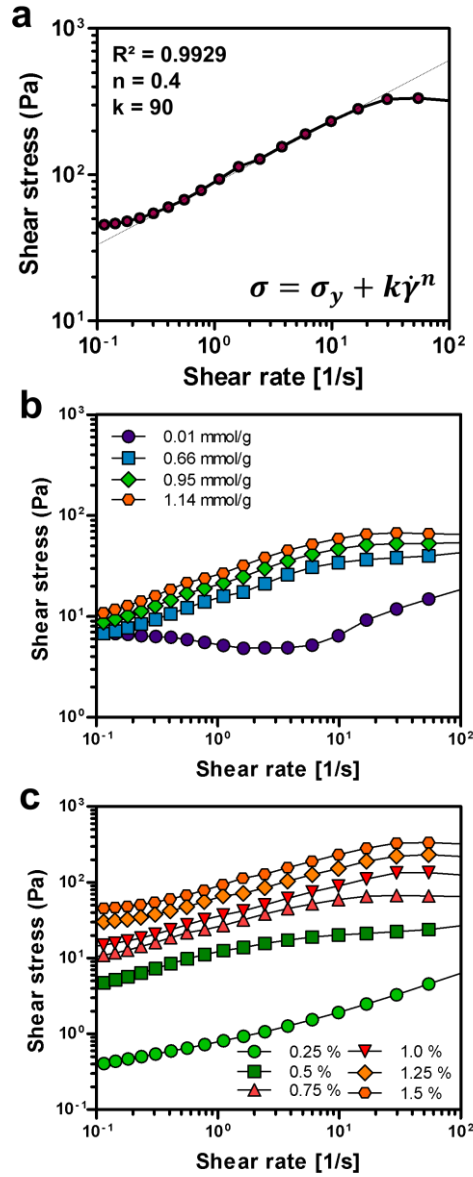
Figure 13. Shear stress of the CNF matrix as a function of shear rate. (a) Fitted shear stress-shear rate curve of the CNF matrix with the Herschel-Bulkley model at the carboxylic content of 1.14 mmol/g and concentration of 1.5 %. The shear stress-shear rate curves of the CNF matrix according to (b) the carboxylic content at the CNF concentration of 0.75 % and (b) the concentration at the carboxylic content of 1.14 mmol/g.

4.2.2. Yielding property of CNF matrix.

It is important to characterize the yield stress of the CNF matrix since the elastic modulus dramatically changes as the shear stress increased. Oscillatory shear rheometry tests were performed to determine the yield stress of the CNF matrix at a frequency of 1 Hz. First, the elastic and viscous moduli of the CNF matrix were measured according to the carboxylic content at a fixed CNF concentration of 0.75% (Figure 14a). The elastic modulus and the range of solid-dominated shear stress increased as the carboxylic content increased. The yield stress was set as the shear stress value at which there was a decrease in elastic modulus [96]. There was a gradual decrease in elastic and viscous moduli close to the yield stress, indicating that yielding is not a sharp transition for these materials. Besides, the yield stress increased with the increase of the carboxyl content. This result indicates that the CNF matrix with high carboxylic content needs more shear stress to deform.

The concentration of CNFs was another critical factor in the change of yielding property of CNF hydrogels. As the concentration of CNF increased from 0.25 to 1.5%, the elastic modulus gradually increased (Figure 14b). The CNF concentration as low as 0.25% was liquid-dominated, whereas the CNF concentration of 1.5% showed solid-dominated characteristics.

The yield stresses were summarized at various CNF conditions in Figure 15. Figure 15a shows the yield stress obtained through the shear strain-shear stress curve, and figure 15b shows the yield stress obtained through the shear elastic modulus. In both cases, yield stress increased with increasing CNF concentration and carboxylic content. The difference in yield stress was significant with concentration as well as the carboxylic content. It was considered that the finer the fiber dimension, the greater the entanglement between fibers.
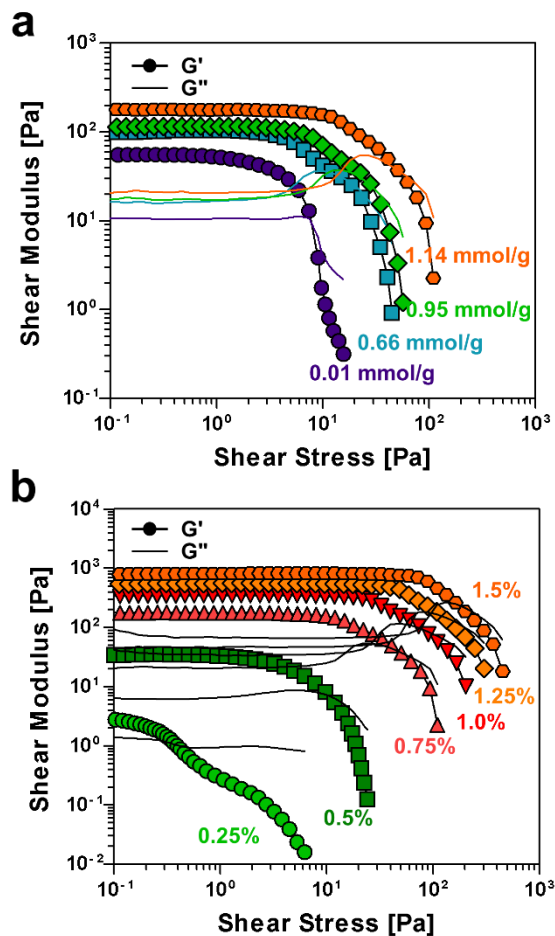
Figure 14. Elastic and viscous moduli of the CNF matrices according to (a) the carboxylic contents at the CNF concentration of 0.75 % and (b) the concentrations at the carboxylic content of 1.14 mmol/g. The yield stress is defined as the shear stress at the point away from the linear viscoelastic region.
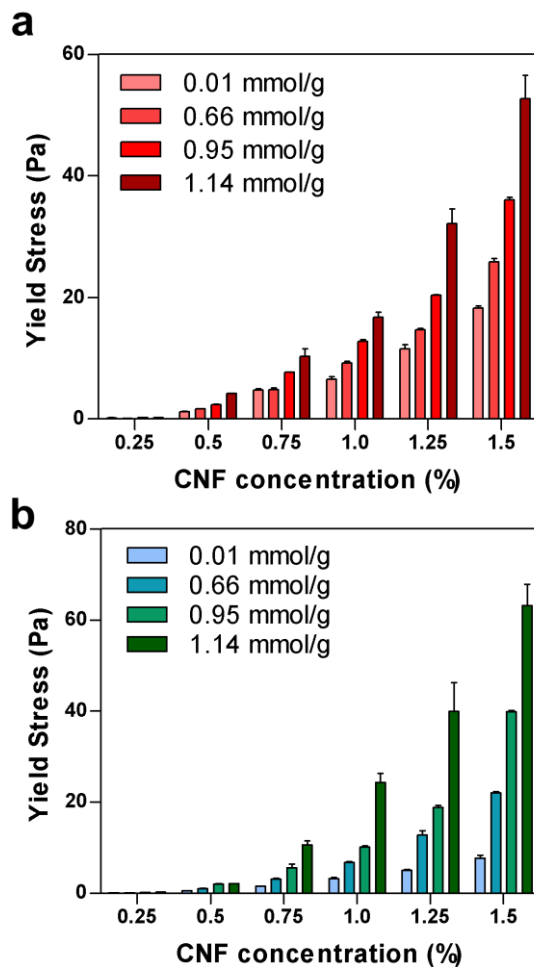
Figure 15. (a) The yield stresses of CNF matrix measured by the shear stress-shear rate curve according to carboxylic content and concentration. (b) The yield stresses of CNF matrix measured by the shear elastic modulus according to carboxylic content and concentration.

4.2.3. Creep and recovery properties of CNF matrix.

The shear modulus and viscosity of CNF vary depending on the shear stress and time, as well as the carboxylic content and concentration previously discussed. Due to the shear acting, the orientation of the nanofibers occurs, and the entanglement of the fibers is unwound [186]. When the shear is stopped, the fiber entanglement occurs again. This phenomenon was confirmed by observing the creep and recovery characteristics of CNF (Figure 16). Rheological measurements of thixotropic time demonstrated the recovery of elasticity [84]. Here, the shear rate was plotted for a constant applied stress. The time until the shear rate constant was considered to be the time when the fiber entanglement completely took place, and CNF showed that it took about 7 min until all the entanglement occurred. During this time, when the shear stress below the initial yielding threshold was applied, the fiber entanglement continued to occur after CNF orientation, and the shear modulus and viscosity changed continuously. In this way, the time range could be set to a constant value of G' and viscosity of the CNF matrix.
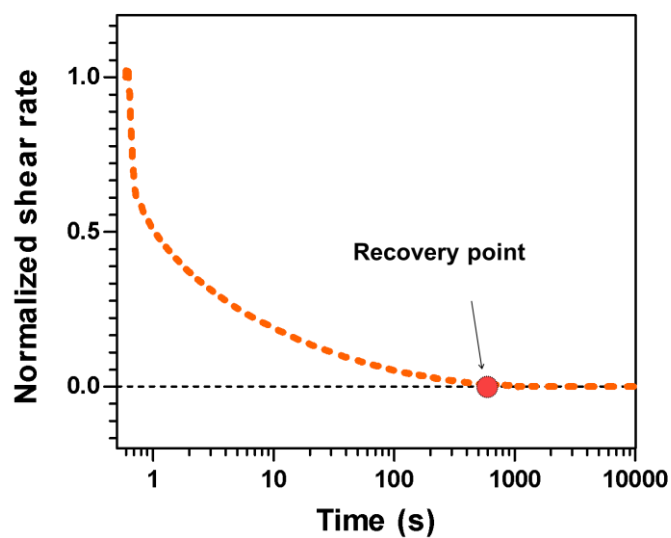
Figure 16. Creep and recovery characteristics of CNF with the carboxylic content of 1.14 mmol/g and the concentration of 0.75 %. The shear rate is plotted for a constant applied stress, immediately after reducing the stress below the yielding threshold.

4.3. Evaluation of printing fidelity in a single printing line feature.

4.3.1. Evaluation of printing fidelity by sharpness of angled-line.

The printing fidelity of the matrix-assisted 3D printing technique was determined by analyzing the features produced by direct injection of cross-linked acrylic acid-based model ink into the CNF matrix. The accuracy of printing was evaluated by the completeness of the single line comparing with the designed structures. Specifically, three criteria, including sharpness, cross-sectional ratio, and straightness of a printed line were evaluated for the determination of printing fidelity in the CNF matrix.

First, printing sharpness, printing path was set to form an angle of 90° and the difference between the ideal angle (θ_i=90°), and the measured angle of printed ink feature (θ_m) was analyzed. The angled-lines at each CNF matrix condition were observed with optical and fluorescence microscope (Figure 17). Based on the microscopic images, the difference of angle (θ_d) was obtained by the equation as $\theta_d = |\theta_i - \theta_m|$ for each CNF matrix condition (Figure 18a).

Printing in a non-carboxymethylated CNF matrix showed a random shape of the ink features, showing a large deviation between angles. However, the inks printed in the CNF matrix with carboxylic content of 0.66 mmol/g showed an acute angle at the low concentration and obtuse angle at the high concentration of the CNF matrix. Precise printing was available with 1.25% of CNF matrix with carboxylic content of 0.66 mmol/g, 1.0% of CNF matrix with carboxylic content of 0.95 mmol/g, and 0.75% of CNF matrix with carboxylic content of 1.14 mmol/g (Figure 18b).

The acute angle appeared when the CNF concentration or carboxylic content was low (Figure 18c). The matrix did not have an elastic modulus sufficient to support the ink to be ejected, and it turned to a liquid-dominated state due to the shear stress generated by the nozzle and the ejected ink. When the elastic modulus was sufficient to support the ejected ink, an accurate angle

appeared, and the CNF matrix had a solid-dominated phase (Figure 18d). However, when the elastic modulus of the CNF matrix became higher than necessary, it showed an obtuse ink feature (Figure 18e). The effect of the carboxylic content can compensate for the effect of the concentration of CNF. The lower the degree of carboxymethylation, the more stable the printing could be achieved at the higher CNF concentrations (Figure 18f).

Figure 19a sequentially shows the path of the nozzle when printing an angled line. It is important to note that an overlapped area of ink at the angled edge. In this process, the ejected ink was forced in outer directions of angle, with the angle determined depending on the yield stress of the CNF matrix (Figure 19b). If the CNF matrix had low carboxylic content or low concentration, the CNF matrix showed low yield stress that deformed even at the small external stress. Thus, the matrix could not withstand the force that the ink pushes outward, resulting in the acute angle. However, if the yield stress of the CNF matrix reaches a value that can withstand the force enough, it can be printed accurately at the desired angle. If the yield stress value of the matrix is too high, the obtuse angle is shown by the overlapped ink. As a result, the yield stress of the accurately printed CNF matrix was similar to the yield stress of the model ink (Figure 19c).

Figure. 20 shows the change of angle according to the injection pressure and printing speed. As the injection pressure was increased from 20 psi to 50 psi, the printed angle gradually increased. This was because the size of the overlapping area also increased with increasing injected amount of ink. The injection rate was fixed by adjusting the printing speed so as not to change the volume of overlapping area. As a result, when the injection volume was constant, the angle was constant regardless of injection pressure and printing speed. The printing shape could be predicted by measuring the yield stress of the ink and the matrix under the fixed injection pressure and printing.
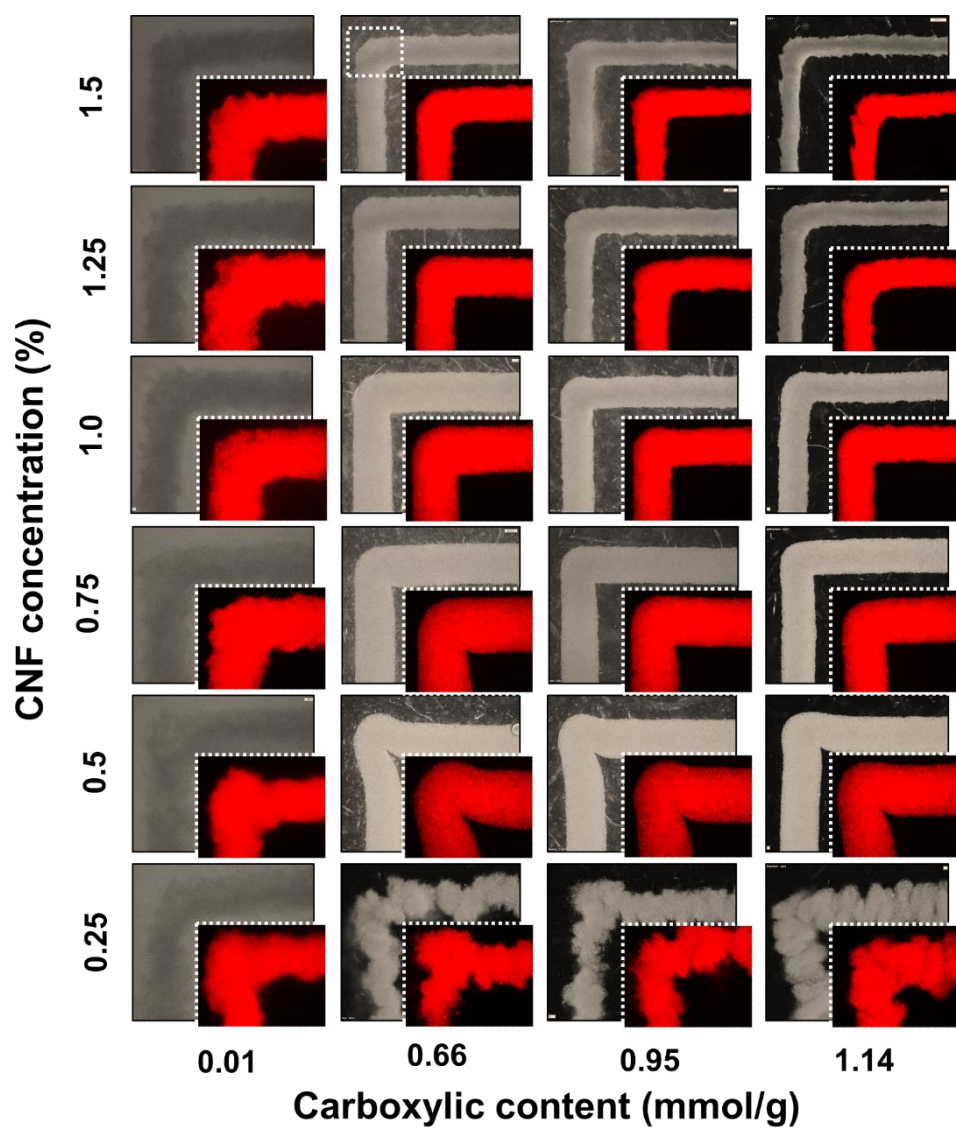
Figure 17. Optical and fluorescence microscopic images of printed cross-linked polyacrylic acid based model inks at various CNF matrix conditions according to carboxylic content and concentration.
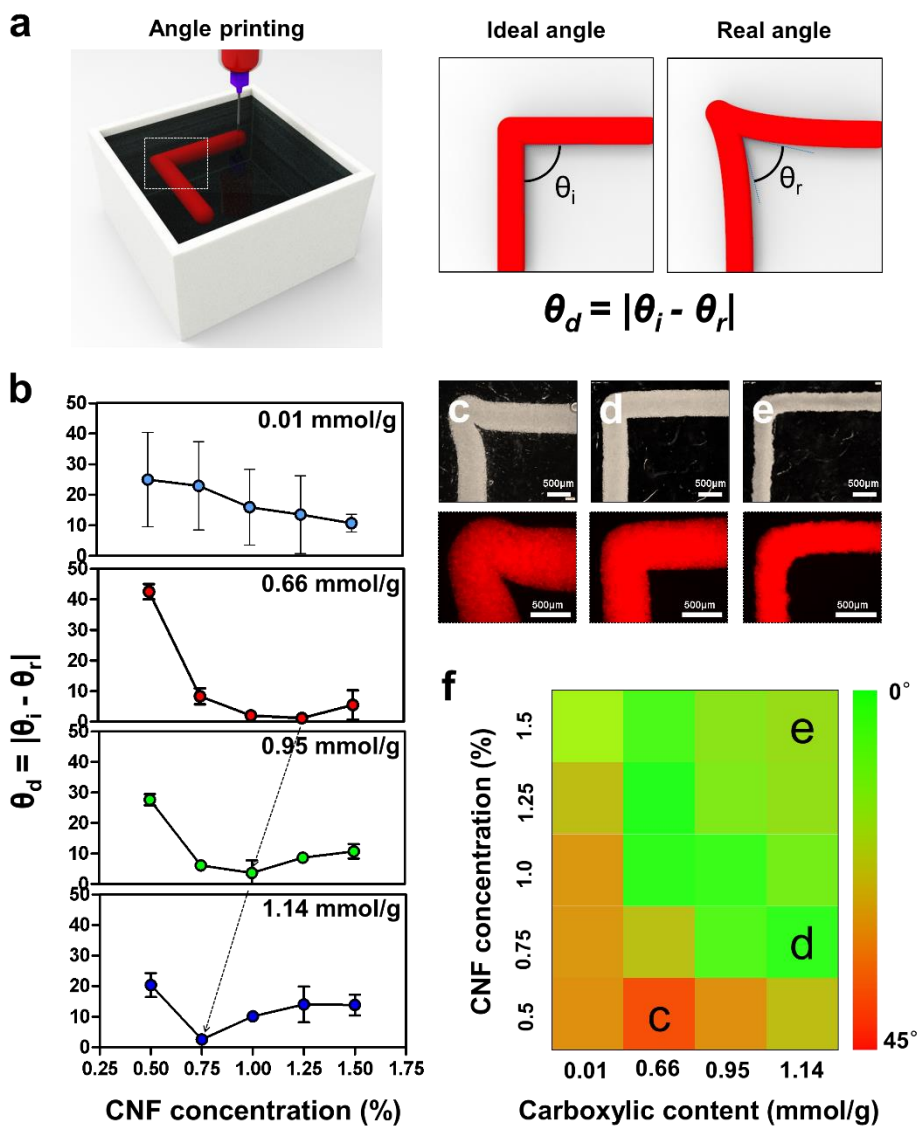
Figure 18. Evaluation of printing fidelity of CNF matrix by sharpness of angled-line. (a) Schematic illustration for measurement of the difference (θ_d) between the ideal angle (θ_i) and the actual printed angle (θ_r). (b) Changes of θ_d at different CNF matrix conditions according to the carboxylic content and concentration. Optical and fluorescent microscopic images of the actual printed angle at CNF matrix condition of (c) 0.66 mmol/g with 0.5%, (d) 1.14 mmol/g with 0.75%, and (e) 1.14 mmol/g with 1.5%. (f) Color map of printing fidelity according to the difference of angle (θ_d) from 0° to 45°.
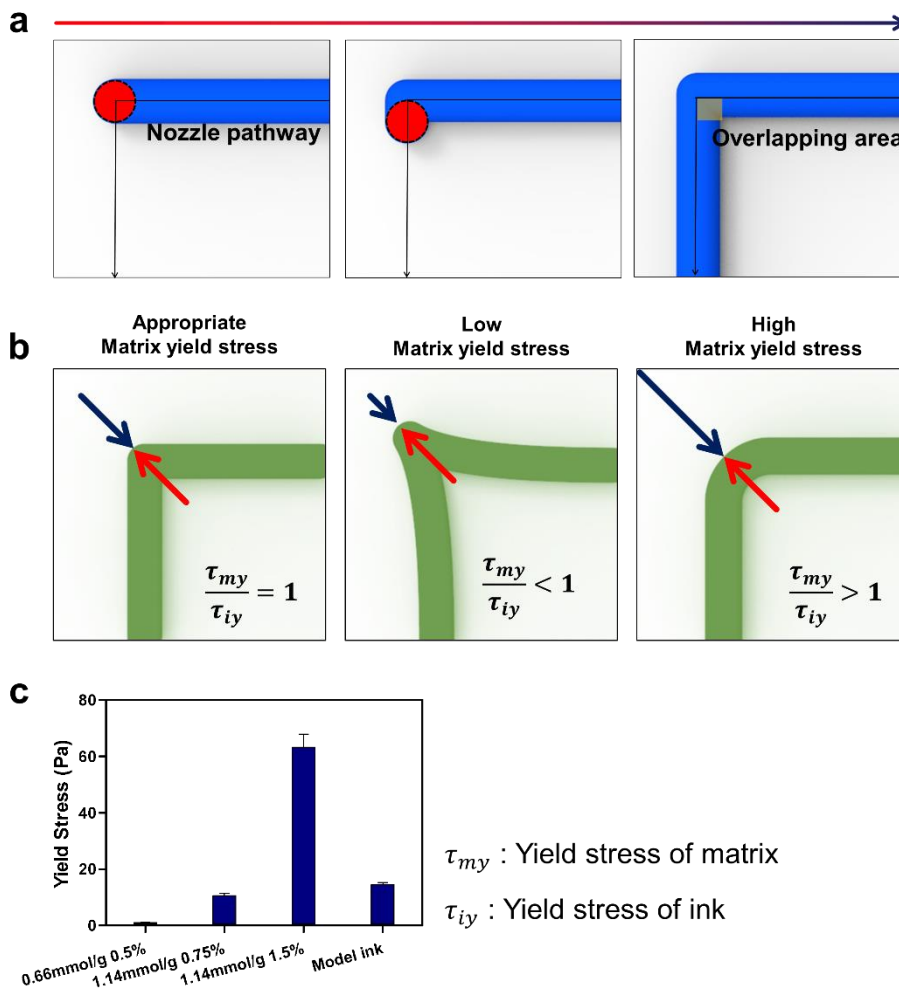
Figure 19. Analysis of sharpness according to the yield stress of the CNF matrix. (a) Printed shapes at the edged area when printing the angled line. (b) The variation of the printed angle according to the yield stress of the matrix and the yield stress of the ink. (c) Yield stresses of the CNF matrix and the cross-linked polyacrylic acid model ink.
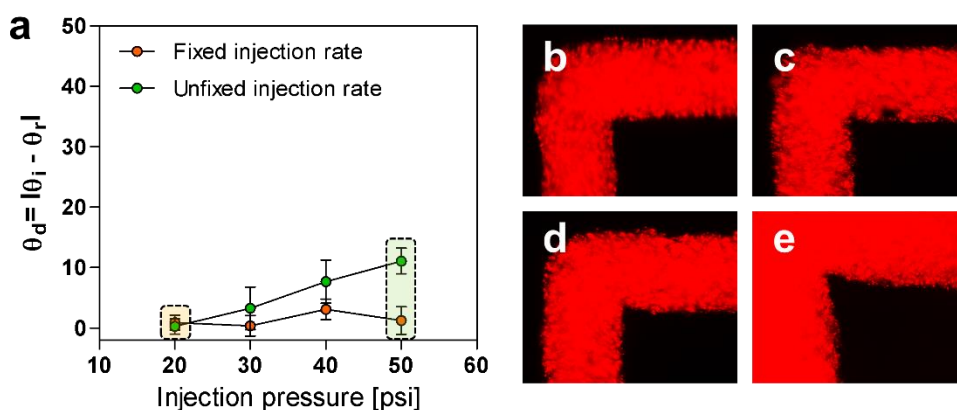
Figure 20. Analysis of sharpness according to the injection pressure and printing speed at the CNF matrix concentration of 0.75% and carboxylic content of 1.14 mmol/g. (a) Changes of θ_d according to the different injection pressure depending on whether the injection pressure was fixed. Fluorescent microscopic images of the actual printed angle at the injection pressure of 20 psi with printing speed of 2 mm/s (b), the injection pressure of 50 psi with printing speed of 11.3 mm/s (c), the injection pressure of 20 psi with printing speed of 2 mm/s (d), and the injection pressure of 50 psi with printing speed of 2 mm/s (e).

4.3.2. Evaluation of printing fidelity by cross-sectional ratio.

The cross-sectional ratio of the ink ejected under each CNF matrix condition was evaluated during the printing of a straight line (Figure 21a). The high printing fidelity is reflected by the cross-section of the exact circle shape, and the ratio between the lengths in the horizontal and vertical directions is close to 1. The non-carboxymethylated CNF matrix showed a very high cross-sectional ratio, but the cross-sectional ratio showed a close value to 1 at a low concentration of carboxymethylated CNF (Figure 21b). As the CNF concentration increased, the cross-section of the printed ink was changed to an elliptical shape (Figure 21c, d). The color map shows that the lower the concentration of the CNF matrix, the closer the cross-sectional ratio is to 1. In addition, as the carboxylic content increased, the increasing rate in the cross-sectional ratio increased (Figure 21e).

It resulted from the formation of crevices along the nozzle pass through the matrix with a higher concentration of CNF (Figure 22a). Structures can be printed into CNF hydrogel matrix of varying composition without the addition of filler fluids because potential crevasses will spontaneously collapse when the hydrostatic stress at the bottom of the crevasses ($\rho g h$, where ρ is density, g is gravity, and h is depth) exceeds the gels yield stress (σ_y) (Figure 22b). If the yield stress is too high and crevasse cannot recover quickly, the ejected ink fills the empty upper space and forms an elliptical shape. For this reason, the cross-sectional ratio increased more rapidly as the CNF concentration increased in the CNF matrix with high carboxylic content. Given the cross-sectional ratio, the CNF matrix with too high yield stress should be avoided.
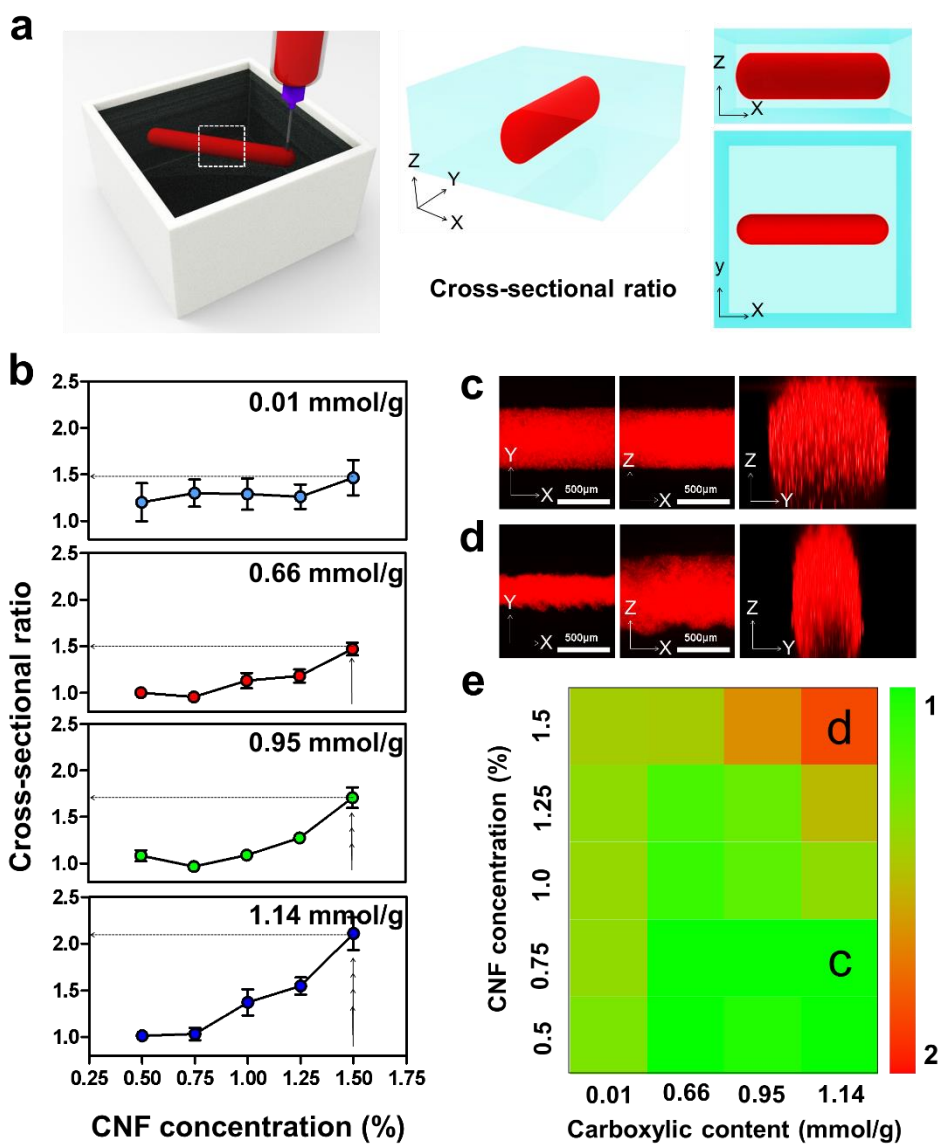
Figure 21. Evaluation of printing fidelity by cross-sectional ratio. (a) Schematic illustration of the cross-sectional ratio analysis. (b) Changes in cross-sectional ratio at different CNF matrix conditions according to the carboxylic content and concentration. Optical and fluorescent microscopic images of the cross-section shapes of the printed lines at CNF matrix conditions of (c) 1.14 mmol/g with 0.75%, and (d) 1.14 mmol/g with 1.5%. (e) Color map of printing fidelity according to the cross-sectional ratio value from 1 to 2.
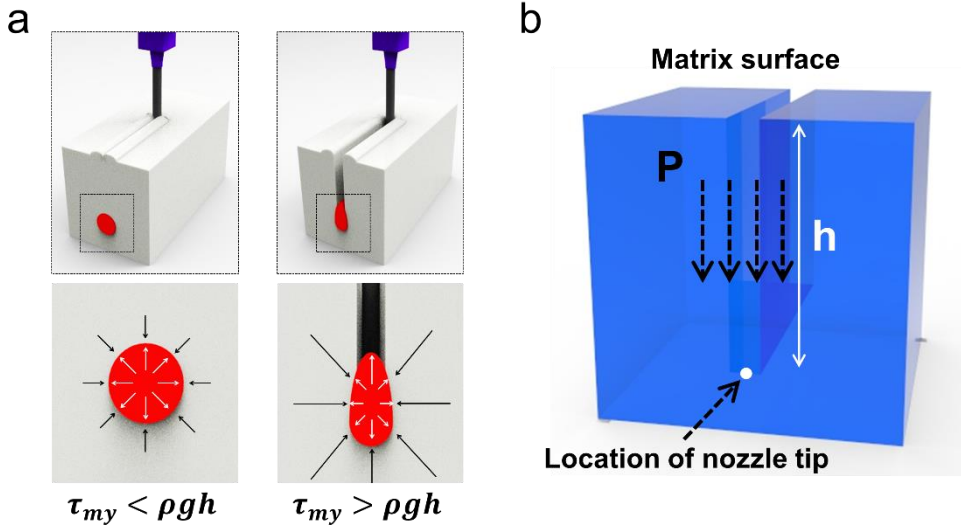
Figure 22. Schematic illustration of the crevasses formation condition according to the matrix yield stress. (a) Shape changes of printed ink cross-section due to the relationship between the CNF matrix yield stress and the hydrostatic pressure. (b) Hydrostatic pressure at the position where the nozzle passes through the CNF matrix.

4.3.3. Evaluation of printing fidelity by straightness of line surface.

The third evaluation factor is the straightness of the printed feature. The shape of the printed ink features was imaged with a fluorescence microscope and was compared to analyze the deviation of the printed ink feature from the straight line (Figure 23). The straightness of the printed line was evaluated by R_a (surface roughness) according to the carboxylic content and concentration of the CNF matrix (Figure 24a). The non-carboxymethylated CNF matrix showed about 20 μm of R_a and remained constant regardless of concentration (Figure 24b). However, printing on carboxymethylated CNF decreased R_a. Besides, R_a increased with increasing CNF matrix concentration (Figure 24c-24e). High printing fidelity in terms of straightness means that the surface of the printed ink is smooth (Figure 24f).

The high surface roughness in non-carboxymethylated CNF matrices is due to the large fiber dimensions, which leads to a large space between the fibers. The ejected ink could bleed into the relatively weak areas between the fibers. Since the entanglements of fibers were unevenly formed, relatively dense and loose portions coexisted with large deviation. In contrast, the fiber dimension became smaller in the carboxymethylated CNF matrix, and a relatively uniform matrix was formed.
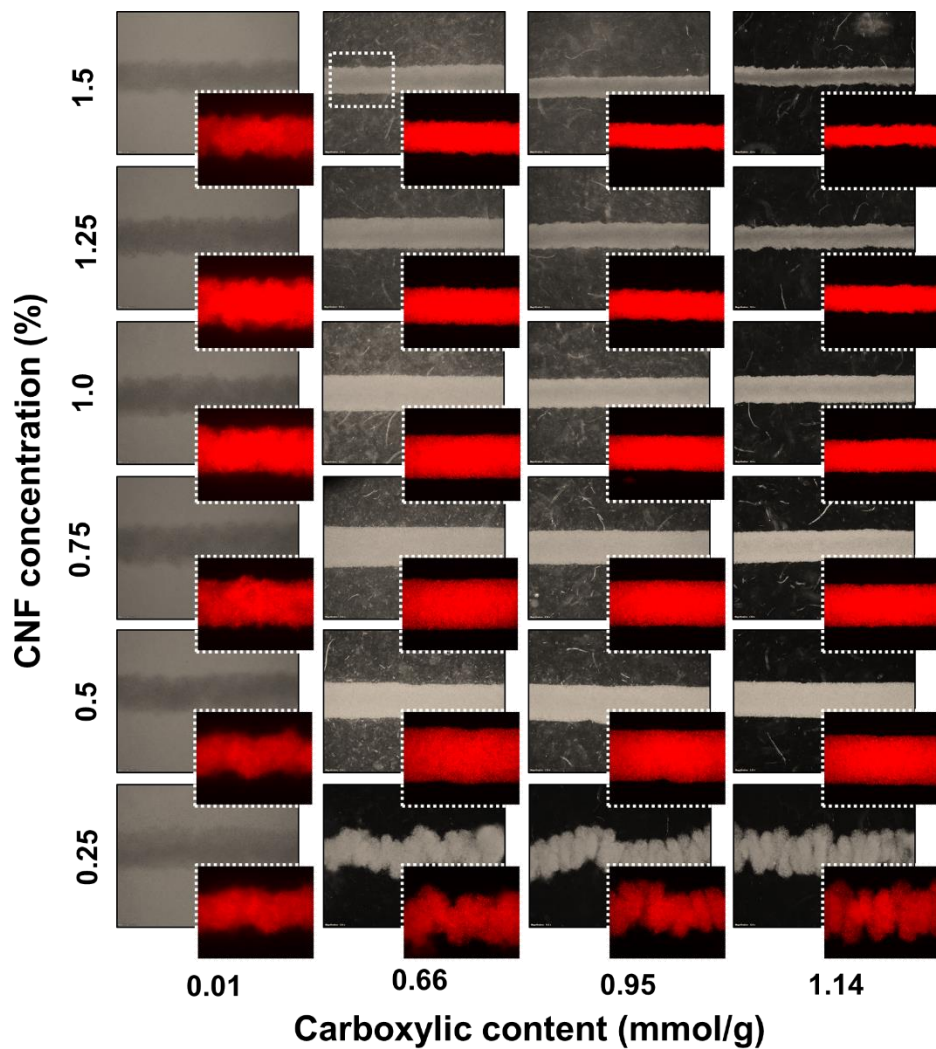
Figure 23. Optical and fluorescence microscopic images of linearly printed cross-linked polyacrylic acid based model inks at various CNF matrix conditions according to carboxylic contents and concentrations.
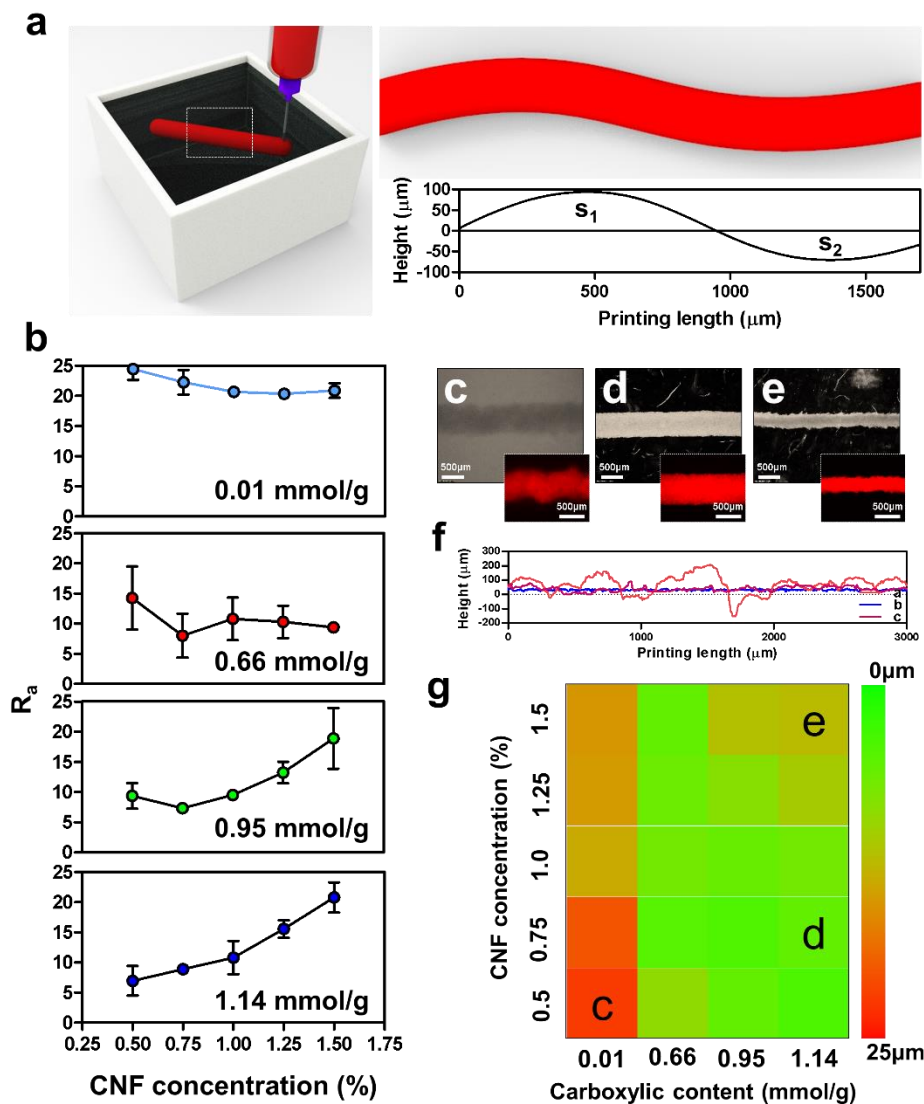
Figure 24. Evaluation of printing fidelity by the straightness of the line surface. (a) Schematic illustration of straightness analysis. (b) Changes in straightness at different CNF matrix conditions according to the carboxylic content and concentration. Optical and fluorescent microscopic images of the printed lines at CNF matrix conditions of (c) 0.01 mmol/g with 0.5%, (d) 1.14 mmol/g with 0.75%, and 1.14 mmol/g with 1.5%. (f) Straightness analysis with surface roughness of printed ink. (g) Color map of printing fidelity according to the straightness from 0 μm to 25 μm.

Based on the evaluation for the three factors, the high printing fidelity according to the carboxylic content and concentration was expressed as a green-colored area, and the low printing fidelity of printing was represented as a red-colored area (Figure 25a-25d). The non-carboxymethylated CNF matrix showed a low printing fidelity at all CNF concentrations, but the printing fidelity was improved with the use of a carboxymethylated CNF matrix. The concentration range showing excellent printing fidelity according to carboxylic content is shown in Figure 26d. Based on this result, a range of suitable CNF matrices for the printing of hydrophilic cross-linked polyacrylic acid model ink was suggested.

The CNF condition for the high printing fidelity was expressed by the range of yield stress. The yield stress range for the recovery of crevasses was represented by a light blue color (Figure 24e) The rapid recovery was observed in all CNF conditions except three conditions under the hydrostatic pressure (The height was set 3 mm in this experiment). The yield stress of the matrix was balanced with the yield stress of the ink and the printing fidelity was high in the yield stress range of 5 Pa to 15 Pa (a dark blue colored range).
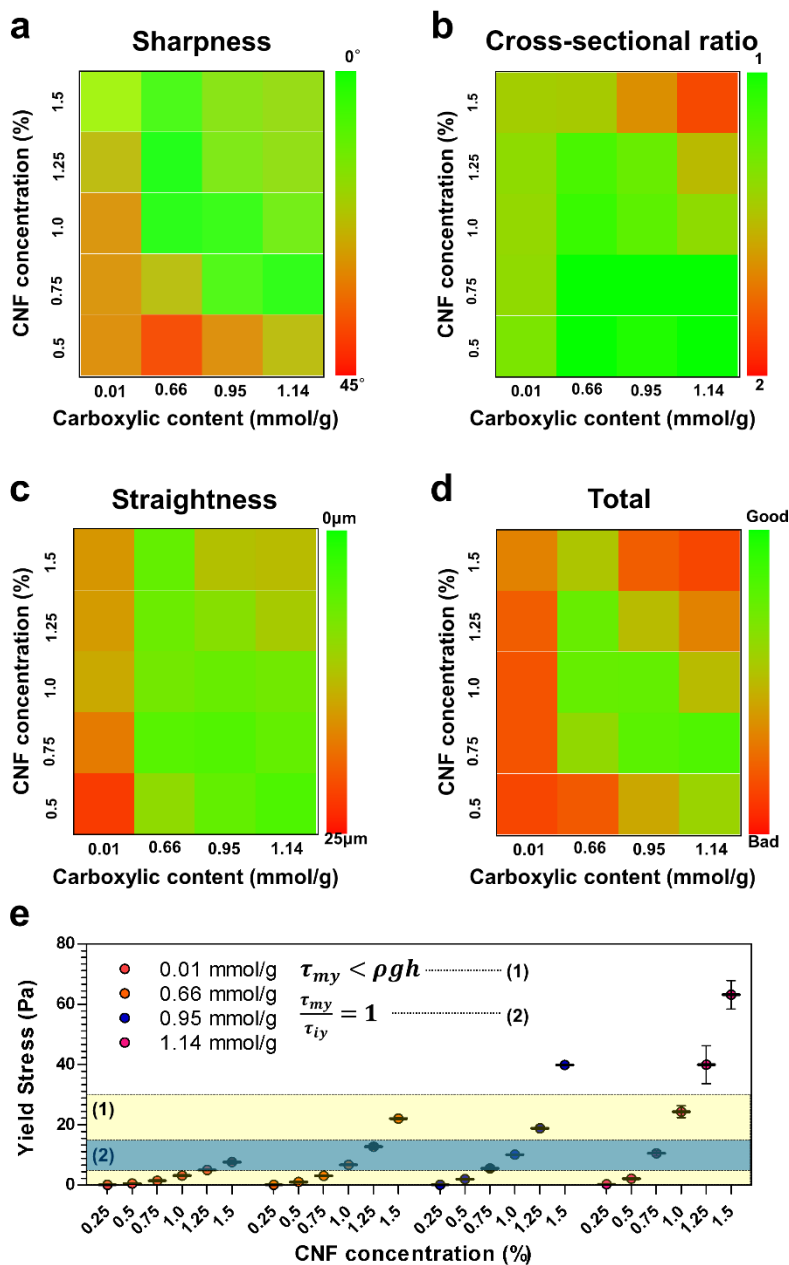
Figure 25. Color maps of printing fidelity. Printing fidelity according to (a) sharpness, (b) cross-sectional ratio, (c) straightness, and (d) total averages. (e) Yield stress area of CNF matrix with high printing fidelity. The area indicated in light blue represents the region satisfying the relationship between the yield stress of the matrix and the hydrostatic pressure, and the area indicated in dark blue represents the region satisfying the relationship between the yield stress of the matrix and the yield stress of the ink.

4.3.4. Evaluation of printing fidelity with hydrophobic ink.

In order to extend the usable ink to hydrophobic ink as well as hydrophilic cross-linked polyacrylic acid model ink, petroleum-jelly model ink was selected, and the previous evaluation methods were applied (Figure 26, 27). The sharpness of the hydrophobic petroleum-jelly ink was evaluated and shown in Figure 28a. As the concentration of CNF increased, θ_d decreased to approach the designed angle. As the carboxylic content increased, θ_d gradually decreased. Compared to the hydrophilic ink, the hydrophobic ink showed much larger θ_d because the ink was dragged due to the adhesion force between the hydrophobic ink and the stainless-steel needle, resulting in an obtuse angle.

In the case of the cross-sectional ratio, hydrophobic inks tended to be similar to hydrophilic inks (Figure 28b). In the low concentration of the CNF matrix, the cross-sectional ratio was 1 showed round shape. However, as the concentration of CNF increased, crevasses formed by the movement of the nozzle resulting in increasing of the cross-sectional ratio.

Based on the straightness of the printed ink, the hydrophobic ink was incompatible with the CNF matrix, resulting in a smooth surface with low R_a of less than 5 μm under most CNF matrix conditions (Figure 28c).

The color map is shown in Figure 28d, with the green-colored area shows high printing fidelity, and the red-colored are the opposites. In particular, unlike the hydrophilic ink, the printing was quite stable even in the non-carboxymethylated CNF matrix. The reason is that the hydrophobic ink has low miscibility with the CNF matrix. In principle, oil has a smooth surface at the interface with water. Hydrophobic inks also have a smooth surface at the interface with the hydrophilic CNF matrix. As a result, when hydrophobic ink is printed, it showed quite high printing fidelity even printing in non-carboxymethylated CNF matrix.

Diverse and more complex structures could be printed, including a triangular pyramid, a sphere, and a helix in a single pass (Figure 29a-29c). The highly resolved structures were imaged by mixing fluorescent particles in ink. The structures were sufficiently stable during printing and exhibited no significant changes after storage for approximately one month.
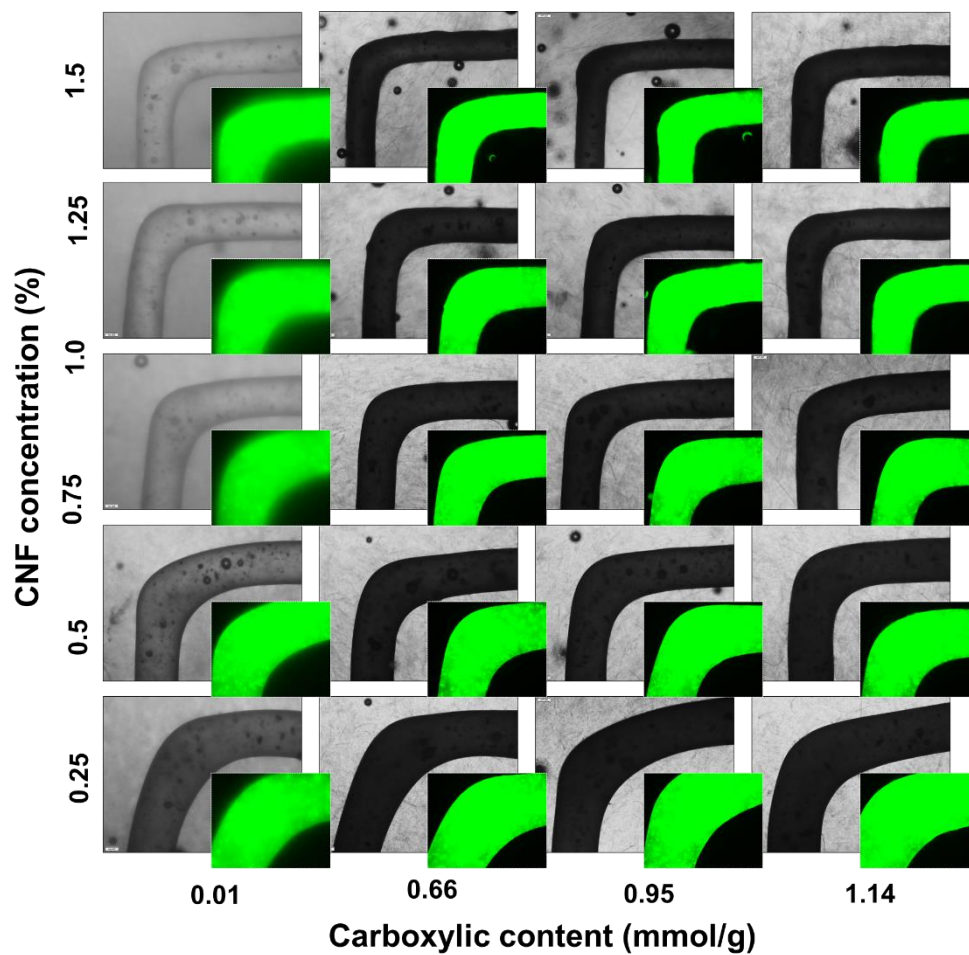
Figure 26. Optical and fluorescence microscopic images of printed petroleum-jelly inks at various CNF matrix conditions according to the carboxylic content and concentration.
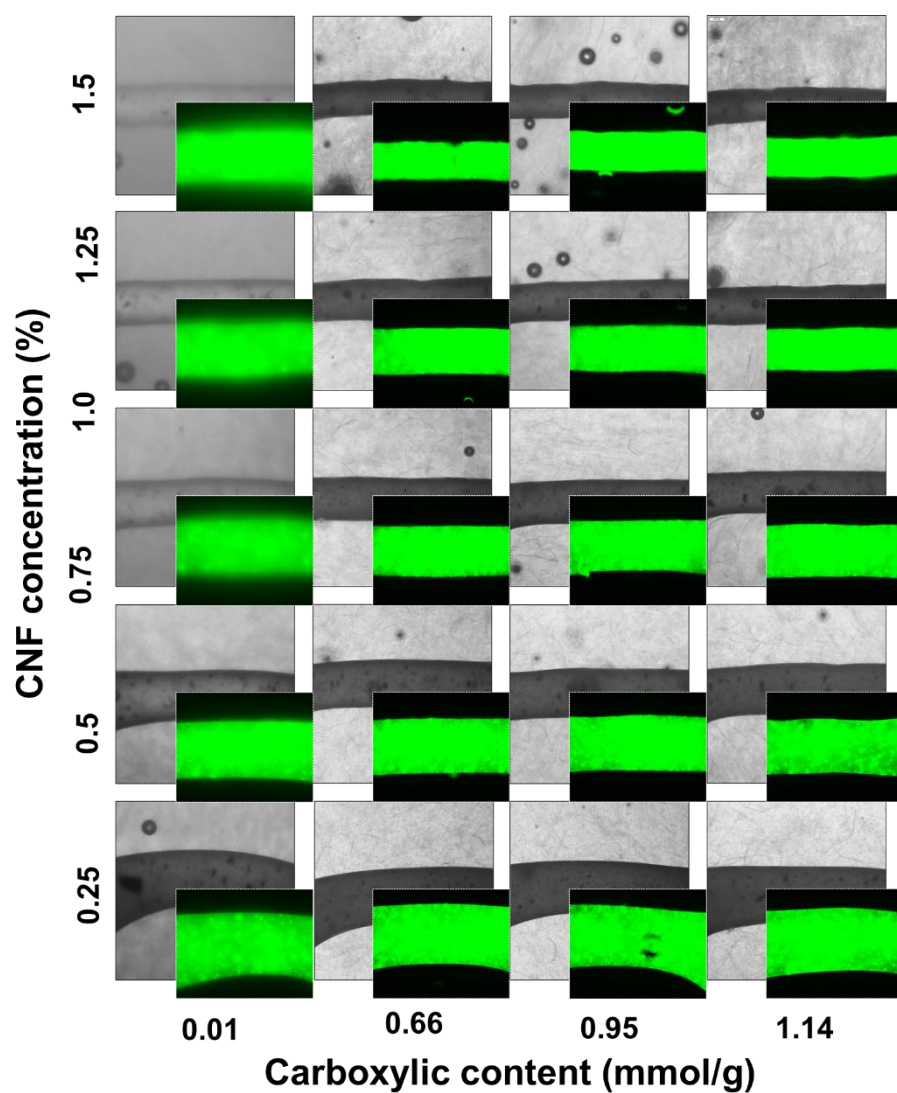
Figure 27. Optical and fluorescence microscopic images of linearly printed petroleum-jelly inks at various CNF matrix conditions according to the carboxylic content and concentration.
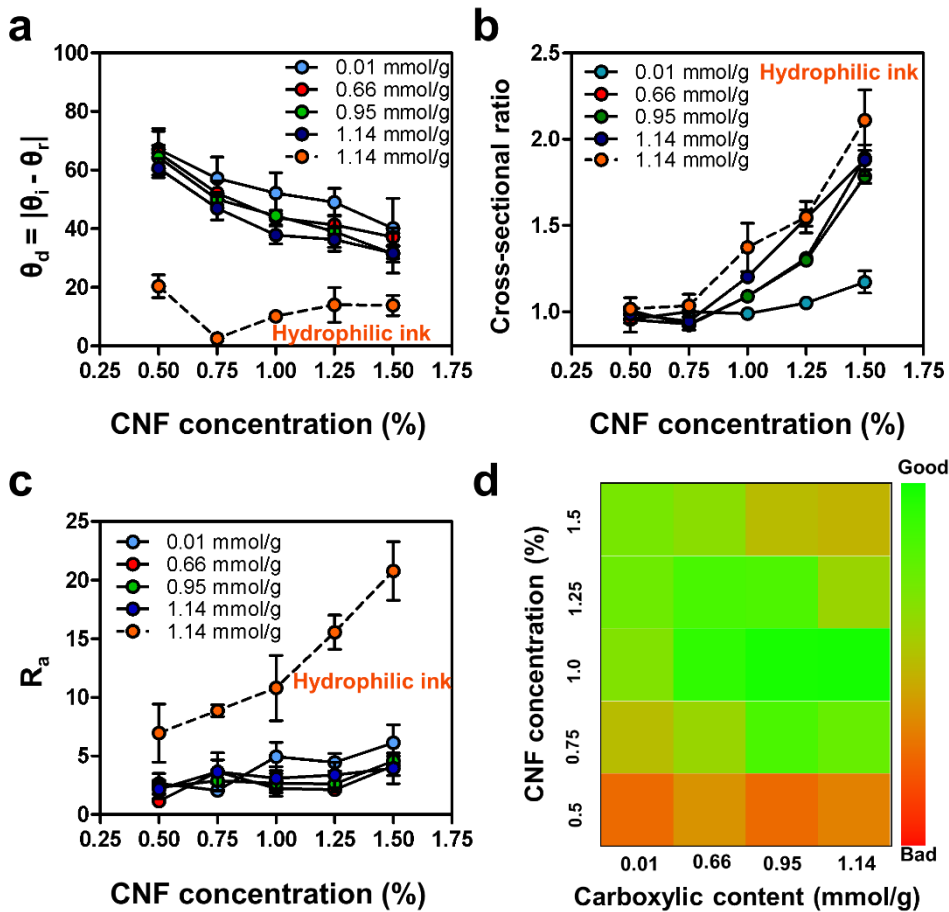
Figure 28. Evaluation of printing fidelity of CNF matrix with hydrophobic petroleum-jelly model ink. (a) Sharpness, (b) cross-sectional ratio, and (c) straightness evaluation by printing hydrophobic inks in various conditions of the CNF matrix. (d) Color map of printing fidelity of hydrophobic model ink in CNF matrix.
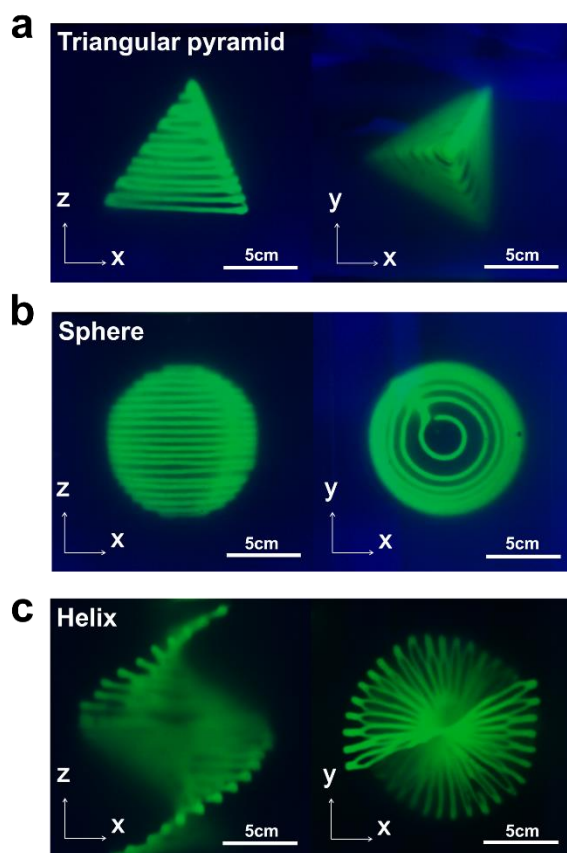
Figure 29. Creation of (a) triangular pyramid, (b) sphere, and (c) helix structures with petroleum-jelly ink. The ink contains green fluorescent microparticles for illumination. The structures were imaged from the side and the top.

The following schematic illustration could be presented based on the printing fidelity results (Figure 30a). The shape of the printed feature changed drastically depending on the rheological property of the printing matrix [95]. With a high fluidic CNF matrix, printed ink moved freely in the matrix, and curved lines were printed. However, as the stiffness of CNF hydrogel increased, the CNF matrix could support the printed features stably as designed. The use of too stiff CNF hydrogel as a matrix formed a crevasse along the nozzle path through the matrix, and the cross-section of the printed ink deviated from the circle to elliptical shape.

The rheological properties of the CNF hydrogel matrix were dependent on the fiber dimension and concentration. The dimension of the fiber was simply controlled by the degree of carboxymethylation. A low degree of carboxymethylation produced thick and long CNFs, while a high degree of carboxymethylation did thin and short CNFs. It led to a difference of entanglement between fibers under the same concentration, resulting in a difference in rheological properties (Figure 30b). In the case of CNFs having similar carboxylic content and fiber dimensional distribution, the point of fiber entanglement can be easily varied with the concentration (Figure 30c).
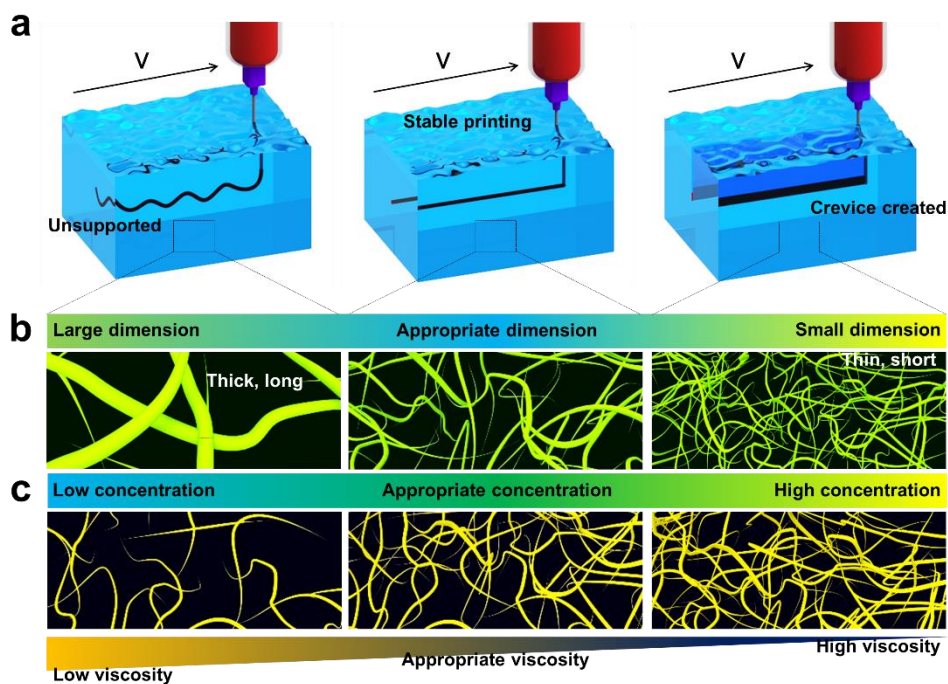
Figure 30. Schematic illustration of printing fidelity in various CNF matrix conditions. (a) Three types of printed ink shapes at various CNF matrix conditions with low, appropriate, and high viscosity. Viscosity change due to the CNF entanglements at different (b) fiber dimension and (c) concentration.

4.4. Evaluation of printing fidelity in multi printing lines feature.

4.4.1. Particle image velocimetry (PIV) test.

Particle Image Velocimetry (PIV) experiments were conducted to investigate the disturbing area in various conditions of the CNF matrix [84, 96]. The disturbing area of the matrix was formed around the nozzle moving within the matrix. For the experiment, a one-dimensional motion controller moved the nozzle inside the matrix incorporated with fluorescent microparticles. The microparticles flowing in the matrix at the bottom of the nozzle were observed with the nozzle pass through at a constant speed.

Figure 31a-31f shows the change of the flow field according to the concentration of the CNF matrix. The deformation of the matrix occurred around the moving nozzle, and the deformation area increased as the concentration of CNF decreased. It means that the structural deformation of a printed feature is possible and causes a decrease in printing accuracy. On the other hand, as the concentration of the CNF matrix increased, the deformation around the nozzle became irregularly protruding out of the straight-line shape. Because the CNF hydrogel is physically entangled with the fibers but not homogeneous as a whole, the CNF ink is discharged to a region where the interfiber density is relatively low. As a result, the morphology of the printed CNF feature became rough with the high concentration of the CNF matrix.

Also, the carboxylic content of CNF is a significant factor affecting the matrix deformation around the nozzle (Figure 32a-32d). Similar to the change in rheological behavior and the printing fidelity, the decrease of carboxylic content elevated the fluidity of the matrix at the same concentration. The CNF matrix with the large fiber dimensions resulted in the wide deformation compared with the CNF matrix with a smaller one.

Changes in CNF concentration and carboxylic content resulted in changes in the number of entanglement points between CNFs. As the concentration of

CNF increased, the number of entanglement points increased, making the matrix more resistant to deformation. This resulted in a change in the disturbing area formed by the stresses around the nozzles as they move between the matrices. Higher CNF concentrations could be more resistant to shear deformation, reducing the size of the disturbing area.
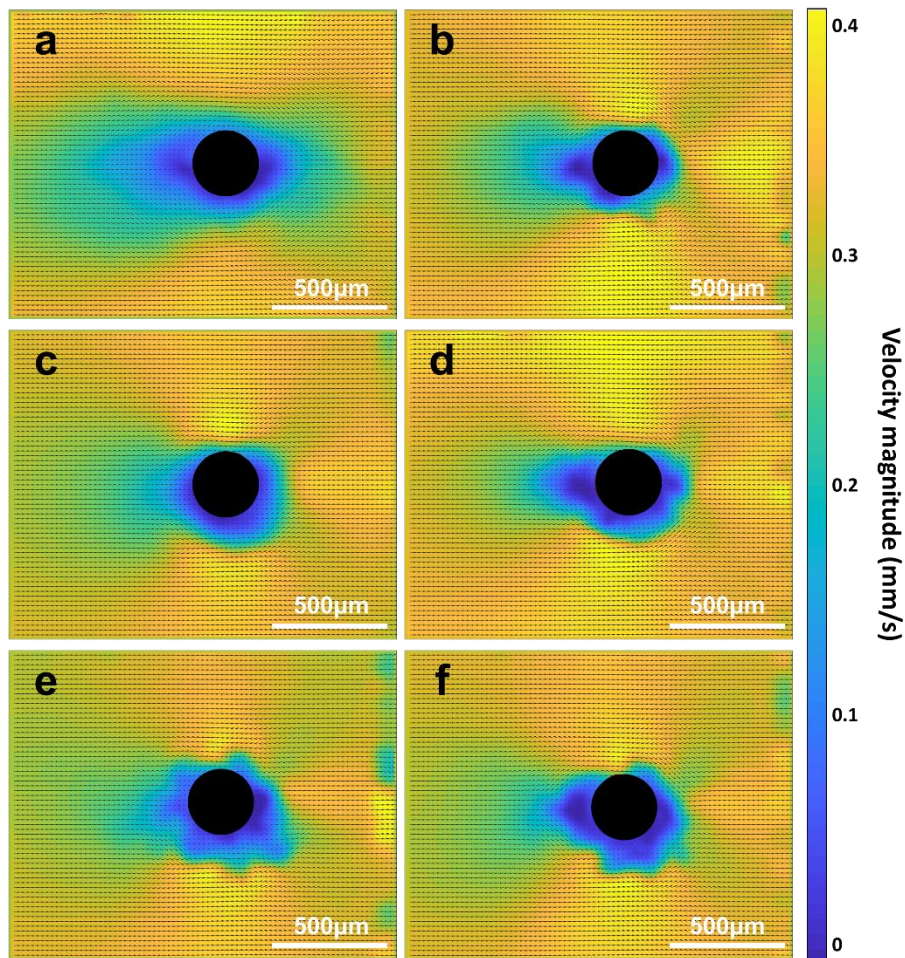
Figure 31. Velocity flow fields within the CNF matrix of varying concentration using a nozzle (outer diameter = 0.3 mm) moving at 0.4 mm/s from right to left. Flow fields according to the concentrations of the CNF matrix at (a) 0.25%, (b) 0.5%, (c) 0.75%, (d) 1.0%, (e) 1.25%, (f) 1.5%.
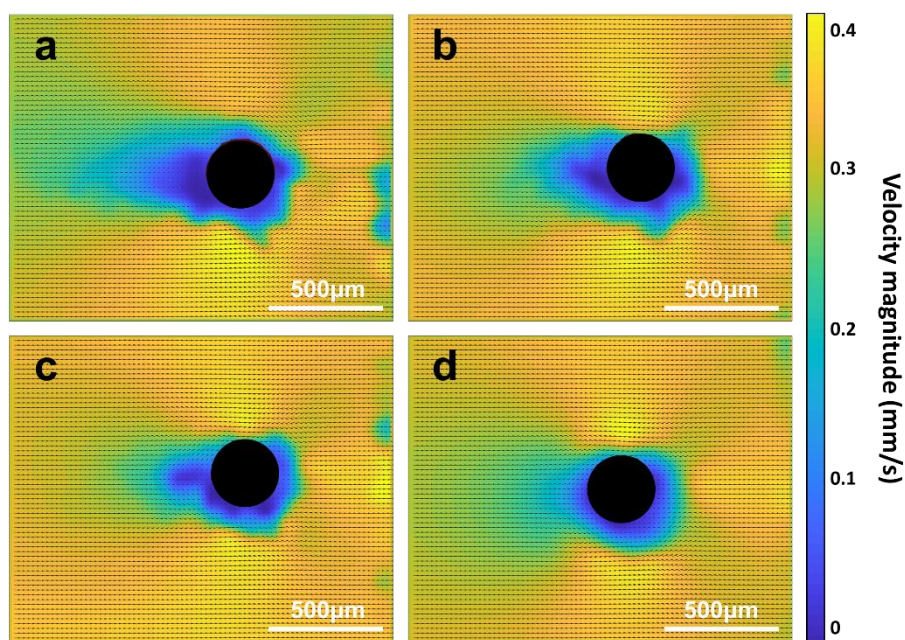
Figure 32. Velocity flow fields within the CNF matrix materials of varying carboxylic content using a nozzle (outer diameter = 0.3 mm) moving at 0.4 mm/s from right to left. Flow fields according to the carboxylic contents of the CNF matrix at (a) 0.01 mmol/g, (b) 0.66 mmol/g, (c) 0.95 mmol/g, (d) 1.14 mmol/g.

4.4.2. Velocity magnitude around nozzle.

The velocity profiles in front of and behind the nozzle were examined for the CNF matrix. The disturbing area around the nozzle was found to be larger at the front side. The disturbing area or the yielding area of the CNF matrix around the nozzle depended on the carboxylic content and concentration. Figure 33a shows the profiles of velocity magnitude according to the change of carboxylic content. As the carboxylic content of CNF increased, the yielding area formed around the nozzle gradually decreased. It indicates that the CNF matrix with a high carboxylic content has a lower possibility of affecting the printed result as the nozzle moves around the already printed ink features, thereby improving the accuracy of the printed features.

As the concentration of the matrix increased, the yielding area around the nozzle gradually decreased (Figure 33b). It revealed that the disturbances in flow decay within less than one tip diameter at the CNF concentration over 0.75%.
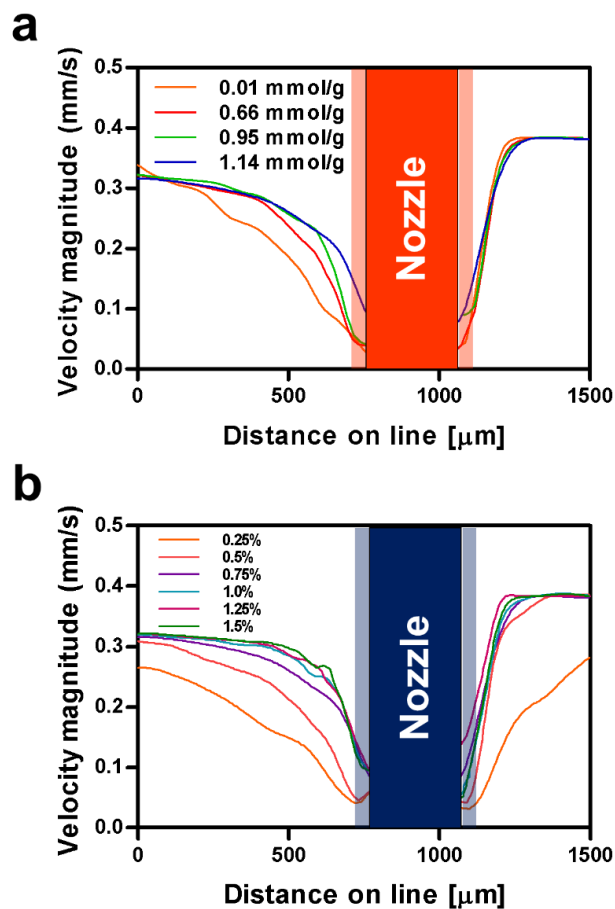
Figure 33. Effect of CNF concentrations and carboxylic contents on the velocity distribution in front of and behind the nozzle. Velocity magnitude profiles of the CNF matrix at different (a) carboxylic content and (b) concentration of the CNF matrix.

4.4.3. Matrix composition and printing path effects on fidelity.

Printing was carried out in order to visualize the effect of the yielding area on the actual printing result according to the matrix conditions. Figure 34a shows that the already printed line feature can be deformed as the nozzle moves around.

The crosslines were designed using three paths and the printing accuracy was analyzed by observing the features of the printed ink (Figure 34b). The images of the patterned features reveal how matrix yielding impacts their fidelity. The first one was the path that prints the crossline by drawing two perpendicular lines. Printing was performed closer to the center of the crossline in a higher CNF concentration matrix. These results were prominent in the second path of the crossline by drawing four lines from the outside to the center. This is because the line already printed is affected more by the movement of the nozzle in the low-density CNF matrix. The third line was printed through two straight lines, and the printed straight line appeared to bend. The bending phenomenon was alleviated as the CNF matrix concentration decreased.

Comparing these results, the matrix composition plays a critical role in enabling patterns that most closely resemble the desired 3D form. These results also indicate that the print path influences printing fidelity. The printed 3D form exhibits the closest resemblance to the desired form using printing path number 3.
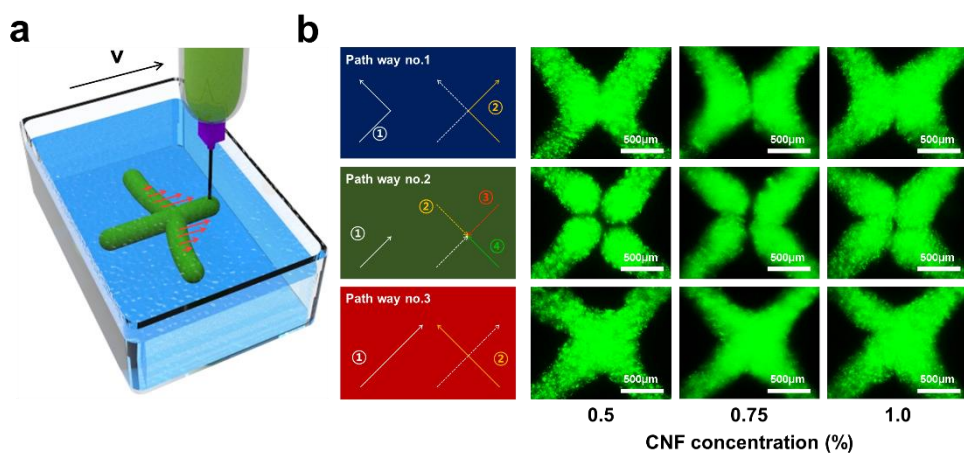
Figure 34. Matrix composition and printing path effects on the printing fidelity. (a) A schematic illustration of deformation occurred in already printed ink as the nozzle moves. (b) Three paths for evaluation of printing fidelity in multi printing lines at different CNF matrix concentration.

4.5. Printing of various ink materials.

4.5.1. Rheological properties of various ink materials.

Various ink materials can be printed inside the CNF matrix if the rheological properties of the inks are met (Figure 35a). In addition to the cross-linked polyacrylic acid-based model ink, hydrophilic CNF and hydrophobic petroleum-jelly and silicone represented high printing fidelity. Rheological property of CNF was adjusted to print living cell embedded bio-ink while liquid paraffin and fumed silica were used to adjust the viscosity of petroleum-jelly and silicone inks, respectively. Ink materials with different properties were printed in the CNF matrix, which was optimized earlier. In addition to hydrophilic inks, hydrophobic inks were printed stably. (Figure 35b).
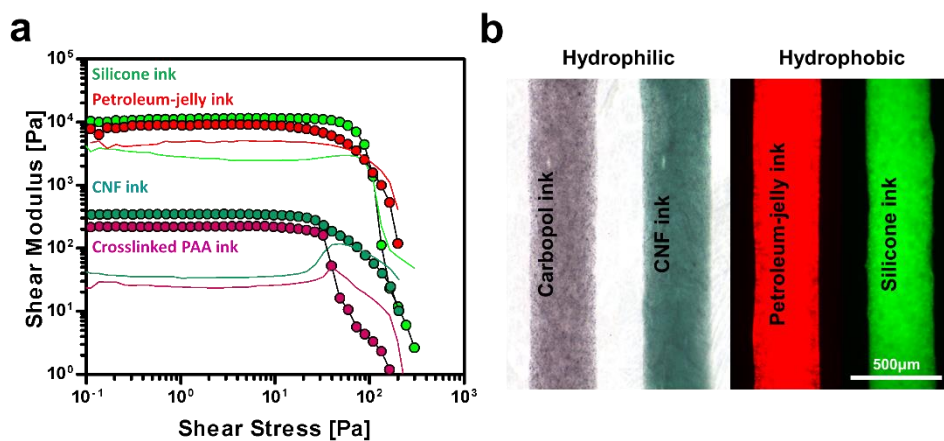
Figure 35. Printing of the various inks in the CNF matrix. (a) Shear modulus of various types of ink. As hydrophilic ink, cross-linked polyacrylic acid ink and CNF ink were used, and as hydrophobic ink, petroleum-jelly ink and silicone ink were used. (b) Optical and fluorescent microscopic images of various inks printed in the CNF matrix with the carboxylic content of 1.14 mmol/g and the concentration of 0.75%.

4.5.2. Living cell embedded 3D bio-printing.

It was possible to cultivate living cells inside the CNF matrix by printing CNF based bio-ink containing cell growth media inside the CNF matrix (Figure 36). The CNF matrix could be a suitable composition for the 3D cell culture. The cell-laden structures were fabricated by printing CNF based bio-ink containing fibroblast cells. The finely printed cells were stably positioned in the CNF matrix, and hollow tubular structures were produced. The cells were well survived inside the CNF matrix forming various sizes of cell pockets by controlling the printing speed or the pressure applied.

4.5.3. Feasibility test of printed silicone actuator.

To explore the range of 3D printing capabilities enabled by the CNF matrix, the complex silicone elastomer structure was constructed (Figure 37a). In the case of soft materials such as silicone, it was possible to obtain highly accurate results with the support of matrix when making more complex shapes such as a stacked structure or a complex entangled vascular structure. The shape change of the silicone actuator fabricated inside the CNF matrix was confirmed by applying pneumatic or hydraulic pressure (Figure 37b). Printing silicone ink was very challenging, and it would be possible to make more complex shapes of silicone mold through the CNF matrix. Because the CNF matrix system can freely print not only hydrophilic ink but also hydrophobic ink, it is expected to have a higher value in use.

Conventional 3D printing methods made it difficult to fabricate complex structures such as the silicon structure shown in Figure 37. The structure formation was better than the reported silicon-based matrix, but the printing fidelity was similar to that of the carbopol-based matrix. Divided into terms of printing resolution and printing fidelity, this study is meaningful in suggesting a method to evaluate printing fidelity quantitatively.
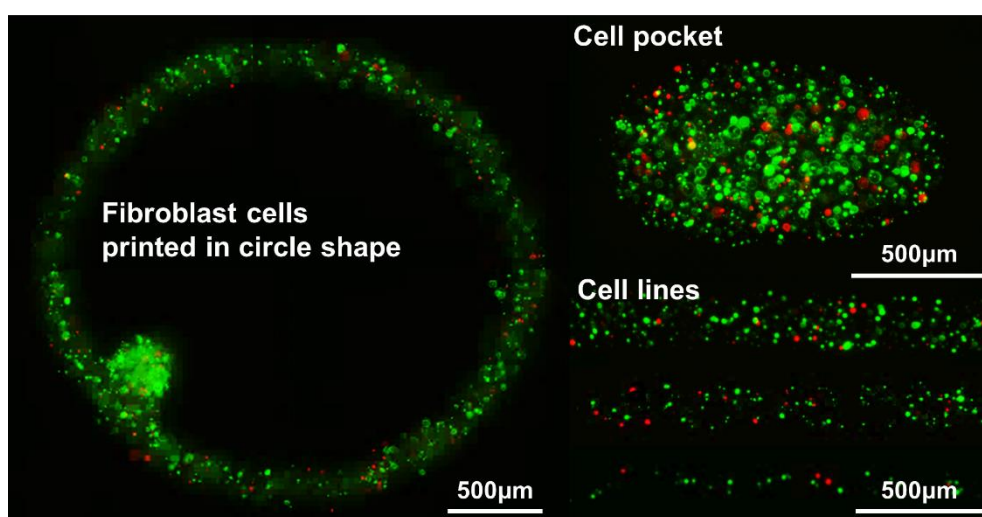
Figure 36. Living cell printing inside the CNF matrix with the carboxylic content of 1.14 mmol/g and the concentration of 0.75%.
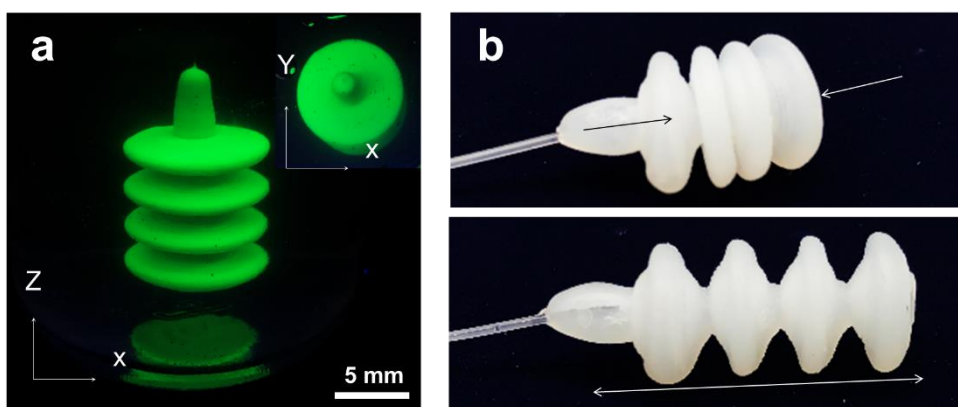
Figure 37. Printing of silicone elastomer-based soft actuator. (a) Optical image of the printed complex silicone elastomer structure inside the CNF matrix with the carboxylic content of 1.14 mmol/g and the concentration of 0.75%. (b) Feasibility test of 3D printed silicone elastomer-based actuator by the pneumatic or hydraulic pressure.

4.6. Fabrication of CNF based open-channel microfluidic devices.

Hydrophobic petroleum jelly was chosen as a counter ink material due to its immiscibility with the hydrophilic CNF hydrogel matrix and the ease of removal from the matrix after drying. The fabrication of microfluidic devices with multilayered channels in a film was achieved in three steps. The first step was to print the channels designed using CAD with a removable ink. As the nozzle moved through the CNF hydrogel matrix, the removable petroleum-jelly ink was printed inside the matrix (Figure 38a). The printing could be routinely performed, and three different shapes of channels were printed inside the matrix at different levels, which were interconnected through a junction between the layers (Figure 38b, c). The second step was to dry the CNF hydrogel with printed features at room temperature. During the drying process, the CNF hydrogel matrix formed a condensed film structure that was still flexible (Figure 38d). The petroleum-jelly ink was stable over the drying process, and no leakage or damaged structure was observed. The third step was to remove the petroleum-jelly ink from the inside of the CNF films for the creation of channel structures. The petroleum-jelly ink started to liquefy above the melting point (>70 °C). This enabled the easy removal of the ink from the dried matrix and the formation of open-channel structures by flowing compressed air (Figure 38e). By using this facile method, various microfluidic channels such as straight lines, curves, intersections, and pockets could be fabricated (Figure 38f). Printed inks are fused at the meeting point of the printing nozzle at the same layer forming the intersections. The pocket designs could be introduced by positioning the needle during extrusion without X, Y, or Z translation. The pocket volumes could be easily controlled by adjusting the applied pressure or extrusion time.
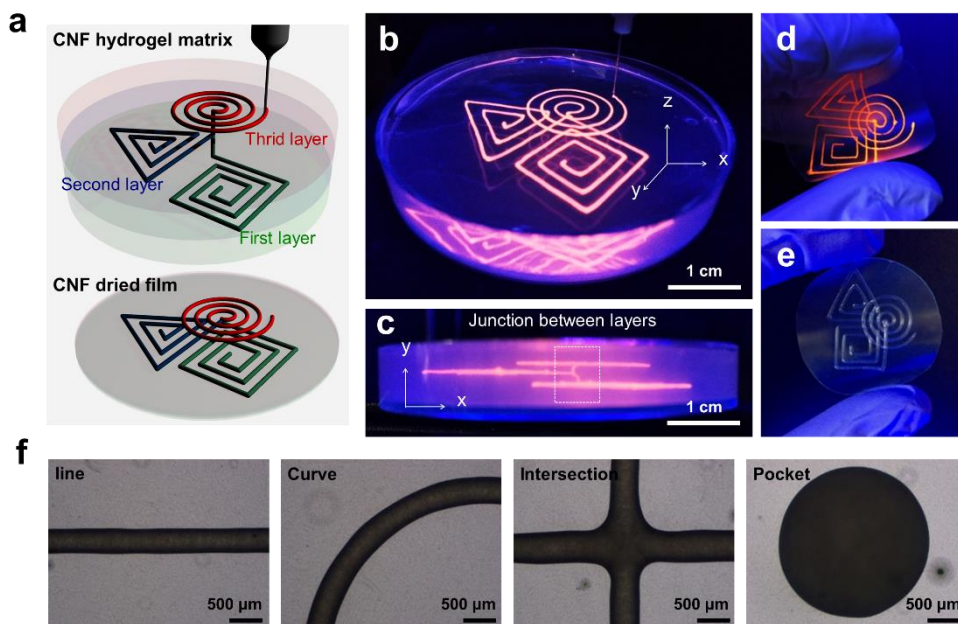
Figure 38. Fabrication of a flexible microfluidic thin film with multilayered channels by matrix-assisted 3D printing in the CNF hydrogel. (a) Series of fabrication processes for three-layered continuous microfluidic channels designed by CAD. (b) Nozzle tip was moved to the three layers, and the petroleum-jelly-based removable ink was injected in the CNF hydrogel matrix. (c) It was possible to interconnect the layers by continuous injection of the ink in tip movement to the next layer. (d) CNF hydrogel matrix was dehydrated and formed a thin, compact microfluidic film. (e) Printed ink was liquefied at elevated temperature and removed under vacuum, forming an open-channel 3D microfluidic device. (f) Different shapes of channel patterns formed in CNF films.

4.6.1. Feasibility test of microfluidic channel devices.

The CNF hydrogels formed a highly transparent film. The clarity of the CNF film was unique compared to that of normal cellulose paper used in analytical chemistry, with a potential enhanced efficiency for detection [176]. The highly transparent substrates enabled the direct observation of the flowing channels rather than the reflection from the paper surface. Channels were connected to silicone tubing using a stainless-steel bridge (Figure 39a). The thickness of a CNF microfluidic device consisted of three-layered channels located vertically (Figure 39b). Two streams of aqueous dye solutions flowed through the separate microfluidic channels and met at a junction, making a laminar flow of the two streams through the CNF microfluidic channels (Figure 39c, d). The CNF-based open-channel microfluidic devices could produce the same diffusion-limited flows reported in conventional PDMS open-channel microfluidic devices (Figure 39d) [187]. The inside of the channel was coated with silicone elastomer to prevent liquid penetration through the channel surface (thickness: 26.33 ± 5.68 μm). The fibrous structure of the channels disappeared, and a new nonporous surface was formed after the coating, inferring uniform coating of the surfaces (Figure 39e, f). The surface roughness was significantly reduced from RMS 4.09 nm to RMS 0.88 nm after the coating, confirming the effective coating of the CNFs with silicone elastomer (Figure 39g).
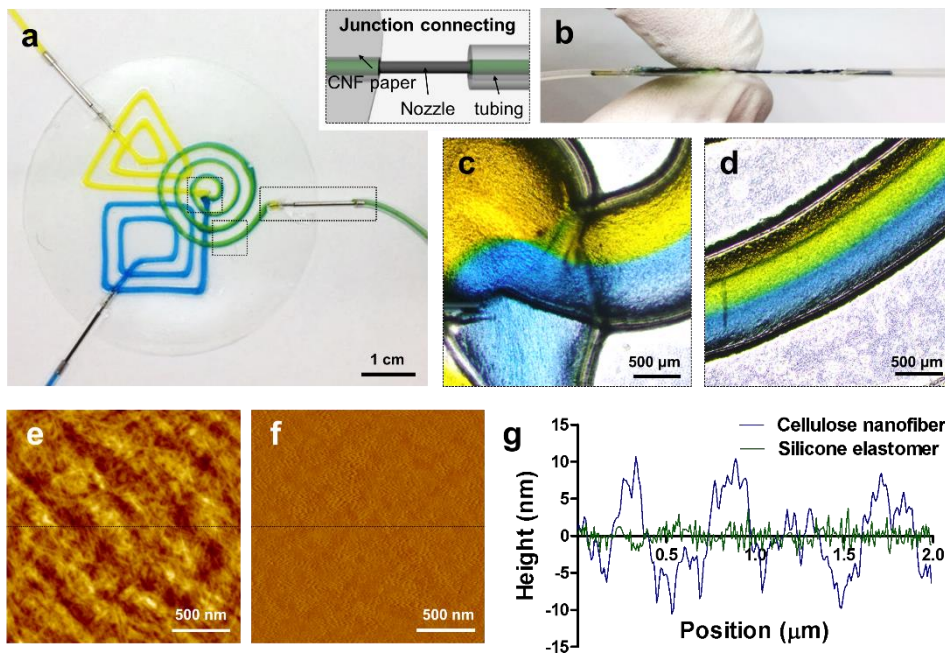
Figure 39. Feasibility test of microfluidic channel devices. (a) Injection of two dye solutions to two separate channels. (b) Thickness of a CNF microfluidic device consisting of three-layered channels located vertically. Optical images of the junction area (c) and laminar flow in the CNF microfluidic channels (d). The channel surface was coated with silicone elastomer to prevent water absorption. The fibrous channel surface (e) was modified into a smooth surface (f), and the surface roughness changed significantly after coating (g) and was confirmed by AFM.

4.6.2. Control of channel diameters.

The elusion volume of the microchannels was closely related to the cross-sectional area of the channel, which was controlled by dynamic pressure variation from 10 to 60 psi in extruding the ink under the printing speed at 5 mm s^{-1}. The cross-sectional area of the channels was calculated by measuring the diameter of the extruded lines (Figure 40a, b). It was determined to increase linearly according to the applied pressure because of the larger amount of ink in the same period under higher pressure (Figure 40c). A series of channels with different diameters could be fabricated by simple adjustment of the dynamic pressure during printing, as shown in Figure 40c.
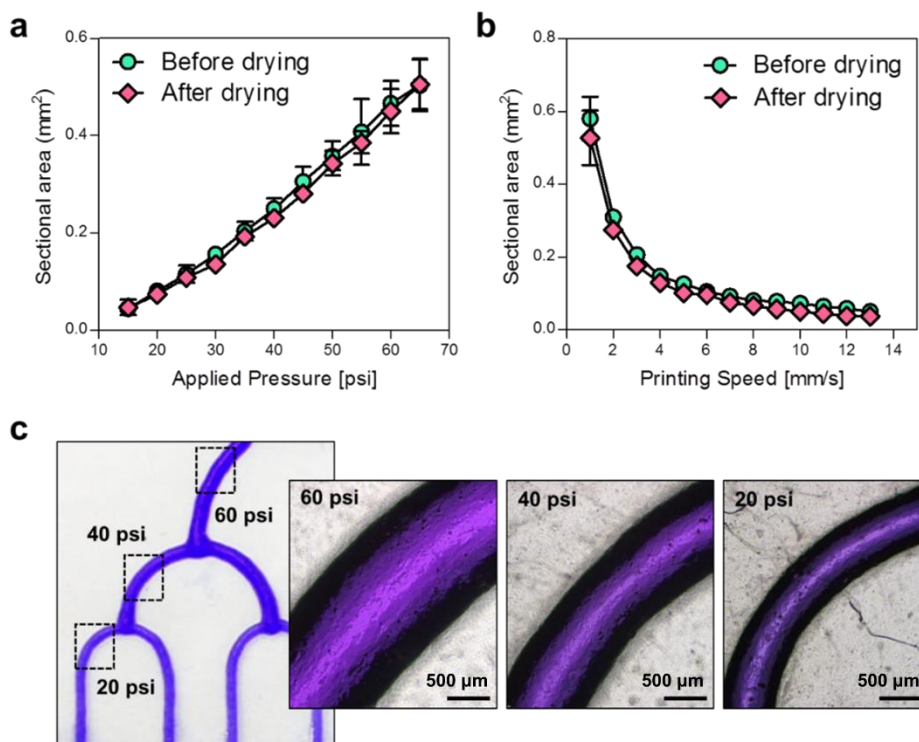
Figure 40. Control of channel diameters by pressure applied to the 3D-printing ink. (a) As a function of applied pressure at a printing speed of 5 mm s^{-1} and (b) as a function of printing speed at an applied pressure of 25 psi using a 160 μm cylindrical stainless steel nozzle at 25 °C. (c) Channel size was controlled by simple adjustment of the applied pressure on the printed inks, which maintained their size after drying of the matrix.

4.6.3. Dimension control of the microfluidic device.

Conventional paper-based open-channel microfluidic devices must be stacked to prepare 3D channel designs [188]. In contrast, the proposed strategy here can control the positioning of the layers and their interconnection three-dimensionally through CAD design. The lower extruding dynamic pressure of the ink formed narrower structures, which required smaller spacing between the layers to resolve the structure (Figure 41a). Unless the minimum distance between the layers was not satisfied at a certain applied pressure, the printed structures were merged, and the solutions were mixed in the fused region. Two different dye solutions flowed through the device to examine the 3D microfluidic design (Figure 41b). The solutions flowed along the channels and mixed at the junction of the channels, turning green with a 0.4 mm spacing microfluidic design. Each solution flowed through the channel without mixing, with a 1.0 mm spacing microfluidic design; a dense CNF film barrier was formed in the middle of the channels during the drying process (Figure 41c). With the proposed matrix-assisted 3D-printing methods, it was possible to integrate the 3D channels. The thickness of the overlaid area increased linearly according to the number of channels used (Figure 41d). A total of six channels was overlaid in the investigation, and six colors of solution were injected into the channels separately. Amazingly, the open-channel microfluidic device delivered six solutions without mixing in the device, confirming well-resolved multilayer microfluidic devices less than 1 mm thick (Figure 41e).
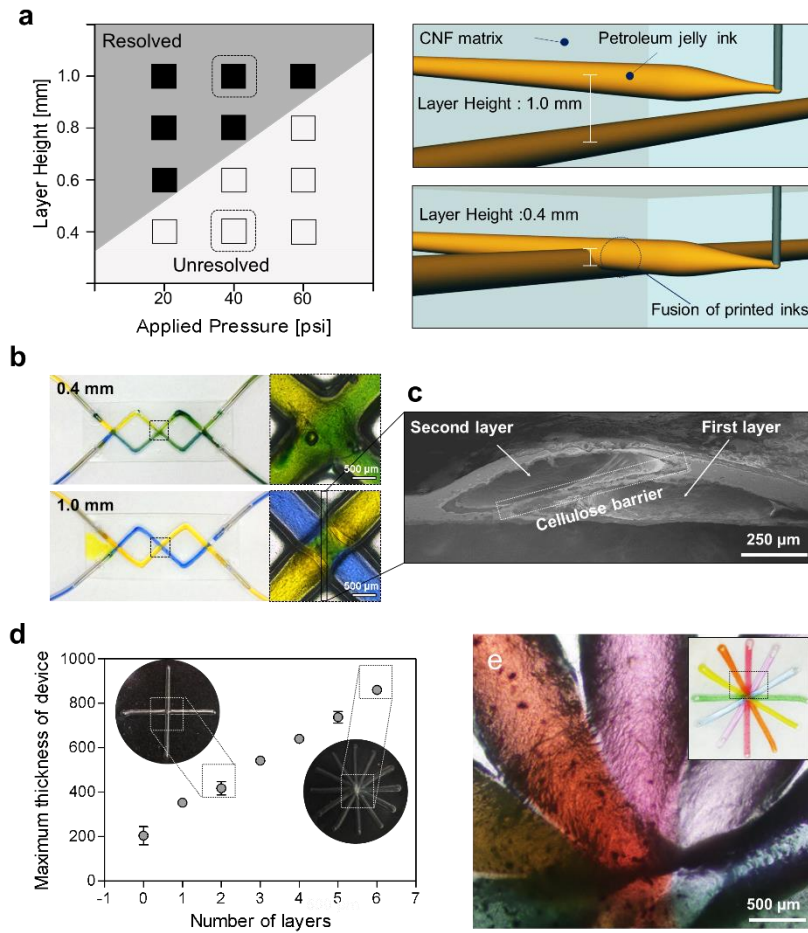
Figure 41. Dimension control of the microfluidic device. (a) Processing map for determining the dimension of the microfluidic devices, denoting regions resolved between the layers (filled-in squares) and unresolved between the layers (empty squares) as a function of the layer height between the nozzle tip and the applied pressure. (b) Two different dye solutions flowed through the devices at different layer height conditions. (c) Detailed image of the cross-sectional 3D microfluidic devices showing the two channels blocked by a cellulose barrier. (d) Variation of the maximum thickness of the device depending on the integration of the multilayered channels. (e) Photographs of six different solutions flowing in six-layered microfluidic devices without mixing.

4.6.4. Feasibility of pH sensor.

The CNF film containing a network of interconnected pores generally exhibited higher permeability to liquids than the solid materials normally used to fabricate microfluidic devices. The closed detection systems using PDMS or other plastic-based microfluidic devices maintained the inertness with molecules during the flow [189]. Meanwhile, a CNF-based microfluidic device allowed molecules to transport across the cellulose barrier, and the molecules were adsorbed at the channel surfaces as an open system. The open system had a variety of attractive features compared to the PDMS-based microfluidic devices. First, simple and active sensing was possible in a single channel line. Second, it was possible to integrate the open channels with a wicking zone through locational control of selective coating.

The high water permeability of an uncoated CNF matrix was the key to the active colorimetric pH sensor. The transparency of the CNF channels enabled the detection of a color change responding to the binding of molecules. The inside of the channels was coated with a silicone elastomer selectively, but the coiled region was left uncoated after the printing of the CNF-based microfluidic channels. A universal indicator was dropped in the coiled region for the detection of pH changes (Figure 42a). It was convenient to monitor the chemical changes occurring inside the channels according to acidity (Figure 42b). Flows of 1 M NaOH caused a color change in the channel to dark purple. Subsequently, the 1 M HCl solution caused a dramatic change in color to red. The device detects pH changes simply in real-time without any sophisticated equipment.
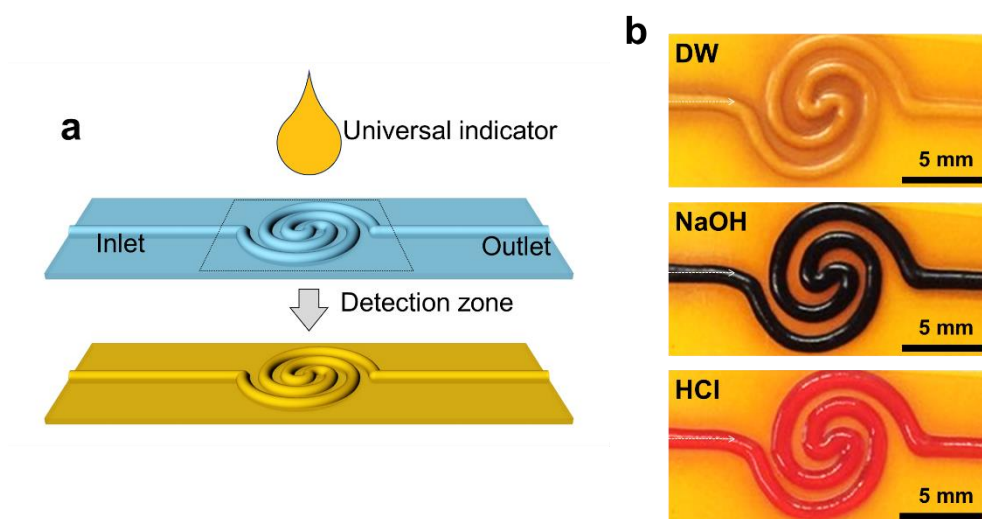
Figure 42. pH sensing devices. (a) Design of the detection zone of a CNF microfluidic device. A universal pH indicator solution was dropped at the surface of the detection zone and dried until use. (b) Streams of DW, 1 M NaOH, and 1 M HCl were injected into the device sequentially.

4.6.5. Colorimetric analysis of heavy metal ions.

The CNF-based platform is also applicable to monitoring heavy metals using pH-dependent reactions. The specific reaction between heavy metal ions and chemicals was considered at a certain pH condition, such as Ni^{2+} and dimethylglyoxime at pH 9 and Cr^{6+} and diphenylcarbazide at pH 1. For the feasibility of a device, a heavy metal solution was injected into the center inlet and mixed with buffer solutions of 10% H_2SO_4 and 1% NaOH injected into the different paths of the channels. The mixed solution reacted with either dimethylglyoxime or diphenylcarbazide in the detection zone (Figure 43a). Specifically, Ni^{2+} ions reacted with dimethylglyoxime under basic conditions, causing a colorimetric change to pink, and Cr^{6+} ions reacted with diphenylcarbazide under acidic conditions, causing a colorimetric change to purple. The changes in color in the monitoring zones were measured according to the metal ion concentration using UV–vis spectroscopy. The intensity of the peaks increased linearly as a function of the ion concentration (Figure 43b, c). The intensity of the absorbance increased linearly as the ion concentration increased. The mixed-ion solutions showed the same absorbance as the single-ion solutions, inferring the high selectivity of the device (Figure 43d).
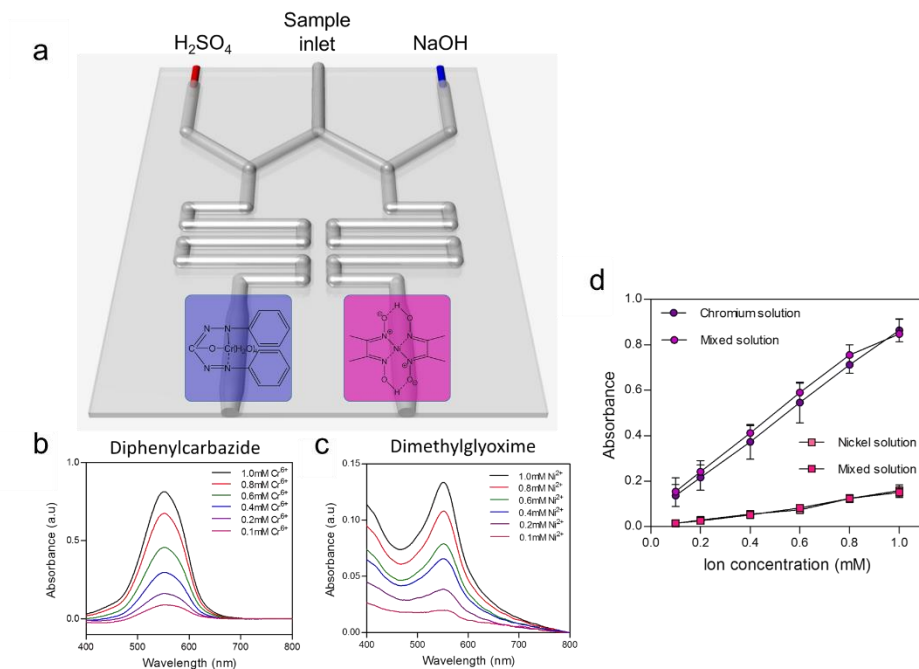
Figure 43. Colorimetric analysis of heavy metal ions in a dual-mode. (a) Schematic drawing of the microfluidic device design for sensing heavy metal ions Ni^{2+} and Cr^{6+}. UV-vis spectra obtained at different concentrations of (b) potassium dichromate and (c) nickel nitrate hexahydrate for selective capture of heavy metal ions. (d) Calibration curves for the detection of Ni^{2+} and Cr^{6+} ions.

4.7. Fabrication of CNF based open cell culture platform.

Diffusion control of molecules is one of the critical factors in the design of microfluidic cell culture devices [190]. Here, hydrophilically modified CNF (Hphil-CNF) hydrogels were patterned in the matrix of hydrophobically modified CNF (Hphob-CNF) using matrix-assisted 3D. First, a nozzle was placed at the surface of the Hphob-CNF matrix, and Hphil-CNF hydrogel was printed to form a cubic 3D hydrogel structure (Figure 44a). Then, a petroleum-based ink was printed through the Hphob-CNF matrix and Hphil-CNF 3D structures according to the design of microchannels for the microfluidic devices (Figure 44b). Dehydration of CNF hydrogels formed a highly dense and transparent CNF film embedding the petroleum-based ink micropatterns. The petroleum-based ink was removed from the film at elevated temperature, creating channel structures in the film. The Hphil-CNF region in the dehydrated CNF film was water absorbable and mass transportable through the thickness, while the outer region consisting of Hphob-CNF was water repellent, resulting in selective diffusion of molecules in aqueous solution (Figure 44c). Fabrication of these water-absorbable structures in CNF films enabled controlled transport of molecules through the diffusible patterns, and the response of cells incubated on the surface was investigated with an environmentally-friendly system (Figure 44d, e). It would be possible to use the other hydrophobic materials for the water repellent matrix instead of Hphob-CNF. However, it is advantageous to use Hphob-CNF for the fabrication of diffusible patterns because of the high compatibility with Hphil-CNF at the interface and nanofibrous morphology of the matrix surface, which improves the cell attachment and mechanical strength of the hydrogel.

Patterning of a selective diffusible layer was performed by a controlled injection of ink in the path of a printing needle, as shown in Figure 45a. Yellow fluorescent polystyrene particles in the printed ink were displayed

clearly in the blue fluorescent matrix under UV irradiation. The patterns of Hphil-CNF ink were stably printed at the surface of the Hphob-CNF matrix as designed. An elliptical diffusion region of Hphil-CNF was prepared by the alternate positioning of the discharged and non-discharged areas in a straight printing line. The flexible design of the diffusive patterns was verified by printing a repetitive serpentine shape of Hphil-CNF. Figure 45b shows the printing of channel structures with petroleum jelly ink incorporated with green fluorescent particles in the Hphob-CNF matrix. Highly resolved fluidic channels were fabricated in the CNF films after the removal of petroleum jelly patterns at elevated temperatures.
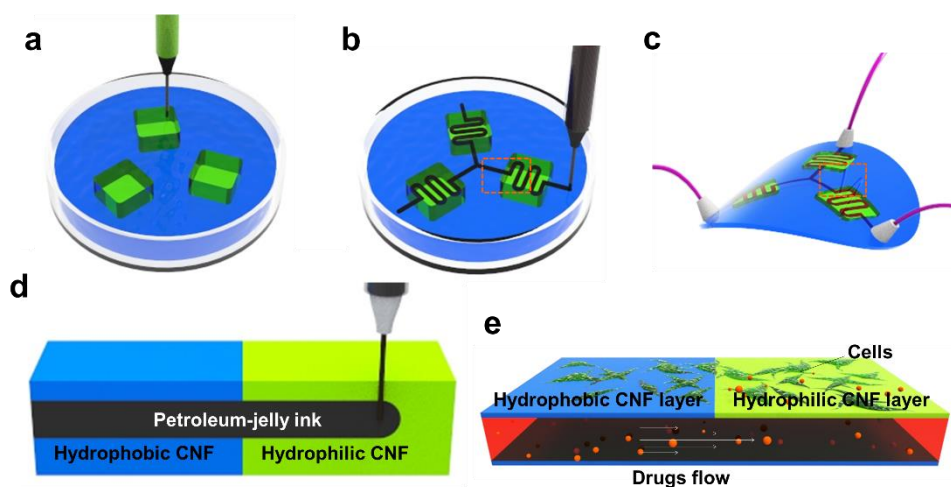
Figure 44. Schematic illustration of the CNF-based cell culture platform embedding a microfluidic system. (a) 3D printing of Hphil-CNF in the matrix of Hphob-CNF hydrogel. (b) Matrix-assisted printing of petroleum jelly ink in the CNF hydrogels. (c) Dehydration of hydrogels for the formation of a condensed film microfluidic device. (d) Formation of channels in the Hphob-CNF and Hphil-CNF hydrogels in the process shown in (b). (e) Cell culture platform for selective diffusion of molecules from the flow.
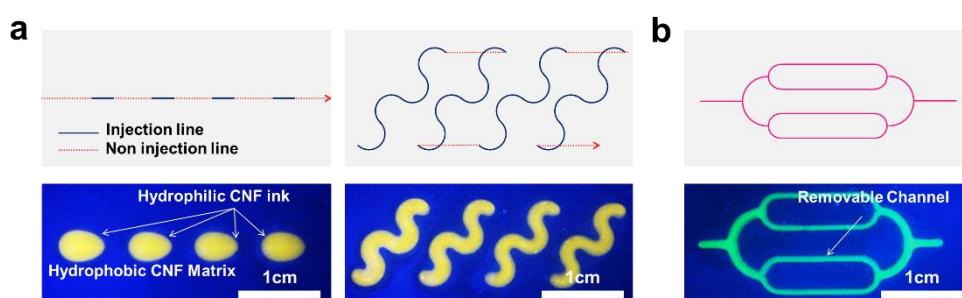
Figure 45. (a) Photographs of matrix-assisted 3D printing of the Hphil-CNF ink in the Hphob-CNF matrix. (b) Photographs of matrix-assisted 3D printing a petroleum jelly ink in an Hphob-CNF matrix.

4.7.1. Evaluation of hydrophobicity of MTMS treated CNF.

Because the Hphil-CNF film is strongly hydrophilic, it was necessary to modify the CNF surface to hydrophobic for controlled diffusion of water at the desired site. For hydrophobic modification of CNF, MTMS was added to a 1 % CNF suspension solution at 0.2, 0.5, and 1.0 % and reacted at 80 °C for 1 h. FT-IR analysis identified the existence of CNF with MTMS (Figure 46a). The stretching vibration of Si-CH$_3$ appeared sharper at 1280 cm^{-1} with an increase in MTMS content, to which it was assigned. CO stretching mixed with a weak contribution of Si-O stretching was observed at 900 cm^{-1}. The stretching vibration of Si-C and the rocking vibration of -CH$_3$ appeared at 780 cm^{-1}, inferring the interaction between MTMS and CNF. The presence of Si−O−cellulose formed by the condensation reaction between the hydroxyl groups of MTMS and the hydroxyl groups of the CNF surface was hard to determine with FTIR spectra because of the masking by intense and wide C−O−C vibration bands of cellulose at 1170-1050 cm^{-1}. The typical vibrations of Si−O−cellulose were assigned at 1150 cm^{-1}, and the development of a shoulder could be observed at the same wavenumber [191]. As the MTMS concentration increased, the vibration intensity of Si−O−cellulose increased, confirming the chemical bonding between MTMS and CNF. The negatively charged CM-CNF was well dispersed in water and formed nanoporous structures after dehydration (Figure 46b). Its high hydrophilicity and water meniscus allowed water absorption and diffusion through the film. The hydrophilicity needed to be controlled in the non-diffusive region, and the water absorption of the CNF films tremendously decreased by MTMS treatment. Significantly, treatment with 1.0% MTMS showed the lowest water swelling ratio of 23.8 %, preventing water penetration into the film (Figure 46c). The transparency of the cell culture platform ensured rapid and real-time observation of cell morphology, attachment, and proliferation. The treated CNF had transparency over 70% in

the entire visible range of light, and the transparency was recovered by contact with water due to suppression of light scattering at the particle edge (Figure 46d). The transparency of the Hphob-CNF Film modified with 1.0 % MTMS was confirmed by showing letter at the background enough to be read (Figure 46e). This system was suitable for real-time observation of features including cell morphology, attachment, and movement on the substrate.
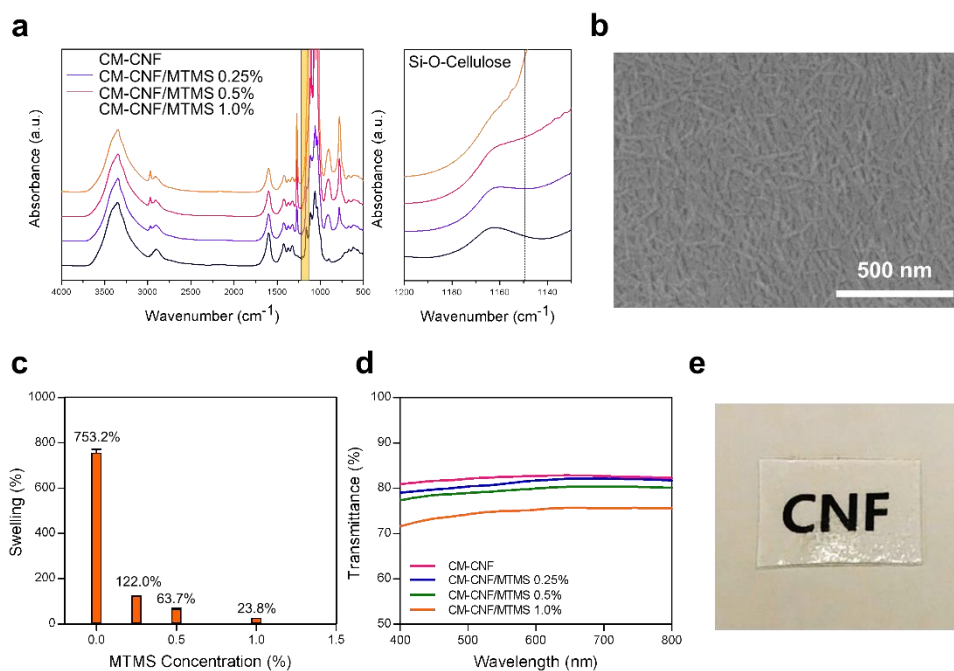
Figure 46. Modification of Hphil-CNFs into Hphob-CNFs. (a) FT-IR spectra and (b) FE-SEM image of MTMS-CNF film. (c) The swelling ratio of CNF films according to MTMS reaction concentration. (d) Transparency of CNF films according to MTMS reaction concentration. (e) Photograph of a transparent Hphob-CNF Film modified with 1.0 % MTMS.

4.7.2. Diffusion of FITC-Dex to CNF channel layers.

The selective diffusion of biomolecules in the CNF-based microfluidic devices was investigated with FITC-Dex having a molecular weight of 4, 70, and 150 kDa (Figure 47a). The model molecules of 5 mg/ml flowed in the channel at a rate of 1 ml/h. Time-lapse fluorescence microscopy demonstrated that 4 kDa of FITC-Dex was not diffusible in the Hphob-CNF region (Figure 47b). In contrast, diffusion of FITC-Dex was observed in the region of Hphil-CNF, and gradual distribution of fluorescent intensity was monitored along the distance from the channel wall (Figure 47c). Furthermore, the fluorescence intensity was measured at 5 min intervals for 1 h, and FITC-Dex having a molecular weight of 4 kDa gradually diffused to a distance exceeding 1000 μm (Figure 47d-47f). In contrast, FITC-Dex with a large molecular weight of 70 or 150 kDa showed a 50 % reduction in intensity compared with 4kDa FITC-Dex (Figure 47f). Spatiotemporal diffusion of molecules through the flow channels provides a cell-friendly experimental tool in the investigation of cell response in an open cell culture environment rather than in closed or confined conditions [190].
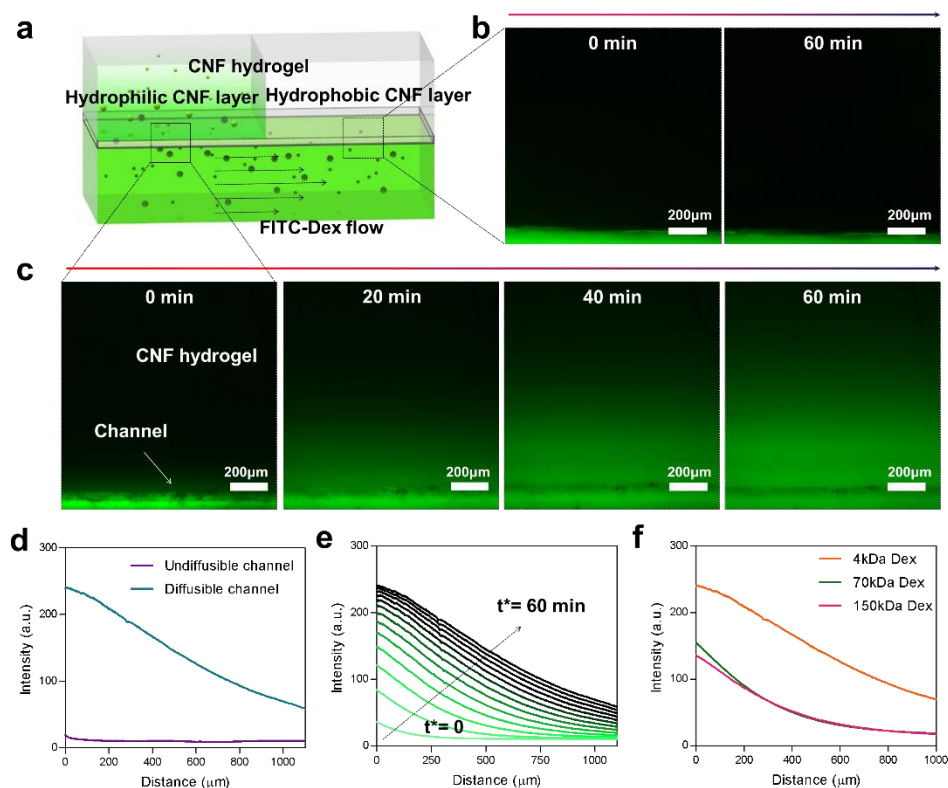
Figure 47. Selective diffusion of molecules in the platform. (a) Schematic illustration of the difference in diffusion tendency at the Hphil-CNF and Hphob-CNF layers in the device. Time-lapse fluorescence microscopic images of 4kDa FITC-Dex flowing in the channel at the (b) Hphob-CNF layer and (c) Hphil-CNF layer. (d) Difference of diffusion tendency between Hphob-CNF and Hphil-CNF layered channels. (e) Change in fluorescence intensity according to distance from the channel surface and diffusion time. 4kDa FITC-Dex was used, and the intensity was measured according to distance from the CNF layered channel at intervals of 5 min. (f) Variation of diffusion tendency according to the size of FITC-Dex molecules.

4.7.3. Cell viability of the CNF-based platform.

In particular, the CNF-based platform is a tool to observe cell response or morphological change caused by diffusion of molecules, including drugs or chemicals, through the channel below the incubation surface. Figure 48a shows a CNF-based cell culture platform whose surface was incubated with fibroblast cells. Cells were seeded at the Hphob-CNF and Hphil-CNF regions and filled the surface as well as on the culture dish. The morphology of cultured cells was observable with an optical microscope because the CNF-based microfluidic device was highly transparent. Despite the confluent growth of cells at the surface, fluidic channels were seen below the surface, confirming chemical flow and cell response (Figure 48b). The Hphob-CNF and Hphil-CNF surfaces showed high cell viability in a live/dead assay (Figure 48c, d). Besides, the relative metabolic activity of cells showed continuous proliferation without a significant difference in cell growth rate between Hphil-CNF and Hphob-CNF (Figure 48e).
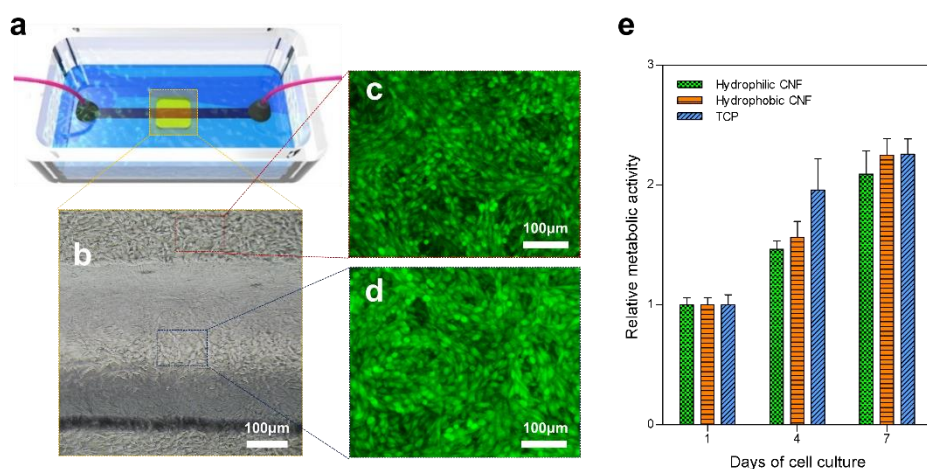
Figure 48. Cell viability of the CNF-based open culture microfluidic platform. (a) A schematic diagram of cell culture with the platform embedding a single-channel structure. (b) Optical microscopic image of the platform cultured with fibroblast cells. Fluorescence images of live and dead assays of fibroblast cells cultured at the Hphob-CNF surface (c) and the Hphil-CNF surface (d). (e) Changes in relative metabolic activity of fibroblast cells in Hphob-CNF, Hphil-CNF, and tissue culture. Metabolic activity was measured with Alamar Blue assay after the cells were cultured for 1, 4, and 7 d.

117

4.7.4. Effect of cisplatin at the CNF-based platform.

The feasibility of the platform for a biomedical cell assay was investigated by inducing diffusion of anticancer molecules to the cell culture and evaluating the effect of drug dose on cell death (Figure 49a). Cisplatin shows specific activity against lung cancer, so it was selected as a model drug for evaluation of the biosensing capability with the CNF-based open culture platform [192]. Lung cancer A549 cells were incubated on the cell culture platform for 3 days, and different concentrations of cisplatin were injected into the channel at a rate of 0.5 ml/h. The Hphob-CNF region was water repellent, and the cisplatin could not diffuse to the cell layer in the same region. A549 cells attached to the Hphob-CNF layer grew well after injection of 100 μM cisplatin because molecular diffusion was prevented through the Hphob-CNF layer (Figure 49b). In contrast, cisplatin diffused to the cell layer in the diffusible region of the Hphil-CNF patterns and affected cell survival (Figures 49c, d). Cell proliferation was decreased dramatically with increased concentration of injected cisplatin, and the IC_{50} of A549 for cisplatin was determined to be 98.91 μM using the open culture CNF microfluidic device (Figure 49e).

The IC_{50} of A549 cells was reported as 23.6 μM when the cells treated with cisplatin solution directly in 2D culture [193]. However, the larger value of IC50 was measured with open culture CNF microfluidic devices. Two possibilities could be considered for the results. First, treatment with cisplatin in 2D cultures might be more effective compared with the diffusion-based CNF microfluidic devices because the cells took the drugs directly. Secondly, carboxymethylated CNFs reduced cisplatin delivered to cells due to the binding of cisplatin to carboxylic groups [194, 195].

Cell growth in a closed or highly integrated culture system induces undesirable effects on the supply of nutrients or critical factors in addition to the complicated design of biochips. The open cell culture system provides

advantages in the investigation of macroscale-cell response to chemicals. The typical protocol for cell culture is applicable without specific control parameters for microenvironments. Control of cell density and surface modification were also efficiently planned with this system.
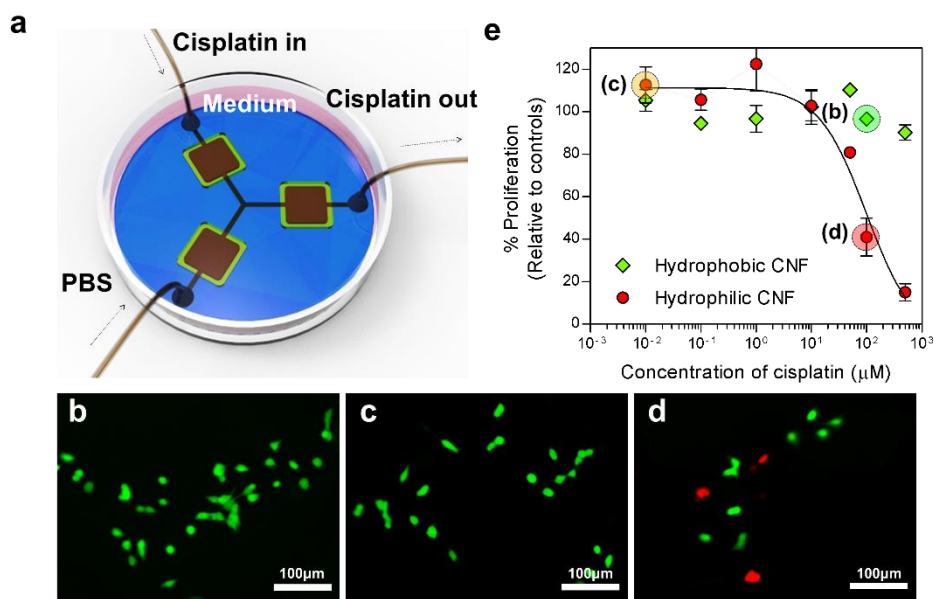
Figure 49. Effect of cisplatin on the viability of cells cultured at the surface of the platform. (a) A schematic diagram of a CNF-based microfluidic device for evaluation of cell proliferation rate of A549 cells. (b) Live/dead assay with A549 cells attached at the surface of the Hphob-CNF layer after 100 μM cisplatin solution was flowed in the channel. Live/dead assay with A549 cells attached at the surface of the Hphil-CNF layer after 0.01 μM (c) and 100 μM (d) cisplatin solutions flowed in the channel. (e) Change in the proliferation rate of A549 cells with a concentration of cisplatin solution in the channel.

V. Conclusion

CNF is an ideal material for forming a hydrogel with suitable viscoelastic properties in 3D printing. CNF hydrogels were suggested as a 3D-structuring ultrathin film and a supporting matrix for 3D microchannels. The optimal combination of rheological properties between the CNF matrix and model inks enabled well-resolved 3D printing, and dehydration from the CNF hydrogel created an ultrathin film containing 3D structures. The infilled inks were easily removed, and the selective coating of the inner channel surfaces was thus available. With the above-described features, a variety of complex structures can be 3D printed in CNF hydrogels and designed for sensing platforms on a microfluidic basis.

The criteria for evaluating printing fidelity in CNF matrix was presented. Firstly, the sharpness of the angle was presented by printing the angled lines. By comparing the yield stresses of the CNF matrix and the model ink under the constant injection pressure and printing speed, it was possible to predict the CNF matrix condition with excellent printing fidelity. The second criterion was whether the cross-sectional shape of the ink was near-circular. This was closely related to the recovery of crevasses formed when the nozzle moved inside the matrix. If the yield stress of the matrix was large, the matrix maintained its shapes against the hydrostatic pressure caused by gravity. This made the cross-sectional shape of the ink close to elliptical. The last criterion was the surface roughness of the printed ink. A more linear feature was shown in the homogeneous CNF matrix. Based on these criteria, the CNF matrix with the carboxylic acid content of 1.14 mmol/g and the concentration of 0.75 % to 1.0 % were most suitable conditions for high print fidelity. The transparency was high enough to observe the 3D printed structure. The PIV experiment was useful in analyzing the flow field of the CNF matrix around the nozzle moving inside the matrix. The disturbing area around the nozzles

affected the printing fidelity when drawing multiple lines. As the yield stress of the CNF matrix increased, the size of the disturbing area decreased and the print fidelity increased.

It was possible to fabricate a thin and transparent CNF-based microfluidic devices capable of flowing the fluid inside. Thus, 3D printing of CNF hydrogels solves critical issues in PDMS-based microfluidic devices such as flexibility and compactness. In addition, it overcomes the limitation in sample migration of wicking paper-based sensing platforms. This greater freedom in regional selectivity will broaden the potential application of 3D patterning in CNF hydrogels to novel areas. In addition, the CNF-based devices were used for the chemical sensor, and cell culture platform due to the numerous nanopores on the CNF film enabling the mass transfer. The high optical transparency of the platform enabled direct observation of flow in the channels, and the spatiotemporal motion of living cells cultured at the CNF surfaces was observed.

The significance of this study could be summarized as follows. First, the CNF, a novel matrix material with high printing fidelity was proposed. Second, the new criteria to quantify the printing fidelity was proposed. Using these criteria, it was easy to identify the printing fidelity, even with other matrix and ink materials. Finally, CNF hydrogels could be fabricated to the thin devices as well as 3D printing matrices.

VI. References

[1] W. Wu, A. DeConinck and J. A. Lewis, Omnidirectional printing of 3D microvascular networks. *Advacned Materials*, **2011**, 23, (24), H178-H183.

[2] D. B. Kolesky, R. L. Truby, A. S. Gladman, T. A. Busbee, K. A. Homan and J. A. Lewis, 3D bioprinting of vascularized, heterogeneous cell-laden tissue constructs. *Advacned Materials*, **2014**, 26, (19), 3124-3130.

[3] J. T. Muth, D. M. Vogt, R. L. Truby, Y. Menguc, D. B. Kolesky, R. J. Wood and J. A. Lewis, Embedded 3D Printing of Strain Sensors within Highly Stretchable Elastomers. *Advacned Materials*, **2014**, 26, (36), 6307-6312.

[4] D. P. Parekh, C. Ladd, L. Panich, K. Moussa and M. D. Dickey, 3D printing of liquid metals as fugitive inks for fabrication of 3D microfluidic channels. *Lab on a Chip*, **2016**, 16, (10), 1812-1820.

[5] C. B. Highley, C. B. Rodell and J. A. Burdick, Direct 3D Printing of Shear-Thinning Hydrogels into Self-Healing Hydrogels. *Advacned Materials*, **2015**, 27, (34), 5075-+.

[6] T. Bhattacharjee, S. M. Zehnder, K. G. Rowe, S. Jain, R. M. Nixon, W. G. Sawyer and T. E. Angelini, Writing in the granular gel medium. *Science Advances*, **2015**, 1, (8), e1500655.

[7] Y. Habibi, L. A. Lucia and O. J. Rojas, Cellulose Nanocrystals: Chemistry, Self-Assembly, and Applications. *Chemical Reviews*, **2010**, 110, (6), 3479-3500.

[8] J. F. Beecher, Wood, trees and nanotechnology. *Nature Nanotechnology*, **2007**, 2, (8), 466-467.

[9] M. Nogi, S. Iwamoto, A. N. Nakagaito and H. Yano, Optically transparent nanofiber paper. *Advanced Materials*, **2009**, 21, (16), 1595-1598.

[10] H. Koga, M. Nogi, N. Komoda, T. T. Nge, T. Sugahara and K. Suganuma, Uniformly connected conductive networks on cellulose nanofiber paper for transparent paper electronics. *Npg Asia Materials*, **2014**, 6.

[11] Y. Fujisaki, H. Koga, Y. Nakajima, M. Nakata, H. Tsuji, T. Yamamoto, T. Kurita, M. Nogi and N. Shimidzu, Transparent Nanopaper-Based Flexible Organic Thin-Film Transistor Array. *Advanced Functional Materials*, **2014**, 24, (12), 1657-1663.

[12] A. Isogai, T. Saito and H. Fukuzumi, TEMPO-oxidized cellulose nanofibers. *Nanoscale*, **2011**, 3, (1), 71-85.

[13] M. Ghaderi, M. Mousavi, H. Yousefi and M. Labbafi, All-cellulose nanocomposite film made from bagasse cellulose nanofibers for food packaging application. *Carbohydrate Polymers*, **2014**, 104, 59-65.

[14] R. M. A. Domingues, S. Chiera, P. Gershovich, A. Motta, R. L. Reis and M. E. Gomes, Enhancing the Biomechanical Performance of Anisotropic Nanofibrous Scaffolds in Tendon Tissue Engineering: Reinforcement with Cellulose Nanocrystals. *Advanced Healthcare Materials*, **2016**, 5, (11), 1364-1375.

[15] C. J. Zhou, Q. F. Shi, W. H. Guo, L. Terrell, A. T. Qureshi, D. J. Hayes and Q. L. Wu, Electrospun Bio-Nanocomposite Scaffolds for Bone Tissue Engineering by Cellulose Nanocrystals Reinforcing Maleic Anhydride Grafted PLA. *ACS Applied Materials and Interfaces*, **2013**, 5, (9), 3847-3854.

[16] X. He, Q. Xiao, C. H. Lu, Y. R. Wang, X. F. Zhang, J. Q. Zhao, W. Zhang, X. M. Zhang and Y. L. Deng, Uniaxially Aligned Electrospun All-Cellulose

Nanocomposite Nanofibers Reinforced with Cellulose Nanocrystals: Scaffold for Tissue Engineering. *Biomacromolecules*, **2014**, 15, (2), 618-627.

[17] R. T. Olsson, M. A. S. A. Samir, G. Salazar-Alvarez, L. Belova, V. Strom, L. A. Berglund, O. Ikkala, J. Nogues and U. W. Gedde, Making flexible magnetic aerogels and stiff magnetic nanopaper using cellulose nanofibrils as templates. *Nature Nanotechnology*, **2010**, 5, (8), 584-588.

[18] M. Wang, I. V. Anoshkin, A. G. Nasibulin, J. T. Korhonen, J. Seitsonen, J. Pere, E. I. Kauppinen, R. H. A. Ras and O. Ikkala, Modifying Native Nanocellulose Aerogels with Carbon Nanotubes for Mechanoresponsive Conductivity and Pressure Sensing. *Advanced Materials*, **2013**, 25, (17), 2428-2432.

[19] Z. Q. Shi, H. C. Gao, J. Feng, B. B. Ding, X. D. Cao, S. Kuga, Y. J. Wang, L. N. Zhang and J. Cai, In Situ Synthesis of Robust Conductive Cellulose/Polypyrrole Composite Aerogels and Their Potential Application in Nerve Regeneration. *Angewandte Chemie International Edition*, **2014**, 53, (21), 5380-5384.

[20] B. Wang, X. L. Li, B. Luo, J. X. Yang, X. J. Wang, Q. Song, S. Y. Chen and L. J. Zhi, Pyrolyzed Bacterial Cellulose: A Versatile Support for Lithium Ion Battery Anode Materials. *Small*, **2013**, 9, (14), 2399-2404.

[21] G. Nystrom, A. Razaq, M. Stromme, L. Nyholm and A. Mihranyan, Ultrafast All-Polymer Paper-Based Batteries. *Nano Letters*, **2009**, 9, (10), 3635-3639.

[22] L. F. Chen, Z. H. Huang, H. W. Liang, Q. F. Guan and S. H. Yu, Bacterial-Cellulose-Derived Carbon Nanofiber@MnO2 and Nitrogen-Doped Carbon Nanofiber Electrode Materials: An Asymmetric Supercapacitor with High Energy and Power Density. *Advanced Materials*, **2013**, 25, (34), 4746-4752.

[23] G. Siqueira, D. Kokkinis, R. Libanori, M. K. Hausmann, A. S. Gladman, A. Neels, P. Tingaut, T. Zimmermann, J. A. Lewis and A. R. Studart, Cellulose Nanocrystal Inks for 3D Printing of Textured Cellular Architectures. *Advanced Functional Materials*, **2017**, 27, (12).

[24] K. Markstedt, A. Mantas, I. Tournier, H. M. Avila, D. Hagg and P. Gatenholm, 3D Bioprinting Human Chondrocytes with Nanocellulose-Alginate Bioink for Cartilage Tissue Engineering Applications. *Biomacromolecules*, **2015**, 16, (5), 1489-1496.

[25] A. S. Gladman, E. A. Matsumoto, R. G. Nuzzo, L. Mahadevan and J. A. Lewis, Biomimetic 4D printing. *Nature Materials*, **2016**, 15, (4), 413-+.

[26] J. G. Torres-Rendon, T. Femmer, L. De Laporte, T. Tigges, K. Rahimi, F. Gremse, S. Zafarnia, W. Lederle, S. Ifuku, M. Wessling, J. G. Hardy and A. Walther, Bioactive Gyroid Scaffolds Formed by Sacrificial Templating of Nanocellulose and Nanochitin Hydrogels as Instructive Platforms for Biomimetic Tissue Engineering. *Advanced Materials*, **2015**, 27, (19), 2989-2995.

[27] X. Li, D. R. Ballerini and W. Shen, A perspective on paper-based microfluidics: Current status and future trends. *Biomicrofluidics*, **2012**, 6, (1).

[28] A. C. Glavan, R. V. Martinez, E. J. Maxwell, A. B. Subramaniam, R. M. D. Nunes, S. Soh and G. M. Whitesides, Rapid fabrication of pressure-driven open-channel microfluidic devices in omniphobic R-F paper. *Lab on a Chip*, **2013**, 13, (15), 2922-2930.

[29] M. M. Thuo, R. V. Martinez, W. J. Lan, X. Y. Liu, J. Barber, M. B. J. Atkinson, D. Bandarage, J. F. Bloch and G. M. Whitesides, Fabrication of Low-Cost Paper-Based Microfluidic Devices by Embossing or Cut-and-Stack Methods. *Chemistry of Materials*, **2014**, 26, (14), 4230-4237.

[30] M. M. Hamedi, B. Unal, E. Kerr, A. C. Glavan, M. T. Fernandez-Abedul and G. M. Whitesides, Coated and uncoated cellophane as materials for microplates and open-channel microfluidics devices. *Lab on a Chip*, **2016**, 16, (20), 3885-3897.

[31] S. V. Murphy and A. Atala, 3D bioprinting of tissues and organs. *Nature Biotechnology*, **2014**, 32, (8), 773-785.

[32] P. F. Jacobs, *Rapid prototyping & manufacturing: fundamentals of stereolithography*. Society of Manufacturing Engineers: 1992.

[33] F. P. Melchels, J. Feijen and D. W. Grijpma, A review on stereolithography and its applications in biomedical engineering. *Biomaterials*, **2010**, 31, (24), 6121-6130.

[34] C. W. Hull, Apparatus for production of three-dimensional objects by stereolithography. In US Patents: 1986.

[35] H. Kodama, Automatic method for fabricating a three-dimensional plastic model with photo-hardening polymer. *Review of Scientific Instruments*, **1981**, 52, (11), 1770-1773.

[36] E. M. Sachs, J. S. Haggerty, M. J. Cima and P. A. Williams, Three-dimensional printing techniques. In US Patents: 1993.

[37] D. K. Patel, A. H. Sakhaei, M. Layani, B. Zhang, Q. Ge and S. Magdassi, Highly stretchable and UV curable elastomers for digital light processing based 3D printing. *Advanced Materials*, **2017**, 29, (15), 1606000.

[38] S. H. Kim, Y. K. Yeon, J. M. Lee, J. R. Chao, Y. J. Lee, Y. B. Seo, M. T. Sultan, O. J. Lee, J. S. Lee and S.-i. Yoon, Precisely printable and biocompatible silk fibroin bioink for digital light processing 3D printing. *Nature Communications*, **2018**, 9, (1), 1620.

[39] Y. Lu, G. Mapili, G. Suhali, S. Chen and K. Roy, A digital micro-mirror device-based system for the microfabrication of complex, spatially patterned tissue engineering scaffolds. *Journal of Biomedical Materials Research Part A*, **2006**, 77, (2), 396-405.

[40] J. M. Florence, W. E. Nelson, V. Venkateswar, J. S. Clair, D. Broddin and S. M. Tavernier, Process and architecture for digital micromirror printer. In US Patents: 1995.

[41] J. R. Tumbleston, D. Shirvanyants, N. Ermoshkin, R. Janusziewicz, A. R. Johnson, D. Kelly, K. Chen, R. Pinschmidt, J. P. Rolland and A. Ermoshkin, Continuous liquid interface production of 3D objects. *Science*, **2015**, 347, (6228), 1349-1352.

[42] R. Janusziewicz, J. R. Tumbleston, A. L. Quintanilla, S. J. Mecham and J. M. DeSimone, Layerless fabrication with continuous liquid interface production. *Proceedings of the National Academy of Sciences*, **2016**, 113, (42), 11703-11708.

[43] B. H. Cumpston, S. P. Ananthavel, S. Barlow, D. L. Dyer, J. E. Ehrlich, L. L. Erskine, A. A. Heikal, S. M. Kuebler, I.-Y. S. Lee and D. McCord-Maughon, Two-photon polymerization initiators for three-dimensional optical data storage and microfabrication. *Nature*, **1999**, 398, (6722), 51.

[44] A. Ovsianikov, J. Viertl, B. Chichkov, M. Oubaha, B. MacCraith, I. Sakellari, A. Giakoumaki, D. Gray, M. Vamvakaki and M. Farsari, Ultra-low shrinkage hybrid photosensitive material for two-photon polymerization microfabrication. *ACS Nano*, **2008**, 2, (11), 2257-2262.

[45] P. Tayalia, C. R. Mendonca, T. Baldacchini, D. J. Mooney and E. Mazur, 3D cell-migration studies using two-photon engineered polymer scaffolds. *Advanced Materials*, **2008**, 20, (23), 4494-4498.

[46] J.-P. Kruth, P. Mercelis, J. Van Vaerenbergh, L. Froyen and M. Rombouts, Binding mechanisms in selective laser sintering and selective laser melting. *Rapid Prototyping Journal*, **2005**, 11, (1), 26-36.

[47] J. M. Williams, A. Adewunmi, R. M. Schek, C. L. Flanagan, P. H. Krebsbach, S. E. Feinberg, S. J. Hollister and S. Das, Bone tissue engineering using polycaprolactone scaffolds fabricated via selective laser sintering. *Biomaterials*, **2005**, 26, (23), 4817-4827.

[48] P. Mercelis and J.-P. Kruth, Residual stresses in selective laser sintering and selective laser melting. *Rapid Prototyping Journal*, **2006**, 12, (5), 254-265.

[49] K. Tan, C. Chua, K. Leong, C. Cheah, P. Cheang, M. A. Bakar and S. Cha, Scaffold development using selective laser sintering of polyetheretherketone–hydroxyapatite biocomposite blends. *Biomaterials*, **2003**, 24, (18), 3115-3123.

[50] J. J. Beaman and C. R. Deckard, Selective laser sintering with assisted powder handling. In US Patents: 1990.

[51] I. Zein, D. W. Hutmacher, K. C. Tan and S. H. Teoh, Fused deposition modeling of novel scaffold architectures for tissue engineering applications. *Biomaterials*, **2002**, 23, (4), 1169-1185.

[52] S.-H. Ahn, M. Montero, D. Odell, S. Roundy and P. K. Wright, Anisotropic material properties of fused deposition modeling ABS. *Rapid Prototyping Journal*, **2002**, 8, (4), 248-257.

[53] S. S. Crump, J. W. Comb, W. R. Priedeman Jr and R. L. Zinniel, Process of support removal for fused deposition modeling. In US Patents: 1996.

[54] O. A. Mohamed, S. H. Masood and J. L. Bhowmik, Optimization of fused deposition modeling process parameters: a review of current research and future prospects. *Advances in Manufacturing*, **2015**, 3, (1), 42-53.

[55] M. F. Afrose, S. Masood, P. Iovenitti, M. Nikzad and I. Sbarski, Effects of part build orientations on fatigue behaviour of FDM-processed PLA material. *Progress in Additive Manufacturing*, **2016**, 1, (1-2), 21-28.

[56] D. Drummer, S. Cifuentes-Cuéllar and D. Rietzel, Suitability of PLA/TCP for fused deposition modeling. *Rapid Prototyping Journal*, **2012**, 18, (6), 500-507.

[57] M. A. Cuiffo, J. Snyder, A. M. Elliott, N. Romero, S. Kannan and G. P. Halada, Impact of the fused deposition (FDM) printing process on polylactic acid (PLA) chemistry and structure. *Applied Sciences*, **2017**, 7, (6), 579.

[58] J. Holländer, N. Genina, H. Jukarainen, M. Khajeheian, A. Rosling, E. Mäkilä and N. Sandler, Three-dimensional printed PCL-based implantable prototypes of medical devices for controlled drug delivery. *Journal of Pharmaceutical Sciences*, **2016**, 105, (9), 2665-2676.

[59] J. Dávila, M. S. d. Freitas, P. Inforçatti Neto, Z. d. C. Silveira, J. V. L. d. Silva and M. A. d'Ávila, Fabrication of PCL/β-TCP scaffolds by 3D mini-screw extrusion printing. *Journal of Applied Polymer Science*, **2016**, 133, (15).

[60] N. Genina, J. Holländer, H. Jukarainen, E. Mäkilä, J. Salonen and N. Sandler, Ethylene vinyl acetate (EVA) as a new drug carrier for 3D printed medical drug delivery devices. *European Journal of Pharmaceutical Sciences*, **2016**, 90, 53-63.

[61] N. Kumar, P. K. Jain, P. Tandon and P. M. Pandey, The effect of process parameters on tensile behavior of 3D printed flexible parts of ethylene vinyl acetate (EVA). *Journal of Manufacturing Processes*, **2018**, 35, 317-326.

[62] M. Dawoud, I. Taha and S. J. Ebeid, Mechanical behaviour of ABS: An experimental study using FDM and injection moulding techniques. *Journal of Manufacturing Processes*, **2016**, 21, 39-45.

[63] M. Montero, S. Roundy, D. Odell, S.-H. Ahn and P. K. Wright, Material characterization of fused deposition modeling (FDM) ABS by designed experiments. *Society of Manufacturing Engineers*, **2001**, 10, (13552540210441166).

[64] J. A. Lewis, Direct ink writing of 3D functional materials. *Advanced Functional Materials*, **2006**, 16, (17), 2193-2204.

[65] J. A. Lewis, J. E. Smay, J. Stuecker and J. Cesarano, Direct ink writing of three-dimensional ceramic structures. *Journal of the American Ceramic Society*, **2006**, 89, (12), 3599-3609.

[66] J. A. Lewis and G. M. Gratson, Direct writing in three dimensions. *Materials Today*, **2004**, 7, (7-8), 32-39.

[67] R. A. Barry III, R. F. Shepherd, J. N. Hanson, R. G. Nuzzo, P. Wiltzius and J. A. Lewis, Direct-write assembly of 3D hydrogel scaffolds for guided cell growth. *Advanced Materials*, **2009**, 21, (23), 2407-2410.

[68] S. Ghosh, S. T. Parker, X. Wang, D. L. Kaplan and J. A. Lewis, Direct-write assembly of microperiodic silk fibroin scaffolds for tissue engineering applications. *Advanced Functional Materials*, **2008**, 18, (13), 1883-1889.

[69] G. M. Gratson, M. Xu and J. A. Lewis, Microperiodic structures: Direct writing of three-dimensional webs. *Nature*, **2004**, 428, (6981), 386.

[70] C. B. Highley, C. B. Rodell and J. A. Burdick, Direct 3D printing of shear-thinning hydrogels into self-healing hydrogels. *Advanced Materials*, **2015**, 27, (34), 5075-5079.

[71] L. Ouyang, C. B. Highley, C. B. Rodell, W. Sun and J. A. Burdick, 3D printing of shear-thinning hyaluronic acid hydrogels with secondary cross-linking. *ACS Biomaterials Science Engineering*, **2016**, 2, (10), 1743-1751.

[72] C. Loebel, C. B. Rodell, M. H. Chen and J. A. Burdick, Shear-thinning and self-healing hydrogels as injectable therapeutics and for 3D-printing. *Nature Protocols*, **2017**, 12, (8), 1521.

[73] S. A. Wilson, L. M. Cross, C. W. Peak and A. K. Gaharwar, Shear-thinning and thermo-reversible nanoengineered inks for 3D bioprinting. *ACS Applied Materials & Interfaces*, **2017**, 9, (50), 43449-43458.

[74] W. Liu, M. A. Heinrich, Y. Zhou, A. Akpek, N. Hu, X. Liu, X. Guan, Z. Zhong, X. Jin and A. Khademhosseini, Extrusion bioprinting of shear-thinning gelatin methacryloyl bioinks. *Advanced Healthcare Materials*, **2017**, 6, (12), 1601451.

[75] D. Kokkinis, M. Schaffner and A. R. Studart, Multimaterial magnetically assisted 3D printing of composite materials. *Nature Communications*, **2015**, 6, 8643.

[76] J. Kopeček, Hydrogel biomaterials: a smart future? *Biomaterials*, **2007**, 28, (34), 5185-5192.

[77] K. T. Nguyen and J. L. West, Photopolymerizable hydrogels for tissue engineering applications. *Biomaterials*, **2002**, 23, (22), 4307-4314.

[78] M. P. Lutolf, Biomaterials: Spotlight on hydrogels. *Nature Materials*, **2009**, 8, (6), 451.

[79] X. Z. Shu, Y. Liu, F. S. Palumbo, Y. Luo and G. D. Prestwich, In situ crosslinkable hyaluronan hydrogels for tissue engineering. *Biomaterials*, **2004**, 25, (7-8), 1339-1348.

[80] V. Mironov, N. Reis and B. Derby, Bioprinting: A beginning. *Tissue Engineering*, **2006**, 12, (4), 631-634.

[81] C. Norotte, F. S. Marga, L. E. Niklason and G. Forgacs, Scaffold-free vascular tissue engineering using bioprinting. *Biomaterials*, **2009**, 30, (30), 5910-5917.

[82] D. B. Kolesky, R. L. Truby, A. S. Gladman, T. A. Busbee, K. A. Homan and J. A. Lewis, 3D bioprinting of vascularized, heterogeneous cell-laden tissue constructs. *Advanced Materials*, **2014**, 26, (19), 3124-3130.

[83] R. L. Truby and J. A. Lewis, Printing soft matter in three dimensions. *Nature*, **2016**, 540, (7633), 371-378.

[84] T. Bhattacharjee, S. M. Zehnder, K. G. Rowe, S. Jain, R. M. Nixon, W. G. Sawyer and T. E. Angelini, Writing in the granular gel medium. *Science Advances*, **2015**, 1, (8).

[85] R. L. Truby, M. Wehner, A. K. Grosskopf, D. M. Vogt, S. G. Uzel, R. J. Wood and J. A. Lewis, Soft somatosensitive actuators via embedded 3D printing. *Advanced Materials*, **2018**, 30, (15), 1706383.

[86] M. Wehner, R. L. Truby, D. J. Fitzgerald, B. Mosadegh, G. M. Whitesides, J. A. Lewis and R. J. Wood, An integrated design and fabrication strategy for entirely soft, autonomous robots. *Nature*, **2016**, 536, (7617), 451.

[87] J. T. Muth, D. M. Vogt, R. L. Truby, Y. Mengüç, D. B. Kolesky, R. J. Wood and J. A. Lewis, Embedded 3D printing of strain sensors within highly stretchable elastomers. *Advanced Materials*, **2014**, 26, (36), 6307-6312.

[88] J. J. Escobar-Chávez, M. López-Cervantes, A. Naik, Y. Kalia, D. Quintanar-Guerrero and A. Ganem-Quintanar, Applications of thermo-reversible pluronic F-127 gels in pharmaceutical formulations. *Journal of Pharmacy & Pharmaceutical Sciences*, **2006**, 9, (3), 339-58.

[89] V. Lenaerts, C. Triqueneaux, M. Quartern, F. Rieg-Falson and P. Couvreur, Temperature-dependent rheological behavior of Pluronic F-127 aqueous solutions. *International Journal of Pharmaceutics*, **1987**, 39, (1-2), 121-127.

[90] M. Bohorquez, C. Koch, T. Trygstad and N. Pandit, A study of the temperature-dependent micellization of pluronic F127. *Journal of Colloid Interface Science*, **1999**, 216, (1), 34-40.

[91] T. J. Hinton, Q. Jallerat, R. N. Palchesko, J. H. Park, M. S. Grodzicki, H.-J. Shue, M. H. Ramadan, A. R. Hudson and A. W. Feinberg, Three-dimensional printing of complex biological structures by freeform reversible embedding of suspended hydrogels. *Science Advances*, **2015**, 1, (9), e1500758.

[92] M. W. Toepke and D. J. Beebe, PDMS absorption of small molecules and consequences in microfluidic applications. *Lab on a Chip*, **2006**, 6, (12), 1484-1486.

[93] T. Fujii, PDMS-based microfluidic devices for biomedical applications. *Microelectronic Engineering*, **2002**, 61, 907-914.

[94] J. R. Anderson, D. T. Chiu, R. J. Jackman, O. Cherniavskaya, J. C. McDonald, H. Wu, S. H. Whitesides and G. M. Whitesides, Fabrication of topologically complex three-dimensional microfluidic systems in PDMS by rapid prototyping. *Analytical Chemistry*, **2000**, 72, (14), 3158-3164.

[95] C. S. O'Bryan, T. Bhattacharjee, S. Hart, C. P. Kabb, K. D. Schulze, I. Chilakala, B. S. Sumerlin, W. G. Sawyer and T. E. Angelini, Self-assembled micro-organogels for 3D printing silicone structures. *Science Advances*, **2017**, 3, (5).

[96] A. K. Grosskopf, R. L. Truby, H. Kim, A. Perazzo, J. A. Lewis and H. A. Stone, Viscoplastic matrix materials for embedded 3D printing. *ACS Applied Materials & Interfaces*, **2018**, 10, (27), 23353-23361.

[97] T. H. Wegner and P. E. Jones, Advancing cellulose-based nanotechnology. *Cellulose*, **2006**, 13, (2), 115-118.

[98] D. Klemm, B. Heublein, H. P. Fink and A. Bohn, Cellulose: fascinating biopolymer and sustainable raw material. *Angewandte Chemie*, **2005**, 44, (22), 3358-3393.

[99] D. G. Coffey, D. A. Bell and A. Henderson, *Cellulose and cellulose derivatives*. Marcel Dekker Inc.: New York, NY, USA: 1995; Vol. 5.

[100] P. Handbook, J. Brandrup, EH Immergut and EA Grulke. In Wiley, New York: 1999.

[101] K. L. Spence, R. A. Venditti, O. J. Rojas, Y. Habibi and J. J. Pawlak, A comparative study of energy consumption and physical properties of microfibrillated cellulose produced by different processing methods. *Cellulose*, **2011**, 18, (4), 1097-1111.

[102] A. Tejado, M. N. Alam, M. Antal, H. Yang and T. G. van de Ven, Energy requirements for the disintegration of cellulose fibers into cellulose nanofibers. *Cellulose*, **2012**, 19, (3), 831-842.

[103] B. Walter and J. C. Gallatin, Enzymatic conversion of cellulosic fibers. In US Patents: 1962.

[104] M. Henriksson, G. Henriksson, L. Berglund and T. Lindström, An environmentally friendly method for enzyme-assisted preparation of microfibrillated cellulose (MFC) nanofibers. *European Polymer Journal*, **2007**, 43, (8), 3434-3441.

[105] M. Pääkkö, M. Ankerfors, H. Kosonen, A. Nykänen, S. Ahola, M. Österberg, J. Ruokolainen, J. Laine, P. T. Larsson and O. Ikkala, Enzymatic hydrolysis combined with mechanical shearing and high-pressure homogenization for nanoscale cellulose fibrils and strong gels. *Biomacromolecules*, **2007**, 8, (6), 1934-1941.

[106] J.-P. Joseleau, V. Chevalier-Billosta and K. Ruel, Interaction between microfibrillar cellulose fines and fibers: Influence on pulp qualities and paper sheet properties. *Cellulose*, **2012**, 19, (3), 769-777.

[107] C.-N. Wu, T. Saito, S. Fujisawa, H. Fukuzumi and A. Isogai, Ultrastrong and high gas-barrier nanocellulose/clay-layered composites. *Biomacromolecules*, **2012**, 13, (6), 1927-1932.

[108] N. J. Davis and S. L. Flitsch, Selective oxidation of monosaccharide derivatives to uronic acids. *Tetrahedron Letters*, **1993**, 34, (7), 1181-1184.

[109] T. Heinze and A. Koschella In *Carboxymethyl ethers of cellulose and starch–a review*, Macromolecular Symposia, 2005; Wiley Online Library: 2005; pp 13-40.

[110] M. Iotti, Ø. W. Gregersen, S. Moe and M. Lenes, Rheological studies of microfibrillar cellulose water dispersions. *Journal of Polymers & the Environment*, **2011**, 19, (1), 137-145.

[111] G. Agoda-Tandjawa, S. Durand, S. Berot, C. Blassel, C. Gaillard, C. Garnier and J.-L. Doublier, Rheological characterization of microfibrillated

cellulose suspensions after freezing. *Carbohydrate Polymers*, **2010**, 80, (3), 677-686.

[112] E. Saarikoski, T. Saarinen, J. Salmela and J. Seppälä, Flocculated flow of microfibrillated cellulose water suspensions: an imaging approach for characterisation of rheological behaviour. *Cellulose*, **2012**, 19, (3), 647-659.

[113] O. Nechyporchuk, M. N. Belgacem and F. Pignon, Concentration effect of TEMPO-oxidized nanofibrillated cellulose aqueous suspensions on the flow instabilities and small-angle X-ray scattering structural characterization. *Cellulose*, **2015**, 22, (4), 2197-2210.

[114] M.-P. Lowys, J. Desbrieres and M. Rinaudo, Rheological characterization of cellulosic microfibril suspensions. Role of polymeric additives. *Food Hydrocolloids*, **2001**, 15, (1), 25-32.

[115] E. Lasseuguette, D. Roux and Y. Nishiyama, Rheological properties of microfibrillar suspension of TEMPO-oxidized pulp. *Cellulose*, **2008**, 15, (3), 425-433.

[116] O. Nechyporchuk, M. N. Belgacem and F. Pignon, Rheological properties of micro-/nanofibrillated cellulose suspensions: wall-slip and shear banding phenomena. *Carbohydrate Polymers*, **2014**, 112, 432-439.

[117] G. Siqueira, D. Kokkinis, R. Libanori, M. K. Hausmann, A. S. Gladman, A. Neels, P. Tingaut, T. Zimmermann, J. A. Lewis and A. R. Studart, Cellulose nanocrystal inks for 3D printing of textured cellular architectures. *Advanced Functional Materials*, **2017**, 27, (12), 1604619.

[118] S. Sultan, G. Siqueira, T. Zimmermann and A. P. Mathew, 3D printing of nano-cellulosic biomaterials for medical applications. *Current Opinion in Biomedical Engineering*, **2017**, 2, 29-34.

[119] S. Shin, S. Park, M. Park, E. Jeong, K. Na, H. J. Youn and J. Hyun, Cellulose nanofibers for the enhancement of printability of low viscosity gelatin derivatives. *Bioresources*, **2017**, 12, (2), 2941-2954.

[120] V. C. Li, A. Mulyadi, C. K. Dunn, Y. Deng and H. J. Qi, Direct ink write 3D printed cellulose nanofiber aerogel structures with highly deformable, shape recoverable, and functionalizable properties. *ACS Sustainable Chemistry & Engineering*, **2018**, 6, (2), 2011-2022.

[121] K. Markstedt, A. Escalante, G. Toriz and P. Gatenholm, Biomimetic inks based on cellulose nanofibrils and cross-linkable xylans for 3D printing. *ACS Applied Materials & Interfaces*, **2017**, 9, (46), 40878-40886.

[122] Q. Wang, J. Sun, Q. Yao, C. Ji, J. Liu and Q. Zhu, 3D printing with cellulose materials. *Cellulose*, **2018**, 25, (8), 4275-4301.

[123] Y. Li, H. Zhu, Y. Wang, U. Ray, S. Zhu, J. Dai, C. Chen, K. Fu, S. H. Jang and D. Henderson, Cellulose-nanofiber-enabled 3D printing of a carbon-nanotube microfiber network. *Small Methods*, **2017**, 1, (10), 1700222.

[124] L. Dai, T. Cheng, C. Duan, W. Zhao, W. Zhang, X. Zou, J. Aspler and Y. Ni, 3D printing using plant-derived cellulose and its derivatives: A review. *Carbohydrate Polymers*, **2019**, 203, 71-86.

[125] V. Kuzmenko, E. Karabulut, E. Pernevik, P. Enoksson and P. Gatenholm, Tailor-made conductive inks from cellulose nanofibrils for 3D printing of neural guidelines. *Carbohydrate Polymers*, **2018**, 189, 22-30.

[126] K. Markstedt, A. Mantas, I. Tournier, H. c. Martínez Ávila, D. Hägg and P. Gatenholm, 3D bioprinting human chondrocytes with nanocellulose–alginate bioink for cartilage tissue engineering applications. *Biomacromolecules*, **2015**, 16, (5), 1489-1496.

[127] E. B. Heggset, B. L. Strand, K. W. Sundby, S. Simon, G. Chinga-Carrasco and K. Syverud, Viscoelastic properties of nanocellulose based inks for 3D printing and mechanical properties of CNF/alginate biocomposite gels. *Cellulose*, **2019**, 26, (1), 581-595.

[128] M. Saric-Coric, K. Khayat and A. Tagnit-Hamou, Performance characteristics of cement grouts made with various combinations of high-range water reducer and cellulose-based viscosity modifier. *Cement Concrete Research*, **2003**, 33, (12), 1999-2008.

[129] A. Rees, L. C. Powell, G. Chinga-Carrasco, D. T. Gethin, K. Syverud, K. E. Hill and D. W. Thomas, 3D bioprinting of carboxymethylated-periodate oxidized nanocellulose constructs for wound dressing applications. *BioMed Research International*, **2015**, 2015.

[130] K. Markstedt, J. Sundberg and P. Gatenholm, 3D bioprinting of cellulose structures from an ionic liquid. *3D Printing Additive Manufacturing*, **2014**, 1, (3), 115-121.

[131] A. J. Benítez, F. Lossada, B. Zhu, T. Rudolph and A. Walther, Understanding toughness in bioinspired cellulose nanofibril/polymer nanocomposites. *Biomacromolecules*, **2016**, 17, (7), 2417-2426.

[132] H. Fukuzumi, T. Saito and A. Isogai, Influence of TEMPO-oxidized cellulose nanofibril length on film properties. *Carbohydrate Polymers*, **2013**, 93, (1), 172-177.

[133] A. J. Svagan, M. A. A. Samir and L. A. Berglund, Biomimetic foams of high mechanical performance based on nanostructured cell walls reinforced by native cellulose nanofibrils. *Advanced Materials*, **2008**, 20, (7), 1263-1269.

[134] A. S. Gladman, E. A. Matsumoto, R. G. Nuzzo, L. Mahadevan and J. A. Lewis, Biomimetic 4D printing. *Nature Materials*, **2016**, 15, (4), 413.

[135] J. K. Muiruri, S. Liu, W. S. Teo, J. Kong and C. He, Highly biodegradable and tough polylactic acid–cellulose nanocrystal composite. *ACS Sustainable Chemistry & Engineering*, **2017**, 5, (5), 3929-3937.

[136] J. Dong, M. Li, L. Zhou, S. Lee, C. Mei, X. Xu and Q. Wu, The influence of grafted cellulose nanofibers and postextrusion annealing treatment on selected properties of poly (lactic acid) filaments for 3D printing. *Journal of Polymer Science Part B*, **2017**, 55, (11), 847-855.

[137] J. Wang, D. J. Gardner, N. M. Stark, D. W. Bousfield, M. Tajvidi and Z. Cai, Moisture and oxygen barrier properties of cellulose nanomaterial-based films. *ACS Sustainable Chemistry & Engineering*, **2017**, 6, (1), 49-70.

[138] Y. Tao, H. Wang, Z. Li, P. Li and S. Q. Shi, Development and application of wood flour-filled polylactic acid composite filament for 3D printing. *Materials*, **2017**, 10, (4), 339.

[139] S. W. Pattinson and A. J. Hart, Additive manufacturing of cellulosic materials with robust mechanics and antimicrobial functionality. *Advanced Materials Technologies*, **2017**, 2, (4), 1600084.

[140] K. M. Håkansson, I. C. Henriksson, C. de la Peña Vázquez, V. Kuzmenko, K. Markstedt, P. Enoksson and P. Gatenholm, Solidification of 3D printed nanofibril hydrogels into functional 3D cellulose structures. *Advanced Materials Technologies*, **2016**, 1, (7), 1600096.

[141] S. Huan, R. Ajdary, L. Bai, V. Klar and O. J. Rojas, Low solids emulsion gels based on nanocellulose for 3D-printing. *Biomacromolecules*, **2018**, 20, (2), 635-644.

[142] H. Koga, M. Nogi, N. Komoda, T. T. Nge, T. Sugahara and K. Suganuma, Uniformly connected conductive networks on cellulose nanofiber paper for transparent paper electronics. *NPG Asia Materials*, **2014**, 6, (3), e93.

[143] K. Nagashima, H. Koga, U. Celano, F. Zhuge, M. Kanai, S. Rahong, G. Meng, Y. He, J. De Boeck and M. Jurczak, Cellulose nanofiber paper as an ultra flexible nonvolatile memory. *Scientific Reports*, **2014**, 4, 5532.

[144] S. Ji, B. G. Hyun, K. Kim, S. Y. Lee, S.-H. Kim, J.-Y. Kim, M. H. Song and J.-U. Park, Photo-patternable and transparent films using cellulose nanofibers for stretchable origami electronics. *NPG Asia Materials*, **2016**, 8, (8), e299.

[145] M. Nogi, N. Komoda, K. Otsuka and K. Suganuma, Foldable nanopaper antennas for origami electronics. *Nanoscale*, **2013**, 5, (10), 4395-4399.

[146] T. Zhang, W. Wang, D. Zhang, X. Zhang, Y. Ma, Y. Zhou and L. Qi, Biotemplated synthesis of gold nanoparticle–bacteria cellulose nanofiber nanocomposites and their application in biosensing. *Advanced Functional Materials*, **2010**, 20, (7), 1152-1160.

[147] M. Nogi, M. Karakawa, N. Komoda, H. Yagyu and T. T. Nge, Transparent conductive nanofiber paper for foldable solar cells. *Scientific Reports*, **2015**, 5, 17254.

[148] S.-J. Chun, E.-S. Choi, E.-H. Lee, J. H. Kim, S.-Y. Lee and S.-Y. Lee, Eco-friendly cellulose nanofiber paper-derived separator membranes featuring tunable nanoporous network channels for lithium-ion batteries. *Journal of Materials Chemistry*, **2012**, 22, (32), 16618-16626.

[149] W. Luo, J. Schardt, C. Bommier, B. Wang, J. Razink, J. Simonsen and X. Ji, Carbon nanofibers derived from cellulose nanofibers as a long-life

anode material for rechargeable sodium-ion batteries. *Journal of Materials Chemistry A*, **2013**, 1, (36), 10662-10666.

[150] G. Nyström, A. Razaq, M. Strømme, L. Nyholm and A. Mihranyan, Ultrafast all-polymer paper-based batteries. *Nano Letters*, **2009**, 9, (10), 3635-3639.

[151] Z. Fang, H. Zhu, Y. Yuan, D. Ha, S. Zhu, C. Preston, Q. Chen, Y. Li, X. Han and S. Lee, Novel nanostructured paper with ultrahigh transparency and ultrahigh haze for solar cells. *Nano Letters*, **2014**, 14, (2), 765-773.

[152] M.-C. Hsieh, H. Koga, K. Suganuma and M. Nogi, Hazy transparent cellulose nanopaper. *Scientific Reports*, **2017**, 7, 41590.

[153] H. Tang, N. Butchosa and Q. Zhou, A transparent, hazy, and strong macroscopic ribbon of oriented cellulose nanofibrils bearing poly (ethylene glycol). *Advanced Materials*, **2015**, 27, (12), 2070-2076.

[154] D. Müller, C. Rambo, D. Recouvreux, L. Porto and G. Barra, Chemical in situ polymerization of polypyrrole on bacterial cellulose nanofibers. *Synthetic Metals*, **2011**, 161, (1-2), 106-111.

[155] H. Wang, E. Zhu, J. Yang, P. Zhou, D. Sun and W. Tang, Bacterial cellulose nanofiber-supported polyaniline nanocomposites with flake-shaped morphology as supercapacitor electrodes. *The Journal of Physical Chemistry C*, **2012**, 116, (24), 13013-13019.

[156] W. Hu, S. Chen, Z. Yang, L. Liu and H. Wang, Flexible electrically conductive nanocomposite membrane based on bacterial cellulose and polyaniline. *The Journal of Physical Chemistry B*, **2011**, 115, (26), 8453-8457.

[157] Y. Fujisaki, H. Koga, Y. Nakajima, M. Nakata, H. Tsuji, T. Yamamoto, T. Kurita, M. Nogi and N. Shimidzu, Transparent nanopaper-based flexible

organic thin-film transistor array. *Advanced Functional Materials*, **2014**, 24, (12), 1657-1663.

[158] Y. Okahisa, A. Yoshida, S. Miyaguchi and H. Yano, Optically transparent wood–cellulose nanocomposite as a base substrate for flexible organic light-emitting diode displays. *Composites Science and Technology*, **2009**, 69, (11-12), 1958-1961.

[159] S. Ummartyotin, J. Juntaro, M. Sain and H. Manuspiya, Development of transparent bacterial cellulose nanocomposite film as substrate for flexible organic light emitting diode (OLED) display. *Industrial Crops Products*, **2012**, 35, (1), 92-97.

[160] T. Inui, H. Koga, M. Nogi, N. Komoda and K. Suganuma, A miniaturized flexible antenna printed on a high dielectric constant nanopaper composite. *Advanced Materials*, **2015**, 27, (6), 1112-1116.

[161] N. Komoda, M. Nogi, K. Suganuma, H. Koga and K. Otsuka In *Silver nanowire antenna printed on polymer and paper substrates*, 2012 12th IEEE International Conference on Nanotechnology (IEEE-NANO), 2012; IEEE: 2012; pp 1-5.

[162] K. Abe and H. Yano, Formation of hydrogels from cellulose nanofibers. *Carbohydrate Polymers*, **2011**, 85, (4), 733-737.

[163] K. Abe and H. Yano, Cellulose nanofiber-based hydrogels with high mechanical strength. *Cellulose*, **2012**, 19, (6), 1907-1912.

[164] A. Bhatnagar and M. Sain, Processing of cellulose nanofiber-reinforced composites. *Journal of Reinforced Plastics Composites*, **2005**, 24, (12), 1259-1268.

[165] A. Iwatake, M. Nogi and H. Yano, Cellulose nanofiber-reinforced polylactic acid. *Composites Science and Technology*, **2008**, 68, (9), 2103-2106.

[166] L. Zhang, X. Li, L. Ong, R. F. Tabor, B. A. Bowen, A. I. Fernando, A. Nilghaz, G. Garnier, S. L. Gras and X. Wang, Cellulose nanofibre textured SERS substrate. *Colloids Surfaces A*, **2015**, 468, 309-314.

[167] P. Liou, F. X. Nayigiziki, F. Kong, A. Mustapha and M. Lin, Cellulose nanofibers coated with silver nanoparticles as a SERS platform for detection of pesticides in apples. *Carbohydrate Polymers*, **2017**, 157, 643-650.

[168] M. Park, H. Chang, D. H. Jeong and J. Hyun, Spatial deformation of nanocellulose hydrogel enhances SERS. *BioChip Journal*, **2013**, 7, (3), 234-241.

[169] Z. Xiong, M. Lin, H. Lin and M. Huang, Facile synthesis of cellulose nanofiber nanocomposite as a SERS substrate for detection of thiram in juice. *Carbohydrate Polymers*, **2018**, 189, 79-86.

[170] H. Wei, K. Rodriguez, S. Renneckar and P. J. Vikesland, Environmental science and engineering applications of nanocellulose-based nanocomposites. *Environmental Science: Nano*, **2014**, 1, (4), 302-316.

[171] M. Smyth, C. Fournier, C. Driemeier, C. Picart, E. J. Foster and J. Bras, Tunable structural and mechanical properties of cellulose nanofiber substrates in aqueous conditions for stem cell culture. *Biomacromolecules*, **2017**, 18, (7), 2034-2044.

[172] X. He, Q. Xiao, C. Lu, Y. Wang, X. Zhang, J. Zhao, W. Zhang, X. Zhang and Y. Deng, Uniaxially aligned electrospun all-cellulose nanocomposite

nanofibers reinforced with cellulose nanocrystals: scaffold for tissue engineering. *Biomacromolecules*, **2014**, 15, (2), 618-627.

[173] R. Pértile, S. Moreira, F. Andrade, L. Domingues and M. Gama, Bacterial cellulose modified using recombinant proteins to improve neuronal and mesenchymal cell adhesion. *Biotechnology Progress*, **2012**, 28, (2), 526-532.

[174] P. M. Favi, R. S. Benson, N. R. Neilsen, R. L. Hammonds, C. C. Bates, C. P. Stephens and M. S. Dhar, Cell proliferation, viability, and in vitro differentiation of equine mesenchymal stem cells seeded on bacterial cellulose hydrogel scaffolds. *Materials Science Engineering: C*, **2013**, 33, (4), 1935-1944.

[175] Q. Xing, F. Zhao, S. Chen, J. McNamara, M. A. DeCoster and Y. M. Lvov, Porous biocompatible three-dimensional scaffolds of cellulose microfiber/gelatin composites for cell culture. *Acta Biomaterialia*, **2010**, 6, (6), 2132-2139.

[176] E. Morales-Narváez, H. Golmohammadi, T. Naghdi, H. Yousefi, U. Kostiv, D. Horak, N. Pourreza and A. Merkoçi, Nanopaper as an optical sensing platform. *ACS Nano*, **2015**, 9, (7), 7296-7305.

[177] F. Cheng, X. Cao, H. Li, T. Liu, X. Xie, D. Huang, S. Maharjan, H. P. Bei, A. Gómez and J. Li, Generation of cost-effective paper-based tissue models through matrix-assisted sacrificial 3D printing. *Nano Letters*, **2019**, 19, (6), 3603-3611.

[178] Y. Habibi, H. Chanzy and M. R. Vignon, TEMPO-mediated surface oxidation of cellulose whiskers. *Cellulose*, **2006**, 13, (6), 679-687.

[179] T. Li, S. X. Li, W. Kong, C. Chen, E. Hitz, C. Jia, J. Dai, X. Zhang, R. Briber and Z. Siwy, A nanofluidic ion regulation membrane with aligned cellulose nanofibers. *Science advances*, **2019**, 5, (2), eaau4238.

[180] O. Nabinejad, D. Sujan, M. Rahman, W. Y. Liew and I. J. Davies, Mechanical and thermal characterization of polyester composite containing treated wood flour from Palm oil biomass. *Polymer Composites*, **2018**, 39, (4), 1200-1211.

[181] O. Nabinejad, D. Sujan, M. Rahman and I. J. Davies, Effect of filler load on the curing behavior and mechanical and thermal performance of wood flour filled thermoset composites. *Journal of cleaner production*, **2017**, 164, 1145-1156.

[182] P. Huang, Y. Zhao, S. Kuga, M. Wu and Y. Huang, A versatile method for producing functionalized cellulose nanofibers and their application. *Nanoscale*, **2016**, 8, (6), 3753-3759.

[183] L. Geng, N. Mittal, C. Zhan, F. Ansari, P. R. Sharma, X. Peng, B. S. Hsiao and L. D. Söderberg, Understanding the mechanistic behavior of highly charged cellulose nanofibers in aqueous systems. *Macromolecules*, **2018**, 51, (4), 1498-1506.

[184] L. O. Pinto, J. S. Bernardes and C. A. Rezende, Low-energy preparation of cellulose nanofibers from sugarcane bagasse by modulating the surface charge density. *Carbohydrate Polymers*, **2019**, 218, 145-153.

[185] A. J. Onyianta, M. Dorris and R. L. Williams, Aqueous morpholine pre-treatment in cellulose nanofibril (CNF) production: comparison with carboxymethylation and TEMPO oxidisation pre-treatment methods. *Cellulose*, **2018**, 25, (2), 1047-1064.

[186] O. Nechyporchuk, M. N. Belgacem and F. d. r. Pignon, Current progress in rheology of cellulose nanofibril suspensions. *Biomacromolecules*, **2016**, 17, (7), 2311-2320.

[187] E. J. Walsh, A. Feuerborn, J. H. Wheeler, A. N. Tan, W. M. Durham, K. R. Foster and P. R. Cook, Microfluidics with fluid walls. *Nature communications*, **2017**, 8, (1), 816.

[188] A. W. Martinez, S. T. Phillips and G. M. Whitesides, Three-dimensional microfluidic devices fabricated in layered paper and tape. *Proceedings of the National Academy of Sciences*, **2008**, 105, (50), 19606-19611.

[189] Y. Lin, D. Gritsenko, S. Feng, Y. C. Teh, X. Lu and J. Xu, Detection of heavy metal by paper-based microfluidics. *Biosensors and Bioelectronics*, **2016**, 83, 256-266.

[190] S. Cosson and M. Lutolf, Hydrogel microfluidics for the patterning of pluripotent stem cells. *Scientific reports*, **2014**, 4, 4462.

[191] M. Zanini, A. Lavoratti, L. K. Lazzari, D. Galiotto, M. Pagnocelli, C. Baldasso and A. J. Zattera, Producing aerogels from silanized cellulose nanofiber suspension. *Cellulose*, **2017**, 24, (2), 769-779.

[192] I. A. L. C. T. C. Group, Cisplatin-based adjuvant chemotherapy in patients with completely resected non–small-cell lung cancer. *New England Journal of Medicine*, **2004**, 350, (4), 351-360.

[193] M. P. Barr, S. G. Gray, A. C. Hoffmann, R. A. Hilger, J. Thomale, J. D. O'Flaherty, D. A. Fennell, D. Richard, J. J. O'Leary and K. J. O'Byrne, Generation and characterisation of cisplatin-resistant non-small cell lung cancer cell lines displaying a stem-like signature. *PloS one*, **2013**, 8, (1), e54193.

[194] S. Dhar, N. Kolishetti, S. J. Lippard and O. C. Farokhzad, Targeted delivery of a cisplatin prodrug for safer and more effective prostate cancer therapy in vivo. *Proceedings of the National Academy of Sciences*, **2011**, 108, (5), 1850-1855.

[195] K. D. Lee, Y.-I. Jeong, G.-T. L. Da Hye Kim and K.-C. Choi, Cisplatin-incorporated nanoparticles of poly (acrylic acid-co-methyl methacrylate) copolymer. *International journal of nanomedicine*, **2013**, 8, 2835.

초 록

본 논문에서는 셀룰로오스 나노섬유 하이드로겔을 3D 프린팅 매트릭스로 활용하기 위한 전략과 프린팅 충실도를 평가하기 위한 기준을 제시하였고, 건조 시 얇고 투명한 필름을 제조할 수 있다는 특성을 바탕으로 마이크로유체칩을 제조하였다.

셀룰로오스 나노섬유는 3 차원 인쇄에 적합한 유변학적 특성으로 인해 최근 3D 프린팅 분야에서 주목을 받아왔으며, 3D 프린팅 잉크로의 활용 가능성이 높은 재료이다. 그러나 하이드로겔 잉크는 변형에 취약하여 기존의 프린팅 기술로는 3 차원 구조물을 제조하는데 한계가 있어, 구조물을 지지해줄 수 있는 매트릭스 재료를 활용한 매트릭스 지원 3D 프린팅 기술이 제안되었다. 현재까지 셀룰로오스 나노섬유를 3D 프린팅 매트릭스로 활용하고자 하는 연구는 보고된 바가 없으며 본 연구에서는 셀룰로오스 나노섬유가 3D 프린팅 매트릭스로 활용되기 위한 최적의 조건을 탐색하였다.

셀룰로오스 나노섬유의 유변학적 특성은 섬유의 크기 및 농도에 의해 결정된다. 본 연구에서는 섬유의 크기를 카르복시메틸화를 통해 조절하였으며, 다양한 농도 조건에서의 프린팅 충실도를 평가하기 위한 기준을 제시하였다. 프린팅 충실도는 셀룰로오스 나노섬유 매트릭스와 혼화성의 차이를 보이는 친수성, 소수성 모델 잉크를 프린팅 하고 잉크의 형상을 관찰하여 평가하는 방식으로 진행하였다. 각이진 선을 프린팅 하고 각도의 날카로운 정도와 잉크의 단면 비율, 그리고 잉크 표면 거칠기를 분석하여 매트릭스의 유변학적 특성과 프린팅 충실도 간의 관계를 분석하였다. 이를 활용하여 셀룰로오스 나노섬유

매트릭스 내부에 바이오 잉크를 프린팅 할 수 있었으며 소수성 실리콘 기반 잉크로 복잡한 3차원 구조체를 제조할 수 있었다.

셀룰로오스 나노섬유는 프린팅 매트릭스로 활용될 수 있을 뿐만 아니라 간단한 건조과정을 통해 얇고 투명한 디바이스를 제조하기 최적화 되어있는 재료이다. 이러한 장점을 활용하여 셀룰로오스 나노섬유 기반의 마이크로유체칩을 제조할 수 있었다. 셀룰로오스 나노섬유의 투명도와 물질확산특성은 화학 센서뿐만 아니라 세포를 배양하고 세포의 거동을 분석할 수 있는 세포 배양 플랫폼으로도 활용될 수 있었다.

감사의 글

먼저 많이 부족한 저를 연구에 대한 열정과 사랑으로 지도해주신 현진호 교수님께 진심으로 감사의 말씀을 드립니다. 6 년의 시간 동안 많은 연구와 과제들을 수행하면서 교수님께서 주신 신뢰와 믿음을 잊지 않겠습니다. 교수님이 주신 신뢰가 있었기에 지금의 제가 있을 수 있었습니다. 교수님의 제자라는 것이 자랑스럽도록 늘 노력하며 성실하게 살아가겠습니다. 교수님, 감사합니다.

제가 이 박사 학위논문을 완성하기까지 애정과 열정으로 많은 가르침을 주셨던 전공교수님들께도 감사의 말을 전하고 싶습니다. 고분자 재료물성학을 열정적으로 교육하시고 학생들과 항상 교류하려고 노력하시는 박종신 교수님, 학생들과 스스럼없이 지내고 때론 스승처럼 때론 친구처럼 챙겨주신 이기훈 교수님, 항상 인자한 웃음으로 제게 관심 가져 주셨던 김태일 교수님, 제가 연구에 있어서 어려움에 맞닥뜨릴 때 마다 자세히 알려주시고 도와주셨던 기창석 교수님, 마지막으로 제가 찾아 뵐 때 마다 밝게 격려해주신 곽선영 교수님께 진심으로 감사드립니다. 현재는 퇴임하셨지만 제게 인생의 조언을 아낌없이 해주셨던 박영환 교수님께도 깊이 감사드립니다. 학부시절부터 교수님들의 가르침을 통해 학문적으로, 인격적으로 많이 발전할 수 있었습니다. 이렇게 학위과정을 마치고 제가 10 년간 몸담았던 바이오소재공학을 떠나지만, 저는 이제 시작이라고 생각합니다. 교수님들의 가르침을 바탕으로 멋진 연구자가 될 때까지 노력하겠습니다.

6 년간의 대학원생활을 돌이켜보면 정말 많은 일들이 있었습니다. 처음 논문을 읽고 연구를 시작할 때 생각이 납니다. 멋지고 가슴 뛰는 연구를 하겠다는 저의 다짐과는 달리 연구주제를 잡고 실험을 하는 것은 어려움의 연속이었습니다. 그럴

때 마다 저희 나노바이오소재 연구실의 선배님들은 제게 동기부여가 되었습니다. 나경아 박사님, 정걸 박사님, 박민성 박사님의 연구에 대한 열정은 제가 나아가야할 올바른 방향을 잡을 수 있게 한 크나큰 원동력이었습니다. 뿐만 아니라 저와 함께 연구하고 즐거운 시간을 보냈던 은수, 동혁이, 종현이, 호정이형, 현지, 성아, 재환이, 화련이, 동한이, 준식이 모두에게 깊은 감사의 말씀을 전합니다. 여러분들과 함께했던 추억들은 절대 잊지 못할 것 같습니다. 함께 지내면서 정말 즐거웠고 모두 건승을 빕니다.

2010 년 관악에 온 뒤로 어느새 10 년이라는 시간이 지났습니다. 20 대의 모든 시간과 열정을 보낸 이 곳이 단지 학위를 취득하는 것뿐만 아니라 제가 살아가는데 있어서의 가치와 의미를 돌이켜보고 고민할 수 있었던 중요한 공간이었다는 생각이 듭니다. 앞으로도 지난 경험을 바탕으로 더 나은 연구자가 될 수 있도록 항상 노력하겠습니다.

저의 그동안의 학위 과정과 이 논문은 모두 사랑하는 우리 가족 덕분입니다. 저를 무조건적으로 믿어주시고, 응원해주시고, 사랑해주신 우리 아버지, 어머니, 그리고 승희에게도 정말 감사드립니다. 아버지, 어머니가 없었다면 지금의 저도 없습니다. 앞으로 더 훌륭하고 자랑스런 아들, 그리고 오빠가 될 수 있도록 노력하겠습니다. 마지막으로 지난 9 년동안 제 곁에서 저를 지켜준 사랑하는 나의 아내 주현이에게 남편의 학업을 지지해주어 고맙고, 미안하고, 사랑한다는 말을 전합니다.

2020 년 1 월

신 성 철 올림